

SPECTRAL IMAGING BASED IN VIVO MODEL SYSTEM FOR CHARACTERIZATION
OF TUMOR MICROVESSEL RESPONSE TO VASCULAR TARGETING AGENTS

By

MAMTA WANKHEDE

A DISSERTATION PRESENTED TO THE GRADUATE SCHOOL
OF THE UNIVERSITY OF FLORIDA IN PARTIAL FULFILLMENT
OF THE REQUIREMENTS FOR THE DEGREE OF
DOCTOR OF PHILOSOPHY

UNIVERSITY OF FLORIDA

2010

© 2010 Mamta Wankhede

To my Mom

ACKNOWLEDGMENTS

I hereby take the opportunity to thank all who have been a part of this journey with me. My heartiest thanks go to Dr. Brian Sorg, who has been my mentor, guide, and source of inspiration for the past five years. I can only hope that his discipline and hardworking nature has rubbed off on us (his students) and made us as 'Sorganized' as himself. I am also thankful to my committee members Dr. Dietmar Siemann, Dr. Brandi Ormerod, and Dr. Paul Carney for guiding and shaping my research in the right direction. This work would not have been possible without the contribution of our collaborators – Dr. Mohan Raizada, Dr. Rodrigo Fraga-Silva, Dr. Lori Rice, Chris Pampo, Sharon Lepler, Dr. Suk-Paul Oh, and Dr. Abhinav Acharya. My special thanks to Chris Pampo for being there for me when I needed help the most.

I take this opportunity to extend my true appreciation and gratitude for the help and contribution of all my colleagues – Casey deDeugd, Se-woon Choe, Jennifer Lee and Gizmo, Raymond Kozikowsky, Phillip Barish, and all members of Kesorgle lab – toward the completion of the presented research. Three cheers to all our successes and failures.

Last but not the least, I would like to thank all my friends and family – Vaishali, Suresh, Chandrakiran, Ravikant, Kevin, Arnav, Bhajji, Mithu, Ziggy, Isabella, and Mannu – for their support and patience through these years.

TABLE OF CONTENTS

| | <u>page</u> |
|--|-------------|
| ACKNOWLEDGMENTS | 4 |
| TABLE OF CONTENTS | 5 |
| LIST OF FIGURES | 8 |
| LIST OF TABLES | 12 |
| ABSTRACT | 13 |
| CHAPTER | |
| 1 INTRODUCTION | 14 |
| Tumor versus Normal Vasculature | 14 |
| Vascular Targeting for Tumor Therapy | 15 |
| Vascular Disrupting Agents and Anti-angiogenic Agents | 16 |
| OXi4503 and Other Vascular Disrupting Agents | 16 |
| Anti-VEGF Angiogenesis Inhibitor Avastin | 19 |
| Need for Combinatorial Approach..... | 20 |
| Evaluation Tools for Vascular Targeting Therapy | 22 |
| Motivation and Goal of Research..... | 23 |
| 2 MOUSE MODEL AND SPECTRAL IMAGING SYSTEM: AN INTRODUCTION | 25 |
| Window Chamber Mouse Model: Background..... | 25 |
| Spectral Imaging: Background..... | 27 |
| Imaging Acquisition and Image Processing: Techniques Used in the Presented Research | 29 |
| Imaging System..... | 29 |
| Image Acquisition | 30 |
| Image Processing..... | 31 |
| 3 SPECTRAL IMAGING OF WINDOW CHAMBERS: A VERSATILE TOOL FOR VASCULAR PATHOLOGY STUDIES..... | 34 |
| Introduction | 34 |
| Materials and Methods..... | 36 |
| Methods for Tumor Vessel Acute Oxygenation Fluctuations | 36 |
| Preparation of fluorescent red blood cells | 36 |
| Preparation of 4TO7 tumor cells | 37 |
| Window surgery, in vivo tumor initiation and tumor imaging | 38 |
| Image and data processing..... | 38 |

| | | |
|---|--|----|
| | Red blood cell flux imaging | 39 |
| | Methods for Induced Thrombus Experiments | 40 |
| | Experiment design summary | 40 |
| | Surgery | 41 |
| | Platelet labeling and visualization | 41 |
| | Thrombus induction | 42 |
| | Thrombus imaging | 42 |
| | Methods for Arterio-venous Malformation Experiments | 42 |
| | Experiment design summary | 42 |
| | Window chamber wound model | 43 |
| | Spectral imaging | 43 |
| | Blood flow imaging | 43 |
| | Results | 44 |
| | Tumor Microvascular Acute Oxygenation Fluctuations | 44 |
| | Spectral Imaging for Study of Microvascular Occlusions | 50 |
| | Spectral Imaging for Real-Time Imaging of Arterio-Venous Malformations | 53 |
| | Discussion | 58 |
| 4 | OXi4503 TREATMENT OF 4T1 and CAKI-1 TUMORS | 61 |
| | Introduction | 61 |
| | Materials and Methods | 63 |
| | Tumor Cells | 63 |
| | Animal Model | 63 |
| | Drug Preparation and Experimental Design | 64 |
| | Imaging System, Image Acquisition and Image Processing | 64 |
| | Results | 65 |
| | Treatment of 4T1 Mouse Mammary Carcinomas | 65 |
| | Treatment of Caki-1 Human Renal Carcinomas | 68 |
| | Rapid Oxygenation Changes after OXi4503 Treatment | 70 |
| | Discussion | 77 |
| 5 | OXI4503 AND AVASTIN COMBINATION TREATMENT OF CAKI-1 TUMORS | 81 |
| | Introduction | 81 |
| | Materials and Methods | 84 |
| | Tumor Cells | 84 |
| | Animal Model | 84 |
| | Drug Preparation and Experimental Design | 85 |
| | Vascular disrupting agent OXi4503 | 85 |
| | Angiogenesis inhibitor Avastin | 85 |
| | Individual and combinatorial treatment design and imaging schedule | 85 |
| | Tumor Size Measurement | 86 |
| | Imaging System, Image Acquisition and Image Processing | 86 |
| | Statistical Analysis | 87 |
| | Results | 87 |
| | Tumor Model Identification | 87 |

| | |
|---|-----|
| Caki-1 tumor growth after individual treatment with OXi4503 | 87 |
| Effect of OXi4503 treatment on Caki-1 tumors: Hemoglobin saturation (HbSat) assessment | 89 |
| Combination Treatment with OXi4503 and Avastin | 91 |
| Tumor growth study | 91 |
| Quantitative HbSat analysis and comparison..... | 93 |
| Discussion | 98 |
| 6 CONCLUSION AND FUTURE DIRECTION | 103 |
| LIST OF REFERENCES | 105 |
| BIOGRAPHICAL SKETCH..... | 122 |

LIST OF FIGURES

| <u>Figure</u> | <u>page</u> |
|---------------|---|
| 2-1 | The window chamber model. Figure 2-1a shows the window chamber implanted on a healthy nude mouse. Figure 2-1b demonstrates the 4T1 tumor growing at the implantation site in the window chamber indicated by the dashed circle, several days after implantation. 26 |
| 2-2 | Description of a spectral image data set [86]. As described by Garini et al. each point in the 3-D spectral image cube represents a single number and the spectral image is described as $I(x,y,k)$. It can be viewed either as an image $I(x,y)$ at each wavelength k , or as a spectrum $I(k)$ at every pixel (x,y) 28 |
| 2-3 | The Imaging system. The Zeiss-based imaging microscope system is shown in Figure 2-2a. Figure 2-2b gives a close view of the mouse being imaged, placed on the heating pad and breathing through the nose cone. 30 |
| 2-4 | Flow diagram depicting the image processing method to obtain hemoglobin saturation map from the stack of 16 images obtained via spectral imaging. 33 |
| 3-1 | Transmitted light image of the tumor microvessel network. It is a 4T07 mouse mammary carcinoma with a diameter of 1.5 to 2.0 mm 9 days after implantation of cells. White triangles represent regions of interest chosen for analysis. A 10x objective was used for imaging (NA of 0.3, working distance of 5.5 mm). 46 |
| 3-2 | Hemoglobin saturation image of the tumor microvessel network in Figure 3-1. The pixels are colored according to the hemoglobin saturation scale to the right of the figure. The background is black. Regions of interest for analysis are indicated in the figure. 47 |
| 3-3 | Fluorescence image of RBCs labeled with DiD flowing in the tumor microvessel network. Images were captured with an electron multiplying CCD camera at video rates (30 Hz). 20 s of data were taken every minute of the hour-long imaging session, and cells were counted over this time increment and then converted to RBC flux measurements. The locations of the regions of interest for analysis are indicated in the figure. 48 |
| 3-4 | Plot of RBC flux versus hemoglobin saturation (HbSat) for region of interest 1 in Figure 3-1. The data points were acquired at 1 min intervals for 1 h. 49 |
| 3-5 | Plot of RBC flux versus hemoglobin saturation (HbSat) for region of interest 3 in Figure 3-1. The data points were acquired at 1 min intervals for 1 h. 49 |
| 3-6 | Brightfield and HbSat images are shown before and 21 minutes after topical application of FeCl ₃ to induce thrombus formation. The red dotted line in the top left image indicates where the border of the paper soaked with FeCl ₃ |

| | | |
|------|--|----|
| | was relative to the image area. The yellow box indicates the region shown in the images in Figure 3-7 at higher magnification..... | 51 |
| 3-7 | Brightfield and HbSat time sequence images of thrombus development for the region indicated by the yellow box in Figure 3-6. The yellow outlined area on the venule in the top left image indicates the ROI used for the HbSat measurements shown in Figure 3-8. The arrow in the brightfield image at the 8-min time point indicates a forming thrombus. | 52 |
| 3-8 | Plot of the HbSat in the ROI indicated in Figure 4-2 at various time points during thrombus development. The data points in the figure are given as the median±interquartile range for the ROI. | 53 |
| 3-9 | AVM development in a conditional Alk1 deletion mouse (ROSA26 ^{CreER} /Alk1 ^{2f/-}) stimulated by a wound, where A, arteriole; V, venule; and W, wound. The left column shows transmitted light images and the right column shows HbSat images. Region where AVMs formed is indicated in the day 5 and day 9 images. At day 5, the AVM connections were not obvious but clear changes in venule oxygenation could be seen due to the AVMs. The arrowheads indicating the arteriole and venule also indicate regions of interest where HbSat measurements were obtained. | 56 |
| 3-10 | Wound healing in a control mouse: A, arteriole; V, venule; and W, wound. The left column shows transmitted light brightfield images and the right column shows HbSat images. The arrowheads indicating the arteriole and venule also indicate regions of interest where HbSat measurements were obtained. Unlike the conditional Alk1 deletion mouse in Figure 3-9, no AVMs formed during wound healing. | 57 |
| 4-1 | Typical OXi4503 treatment progression in a 4T1 tumor-bearing mouse. The brightfield images (left hand figures in each panel) show structural alterations in the vasculature through the course of the single treatment. The approximate tumor border is indicated by the dotted line in (A). Vessels outside the dotted line are considered normal tissue vasculature. The tumor periphery consisted of a 250- to 500-µm thin border on the circumference of the tumor. Remaining tumor vasculature except for the periphery constituted the tumor core. Images were obtained at x2.5 magnification with image dimensions of 4.15x3.125 mm. The HbSat maps are shown in the right hand figures in each panel. The oxygenation levels in the HbSat maps are color coded as indicated by the colorbar. Arrows in frames (G) and (H) highlight the disintegrating vasculature, while arrows in (I) and (J) indicate an example vessel that persists through all time-points with only oxygenation changes. The star in frames (M) and (O) indicate the avascular regions created by the OXi4503 treatment. | 71 |
| 4-2 | Recovery, re-oxygenation, vascular remodeling, and neovascularization in the 4T1 tumor during the recovery phase after OXi4503 treatment for the | |

area indicated in Figure 1O by the dotted rectangle. The approximate tumor border is demarcated by the dotted line in the first bright field image. The arrows highlight an example vessel that maintains its structure throughout the treatment but undergoes dramatic oxygenation changes. The color-scale for hemoglobin saturation is the same as in Figure 4-1. 72

4-3 Quantitative tumor regional analysis for 4T1 tumor treatment. The tumor was divided into core, periphery, and normal tissue for purposes of analysis. (A) Brightfield images before and after every successive treatment of the tumor in Figure 4-1. (B) Cumulative HbSat values (mean \pm standard error) for 3 serial treatments in all 5 4T1 tumor mice. Arrows indicate drug administration. (C) Cumulative HbSat values (mean \pm standard error) for 3 serial sham treatments (saline) in all 3 control mice. 73

4-4 OXi4503 treatment 2 of a Caki-1 tumor bearing mouse. Images were obtained at x2.5 magnification with image dimensions of 4.15x3.125 mm. The HbSat maps are shown in the right hand figures in each panel. The oxygenation levels in the HbSat maps are color coded as indicated by the colorbar. 74

4-5 Quantitative tumor regional analysis for Caki-1 tumor treatment. The tumor was divided into core, periphery, and normal tissue for purposes of analysis. (A) Brightfield images before and after every successive treatment of the tumor in Figure 6-4. (B) Cumulative HbSat values (mean \pm standard error) for 3 serial treatments in all 5 4T1 tumor mice. Arrows indicate drug administration. (C) Cumulative HbSat values (mean \pm standard error) for 3 serial sham treatments (saline) in a control mouse. 75

4-6 Rapid oxygenation changes in 4T1 tumor microvasculature after treatment with VDA OXi4503. The mouse was imaged for 20 min before treatment and for 60 min after treatment. Spectral images were obtained every 30 sec. (A) Brightfield image of the tumor microvasculature. (B) Hemoglobin saturation before and after OXi4503 treatment. 76

5-1 Effect of OXi4503 treatment on different sized Caki-1 tumors. As shown in Figure 5-1A (i) and (ii), tumors with pre-OXi4503 volumes up to 50 mm³ demonstrated control of tumor growth compared to controls in the window chamber model. 88

5-2 Example of one of the serial OXi4503 treatments in one mouse. The brightfield images are shown along with the corresponding hemoglobin saturation maps. At the beginning of treatment the tumor was approximately 55 mm³ in volume and 12 days old. Structural deterioration of tumor vessel network is evident in the brightfield images up to 8 h post Tx, with recovery of peripheral vessels from 24 h. Oxygenation plummeted corresponding to the structural damage nearly to 8 h and recovered on the tumor rim from 8 h. At 48 h post Tx tumor had shrunk to nearly 42 mm³ in volume. 90

- 5-3 Tumor volume comparison after individual and combination treatment with OXi4503 and Avastin. It was observed that combination of therapeutics have additive/supra-additive effects on tumor size reduction of Caki1 tumors. A) The carrier treatment had no effect on tumor growth retardation. B) Avastin alone did not reduce the tumor size appreciably. C) The treatment of OXi4503 alone retarded the tumor growth D) Trend suggests that the combinatorial treatment of Avastin and OXi4503 reduces the tumor size with each consecutive treatment. E) Interesting significantly different pairs ($p < 0.05$) are as follows: treatments marked with * as compared to 48h post Tx2 and Tx3 of Avastin..... 92
- 5-4 Example of classification of tumor core, periphery and normal vasculature. The periphery was chosen between 250-500 μm on the tumor rim..... 94
- 5-5 The HbSat or oxygenation of the periphery, core and normal microvessels modulates with individual treatments with (A) Oxi4503 or (B) Avastin, or their (C) combination at different time points and (D) control. Two-way ANOVA was performed on HbSat values normalized to 0 h time points of each treatment obtained from more than 3 mice per group and the average values of HbSat and standard error are plotted against corresponding time points. Significant differences between individual time points are indicated. The black arrows represent the time point where treatment was given to mice..... 97

LIST OF TABLES

| <u>Table</u> | | <u>page</u> |
|--------------|--|-------------|
| 1-1 | Small-molecule VDAs in active clinical development. Adopted from[1] | 17 |
| 3-1 | Comparison of arteriole and venule saturation in a mouse model of HHT during wound healing. | 58 |

Abstract of Dissertation Presented to the Graduate School
of the University of Florida in Partial Fulfillment of the
Requirements for the Degree of Doctor of Philosophy

SPECTRAL IMAGING BASED MODEL IN VIVO SYSTEM FOR CHARACTERIZATION
OF TUMOR MICROVESSEL RESPONSE TO VASCULAR TARGETING AGENTS

By

Mamta Wankhede

December 2010

Chair: Brian Sorg

Major: Biomedical Engineering

Functional vasculature is vital for tumor growth, proliferation, and metastasis. Many tumor-specific vascular targeting agents (VTAs) aim to destroy this essential tumor vasculature to induce indirect tumor cell death via oxygen and nutrition deprivation. The tumor angiogenesis-inhibiting anti-angiogenics (AIs) and the established tumor vessel targeting vascular disrupting agents (VDAs) are the two major players in the vascular targeting field. Combination of VTAs with conventional therapies or with each other, have been shown to have additive or supra-additive effects on tumor control and treatment. Pathophysiological changes post-VTA treatment in terms of structural and vessel function changes are important parameters to characterize the treatment efficacy. Despite the abundance of information regarding these parameters acquired using various techniques, there remains a need for a quantitative, real-time, and direct observation of these phenomenon in live animals. Through this research we aspired to develop a spectral imaging based mouse tumor system for real-time in vivo microvessel structure and functional measurements for VTA characterization. A model tumor system for window chamber studies was identified, and then combinatorial effects of VDA and AI were characterized in model tumor system.

CHAPTER 1 INTRODUCTION

Tumor versus Normal Vasculature

Under normal physiological conditions, 'angiogenesis' or sprouting of new vessels is a tightly controlled mechanism with the pro-angiogenic factors delicately balancing the anti-angiogenic factors[1]. Such physiological angiogenesis is required during fetal growth, wound healing process as well as in female reproductive system. The resulting vasculature is uniformly structured and well oxygenated.

As opposed to normal angiogenesis, pathological conditions such as tumors cause an imbalance between pro- and anti-angiogenic factors in favor of the pro-angiogenic side, resulting in accelerated vessel growth. Such enhanced vascular development is initiated by tumors to fulfill the excessive oxygen and nutrients requirements of their rapidly growing tumor mass. The resulting tumor vasculature greatly differs from normal vasculature in both structural and molecular aspects.

In most big tumors the core remains comparatively non-vascularized. Vasculature in the remaining tumor areas is often found to be leaky, unorganized, and deformed resulting in a vasculature system which is maximally stimulated yet minimally fulfilling the metabolic needs of the host tumor mass[2]. Other vascular abnormalities include temporary occlusions, rapidly dividing endothelial cells, blind ends, and a reduction in pericytes[3]. This results in heterogeneously distributed hostile micro-milieus within the tumor mass characterized by parameters such as hypoxia, hypoglycemia, extra-cellular acidosis etc. These hostile parameters may directly or indirectly be responsible for inducing angiogenesis, selection of aggressive cells, tumor progression and acquired treatment resistance.

It has been observed that in order to initiate aggressive vessel development, tumors rely on numerous triggering mechanisms such hypoxia, hypoglycemia, oncogenic transformations, or autocrine growth factor loops[4]. For example hypoxia, or oxygen deprivation, accelerates angiogenesis in tumors via increase in the hypoxia-inducible transcription factor-1 α (HIF-1 α), which in turn up-regulates the vascular endothelial growth factor (VEGF). VEGF is considered among one of the most important regulators of angiogenesis. On the other hand, hypoglycemia, or nutrient deprivation, induces VEGF expression through a pathway completely independent of HIF. Growing tumor mass is commonly inflicted with hypoxic and hypoglycemic insults due to mismatch in demand and supply rate. Such pathological angiogenesis can thus be called as inherent characteristics of the solid tumors.

Vascular Targeting for Tumor Therapy

Despite its abnormal structure and function, active tumor vasculature remains crucial for tumor growth, proliferation and metastasis [5]. Tumor vasculature plays essential role in tumor survival, tumor metastasis and progression, and in controlling the tumor microenvironment, thereby influencing conventional therapies[6]. Targeting tumor vasculature could thus have devastating effects on the tumor. When compromised, impaired tumor vasculature may result in indirect tumor cell death via nutrient deprivation and impaired waste product drainage. Vascular targeting thus makes a promising therapeutic target for tumor treatment and strategies targeting tumor blood vessels have been actively developed over the years[7-11].

The idea of exploiting the tumor vasculature as a form of treatment has been around since mid-1800s, with numerous strategies including bacterial inductions, use of lead colloids and arsenicals, and colchicines implemented through 1900s. A radical

approach took roots during 1980's when Juliana Denekamp proposed to use the specificity of tumor endothelial cells as a targeting approach. She suggested that the much higher proliferation rate of tumor endothelial cells compared to normal tissue could be specifically targeted to destroy the tumor vasculature. Recently this approach has gained momentum and a number of different agents are being developed selectively and specifically targeting the tumor vasculature without damaging the normal vasculature[5, 12-16]. Collectively these agents are known as 'Vascular Targeting Agents' (VTAs).

Vascular Disrupting Agents and Anti-angiogenic Agents

The vascular disrupting agents (VDAs) and angiogenic inhibitors (AIs) are two major types of vascular targeting agents currently being investigated for tumor therapy with distinct mechanisms of action, disparate treatment regimens and unique treatment application and outcomes [17]. While vascular disrupting agents (VDAs) utilize the inherent differences between normal and tumor vasculature to destroy the well-established tumor vessels [5, 12-16], the angiogenesis inhibitors' (AIs) primary function is to inhibit new vessel formation by interfering with the key signaling pathways essential for neo-angiogenesis [9, 10, 18-21]. It has been hypothesized that these two distinct and non-overlapping therapeutic approaches can be used in a synergistic manner to achieve additive therapeutic benefit, either in combination with regular chemotherapy or radiation, or in combination with each other [6, 22-26].

OXi4503 and Other Vascular Disrupting Agents

Vascular disrupting agents essentially refer to all the agents which aim at destroying the well-established tumor microvasculature without damaging the normal vessels. These agents range from physical treatments such as hyperthermia or

photodynamic therapy (PTD), to induction of cytokines such as tumor necrotic factor (TNF) and interleukins, chemotherapeutics such as Vinca alkaloids and arsenic trioxide (ATO), antibodies, peptides, and growth factors that selectively bind to tumor vessels and ultimately destroy them[6].

Small-molecule vascular targeting agents are rapidly becoming the most popular VDAs[6]. As evident from Table 1-1, majority of VDAs in clinical trials use inhibition of tubulin assembly as their mechanism of action[1].

Table 1-1. Small-molecule VDAs in active clinical development. Adopted from[1]

| Compound | Mechanism | Current development status | Tumor blood flow reductions in patients | Company |
|--------------------|------------------------------|--|---|-------------------------------|
| CA4P (Zybrestat) | Tubulin depolymerizing agent | Phase II and III clinical trials ongoing | Yes | OXiGENE, Inc. |
| DMXAA (ASA404) | TNF induction | Phase II clinical trials completed | Yes | Antisoma/Novartis |
| MN-029 (Denebulin) | Tubulin depolymerizing agent | Phase I clinical trials completed | Yes | Medicynova |
| AVE8062 (AC7700) | Tubulin depolymerizing agent | Phase I clinical trials ongoing | Yes | Sanofi-Aventis |
| ZD6126 | Tubulin depolymerizing agent | Phase I clinical trials completed | Yes | Angiogene Pharmaceuticals Ltd |
| OXi4503 | Tubulin depolymerizing agent | Phase I clinical trials ongoing | Studies ongoing | OXiGENE, Inc |
| NPI2358 | Tubulin depolymerizing agent | Phase I clinical trials ongoing | Studies ongoing | Nereus Pharmaceuticals |
| CYT997 | Tubulin depolymerizing agent | Phase I clinical trials ongoing | Studies ongoing | Cytopia |
| MPC-6827 | Tubulin depolymerizing agent | Phase I clinical trials ongoing | Studies ongoing | Myriad Pharmaceuticals |

There are two major sub-categories of small molecule VDAs. The first sub-category utilizes the cytokine induction capacity of agents like flavone acetic acid (FAA)

and its derivative 5, 6-dimethylxanthenone-4-acetic acid (DMXAA). The second sub-category utilizes the tubulin-binding capability of agents such as Combretastatin A4 Phosphate (CA4P), the phosphate prodrug of N-acetyl-colchicinol (ZD6126), Ave8062, NPI2358, MN-029, and OXi4503.

OXi4503 is the diphosphate prodrug of Combretastatin A1 (CA1), which along with its predecessor Combretastatin A4 Phosphate (CA4P) is isolated from the South African tree *Combretum Caffrum* and is considered to be among the most potent tubulin binding agents[27]. When used as a single agent against the murine breast adenocarcinoma CaNT , the murine colon tumor MAC29, the human adenocarcinoma MDA-MB-231 and the murine myocardial endothelioma MHEC5-T, OXi4503 exhibits a stronger antivasular and antitumor effect than CA4P[27]. Oxi4503 has been shown to retard tumor growth in a dose-dependent manner and improved survival in murine model of colorectal liver metastases[28]. CA4P, the analogue of OXi4503, has been shown to enhance the effects of radiation, hyperthermia, chemotherapy, and radio-immunotherapy[3].

Studies have shown that this second generation vascular disrupting agent OXi4503 not only possesses significant antivasular effects in solid tumors but also follows a similar treatment-response -trend after subsequent repeat treatments[3].

OXi4503 preferentially binds to the α -tubulin subunits inside the dividing endothelial cells, thereby preventing the formation of microtubules. The cytoskeleton of the proliferating endothelial cells gets disrupted which in turn results in endothelial cell shape changes. The endothelial cells round up, detach from the vascular wall, and finally the vascular wall collapses. This vascular collapse and the subsequent thrombus

formation blocks the vessel blood supply resulting in tumor cell death and extensive necrosis due to lack of oxygen, nutrition, and metabolic waste removal[3, 29].

While experimental evidence has confirmed the selective tumor vessel targeting and immediate microvascular destruction capacity of OXi4503, the 'viable rim' problem is still not overcome even after using the maximum tolerable doses (MTD) of the drug[28]. Since the peripheral tumor cells obtain nutrition mainly from the surrounding normal vessels, these few peripheral tumor cells survive resulting in incomplete tumor destruction. Consequently, a combination therapy of OXi4503 with traditional anticancer therapies is suggested for complete tumor eradication [3].

Anti-VEGF Angiogenesis Inhibitor Avastin

The idea that tumor angiogenesis was mediated by diffusible factors expressed by tumor cells [30], and that anti-angiogenic strategies might be effective against tumors [31] have been around since the 1960's and 70's. Since then a number of tumor angiogenesis-inducing, and possible anti-angiogenic factors, such as epidermal growth factor (EGF), transforming growth factor (TNF)- α , TGF- β , tumor-necrosis factor- α and angiotensin have been reported [32].

The vascular endothelial growth factor (VEGF, also known as VEGF-A) is a key regulator of angiogenesis, and the role of the VEGF gene family in the regulation of angiogenesis has been keenly studied [33]. While the complex process of assembly and maturation of the vessel wall is co-ordinated by several factors such as angiopoietins, platelet-derived growth factor B (PDGF-B) etc [34], VEGF-A is responsible for a rate-limiting step in normal and pathological blood vessel growth [35].

Studies have reported VEGF expression in many human tumors including lung [36], breast [37], gastrointestinal tract [38], renal [39] and ovarian carcinomas [40].

Renal cell carcinomas have been reported to have particularly high VEGF expressions. A mouse anti-human VEGF monoclonal antibody, known as A.4.6.1, has been known to possess tumor growth inhibition potential several mouse tumor models [41-44].

Avastin or Bevacizumab is the humanized form of the mouse anti-VEGF monoclonal antibody A.4.6.1. Similar to the mouse antibody, Avastin binds and neutralizes all human VEGF-A isoforms, but does not neutralize other members of the VEGF gene family [35, 45]. The pharmacokinetic properties of Avastin have been studied and its terminal half-life has been reported as 17-21 days [46]. After extensive preclinical [45, 47, 48] and clinical studies [49-53], Avastin has been approved by FDA for clinical use as a first-line therapy for metastatic colorectal cancer.

Need for Combinatorial Approach

Despite their efficacy in terms of vascular damage and tumor cell kill, the VDAs suffer from a classical Achilles' heel, often referred to as the "viable rim". The tumor periphery being mainly supplied by the normal host vasculature undestroyed by the VDA, helps sustain nearby tumor cells. Thus VDAs alone tend to be non-curative as a single therapeutic agent [3, 15]. Hence, combination of VDAs with other therapies is a logical step in order to achieve complete tumor therapy. The rationale behind combination of a VDA such as CA4P with radiation is well explained by Landuyt et al [25] as follows. They hypothesized an additive antitumor effect with the combination of the direct tumor cell kill achieved by irradiation and the majorly indirect tumor necrosis due to CA4P. Their logic being that the ionizing radiation would be more effective, especially in case of large tumors, in the proliferating and host vessel-supplied tumor periphery region, whereas CA4P would achieve indirect tumor cell death, including that of the hypoxic radio-resistant cells. Corroborating similar additive co-operation, Li et al

have reported that CA4P was able to significantly improve tumor therapy when administered 0.5-1 hour post- radiation or chemotherapy [54].

Angiogenesis inhibiting agents are unlikely be used as a single agent tumor therapeutics either. Tumor progression during the course of treatment is a major reason for therapy failure. Tumor growth and metastasis being dependent on angiogenesis, the merit of AIs mostly lies in disease control as opposed to tumor cell kill [23, 55]. Evidence suggests that cytotoxic therapies including radiation therapy can initiate tumor angiogenesis [56]. Hence the need for combination of AIs with conventional treatment is justified.

Several studies so far have demonstrated that scheduling of the VTAs with traditional chemo- and radio- therapy produce better outcomes than using VTAs alone [25, 57-59]. Furthermore, the combination of AIs with VDAs is believed to have potential for even more comprehensive tumor therapy [24-26]. Since the AIs, VDAs and conventional treatments such as chemo- and radio-therapy accomplish tumor damage via altogether different mechanisms and can have non-interfering treatment schedules; it makes sense to utilize these means to treat the tumors by attacking from as many fronts as possible.

Even though, at first thought, it would seem that VDAs and AIs might result in hindered tumor blood perfusion and reduced oxygen concentration by disrupting tumor vasculature or reducing tumor vessel density, several studies have shown conflicting data regarding tumor perfusion and oxygenation as well summarized in the review by Horsman et al. [6]. The effects of VDAs on tumor pathophysiology are relatively less controversial with typical reduction of tumor perfusion between 1-6 hours post-VDA and

recovery at later time points, with the degree and duration of the vascular shut down being dependent on the drug type, dosage, and tumor type [6]. On the contrary, AIs have been reported to induce extremely contradicting results in terms of vessel density, tumor oxygenation, and blood perfusion in different tumors evaluated using different methods [6]. Therefore we concluded that further investigation and in-depth characterization of VTA response was needed for their better utilization in tumor therapy.

Evaluation Tools for Vascular Targeting Therapy

Tumor oxygenation measurement is considered as a classical evaluation endpoint from techniques such as the Eppendorf polarographic oxygen electrodes [60-62], hypoxic markers [63-65], or radiation response assays [66-68] for characterization of AI efficacy, often times with conflicting results. On the other hand, characterization of VDA efficacy is performed in preclinical and clinical studies, by using conventional assays for tumor perfusion, blood flow, vascular structure, vessel permeability, and vascular damage in tumor and normal tissue [28, 29, 69-71]. Though useful, some of these methods are unable to provide real-time serial information in vivo, and require animal sacrifice at the point of measurement. For observing real-time in vivo changes after VDA treatments, Sheng et al used microsphere fluorescence and assessed tumor blood flow in murine flank tumors after OXi4503 treatment [27]. Several other techniques such as MRI and PET can also be used to observe blood flow changes, tumor perfusion, and vascular permeability [3, 72], but are unable to provide microvascular resolution. To obtain microvessel function data and to observe serial morphological changes after VDA treatment, Tozer et al have employed multi-photon fluorescence microscopy measurements in their window chamber models [73].

We thought it important to look at microvessel oxygenation for VTA characterization, not only because they induce oxygenation fluctuations, but also due to the relevance of tumor oxygen status for other therapeutic modalities. As we know, oxygenation of a vessel depends on several factors such as hemoglobin saturation (HbSat), perfusion, and red cell flux [74, 75]. Spectral imaging enabled us to provide direct information regarding microvessel oxygenation in terms of HbSat.

Motivation and Goal of Research

Development of novel VTAs holds promise for effective tumor treatment. Combination of VTAs with conventional therapies or with each other, have been shown to have additive or supra-additive effects on tumor control and therapy. Thorough preclinical evaluation of these drugs in live animal models is essential prior to human trials. Pathophysiological changes post-VTA treatment in terms of structural and vessel function changes are important parameters to characterize the treatment efficacy and optimize treatment regimen. Despite the abundance of information regarding these parameters acquired using various techniques, there remains a need for a quantitative, real-time, and direct observation of these phenomenon in live animals. Through this research we aspired to develop a spectral imaging based mouse tumor system for real-time in vivo microvessel structure and functional measurements for VTA characterization. A model tumor system for window chamber studies was identified, and then combinatorial effects of VDA and AI were characterized in model tumor system.

Specifically, we studied the effect of individual as well as combinatorial treatment of human renal carcinomas (Caki-1 tumors) with two different VTAs (OXi4503, a tubular binding vascular disrupting agent; and Avastin, an anti-VEGF angiogenesis inhibitor) using our mouse window chamber model and spectral imaging system. We were able to

provide further insights in the working of these drugs and study their effects on tumor vessel pathophysiology. The eventual goal of this research is the in-depth characterization and optimal combinatorial scheduling of VTAs with conventional therapies.

CHAPTER 2 MOUSE MODEL AND SPECTRAL IMAGING SYSTEM: AN INTRODUCTION

Window Chamber Mouse Model: Background

The rodent dorsal skinfold window chambers have been used for a long time to non-invasively study blood vessels. The chamber model has been used for microcirculatory studies [76, 77], study of endometriosis [78], and studies of tumor microvasculature and angiogenesis [79-81]. Early tumor growth and angiogenesis has been recorded by Li et al [82] by injecting 20 to 30 fluorescently labeled tumor cells into the window chamber and monitoring the tumor growth right from the initiation stages, along with tumor cell migration toward and around the existing host microvessels.

Modified window chambers have been successfully used in rats, hamsters, as well as mice [76, 77]. Imaging techniques such as confocal and multiphoton microscopy have been used with the window chamber to image fluorescently labeled cells as well as unlabeled extracellular matrix components [83-85].

We used the window chamber model in our work to look at tumors, tumor and normal microvasculature, blood hemoglobin saturation, and blood flow. Several intra-vital imaging modalities such as brightfield imaging, fluorescent imaging, Laser scanning microscopy, and spectral imaging were successfully employed in live tumor-bearing mice.

Our window chamber mouse model with the window chamber implanted on a nude mouse is depicted in Figure 2-1.

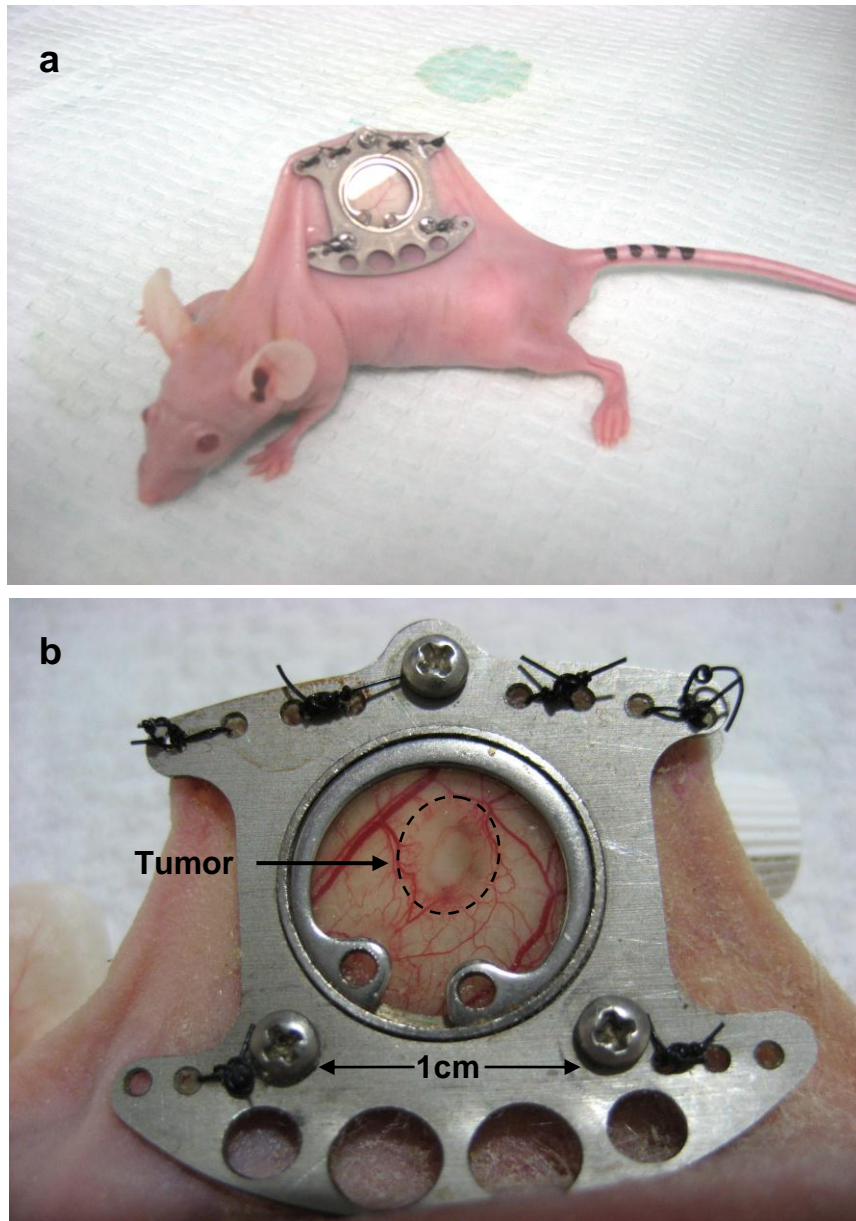


Figure 2-1. The window chamber model. Figure 2-1a shows the window chamber implanted on a healthy nude mouse. Figure 2-1b demonstrates the 4T1 tumor growing at the implantation site in the window chamber indicated by the dashed circle, several days after implantation.

Spectral Imaging: Background

Spectral imaging is a very advantageous combination of spectroscopy methods with imaging modalities. It is a great tool that allows us to simultaneously study multiple features such as organelles and proteins both qualitatively as well as quantitatively. Even though both spectroscopy and imaging techniques are well established in their respective fields, their combination is a relatively novel concept with great possibilities yet to be explored. The need to measure the spectrum each point of the image often leads to long acquisition times. For practical use in biomedical applications, compromises are made to reduce the acquisition times in a tolerable range [86].

Spectral imaging requires imaging the same object multiple times, with each image being taken at a different wavelength, thus creating a three-dimensional data set. As depicted in Figure 2-2, the spectral data acquired at each pixel is the light intensity at each wavelength, $I(x,y,\lambda)$. It can be viewed either as an image $I(x,y)$ at each wavelength k , or as a spectrum $I(k)$ at every pixel (x,y) .

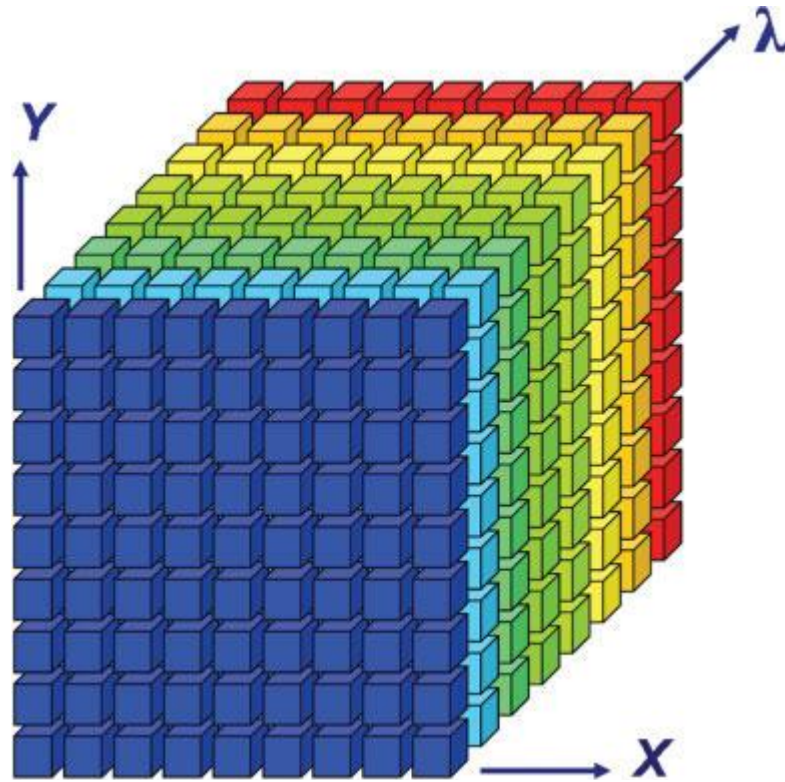


Figure 2-2. Description of a spectral image data set [86]. As described by Garini et al. each point in the 3-D spectral image cube represents a single number and the spectral image is described as $I(x,y,k)$. It can be viewed either as an image $I(x,y)$ at each wavelength k , or as a spectrum $I(k)$ at every pixel (x,y) .

The image acquisition time highly depends on the detection device, which could be a single point detector, a line detector, or a 2-D array detector such as a charged couple device (CCD). Obviously, if any of these methods are used for image detection, the spectral image acquisition could not be performed at once. There are several different strategies employed for spectral image acquisition such as, 'spatial-scan methods', 'time-scan methods', 'whole spectrum scan methods', and 'wavelength scan methods'.

For obtaining spatial scans, the entire spectrum of a portion of the image at a time is measured and the entire image is scanned in such manner. Time-scan methods measure a set of images where individual images are a superposition of spectral or spatial image information. The actual spectral information is then transformed in the actual spectral image using methods such as Fourier transforms. Moreover, the whole spectrum measurement methods involve the measurement of entire spectral image at once, but in order to do so the spectral or spatial resolution is compromised.

In wavelength scan methods, one image at one wavelength is captured at a time. For a small number of wavelengths color-filters can be used. Otherwise, any of the variable filters such as the circular-variable filter (CVF) [87], liquid –crystal tunable filter (LCTF) [88], and acousto-optical tunable filter (AOTF) [89] may be used. These filters can capture a full spectral image by measuring one image at a time but each time at a different wavelength. They enable us to acquire a user-selectable number of wavelength images with adjustable exposure time for each separate wavelength.

Imaging Acquisition and Image Processing: Techniques Used in the Presented Research

Imaging System

A Zeiss microscope (Carl Zeiss, Inc., Thornwood, NY) was used as the imaging platform (Figure 2-3). For transillumination of window chambers, a 100W tungsten halogen lamp was used. Images were obtained at 1380 x 1035 pixels and 12 bit dynamic range using a CCD camera thermoelectrically cooled to -20°C (DVC Company, Austin Texas; Model # 1412AM-T2-FW). The long working distance objectives used were 2.5x and 5x fluars, 10x EC Plan-NeoFluar, and a 20x LD-Plan-NeoFluar (Carl Zeiss, Inc., Thornwood, NY). Hyperspectral images were obtained via band-limited

optical filtering using a C-mounted liquid crystal tunable filter (LCTF) (CRI, Inc., Woburn, MA) with a 400-720nm transmission range and a 10 nm nominal bandwidth, placed in front of the camera. Images were saved as 16-bit TIF files. Fluorescent images for 4T1-GFP were taken using a FITC filter set (Carl Zeiss, Inc., Thornwood, NY; Excitation range: 450-490nm; Emission range: 515-565nm) at 520nm.

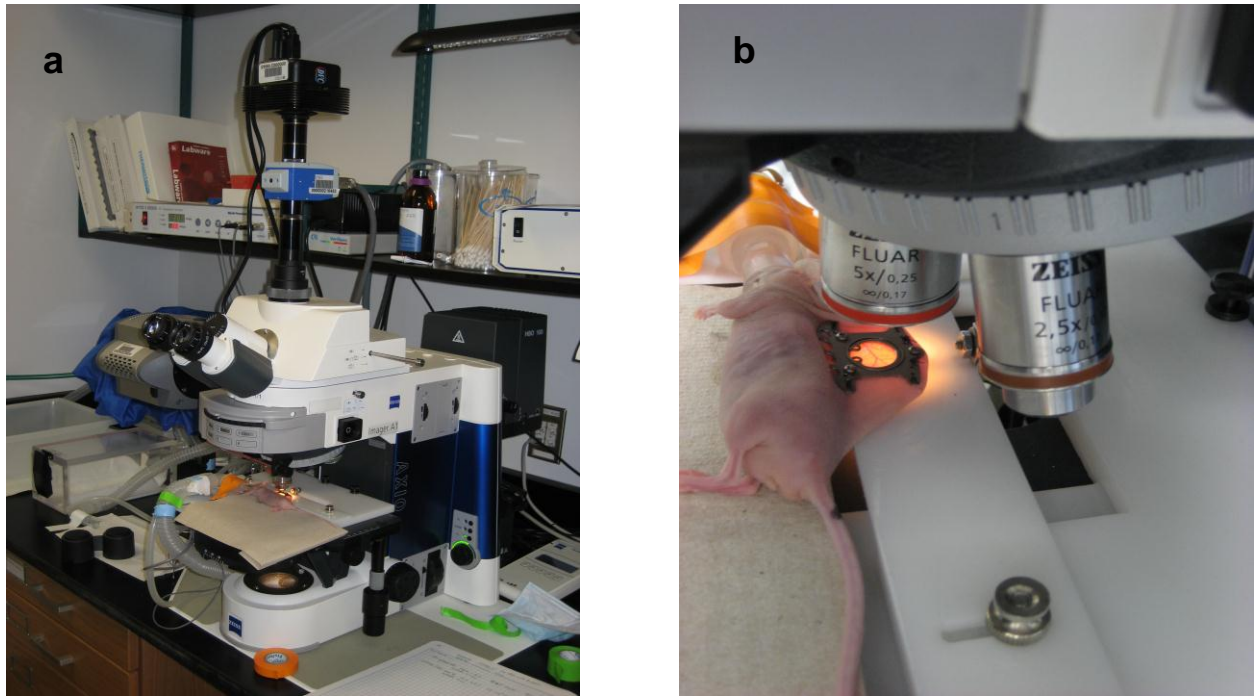


Figure 2-3. The Imaging system. The Zeiss-based imaging microscope system is shown in Figure2-2a. Figure 2-2b gives a close view of the mouse being imaged, placed on the heating pad and breathing through the nose cone.

Image Acquisition

LabVIEW8 (National Instruments Corp., Austin, TX) was used to prepare a custom designed virtual instrument for controlling the tuning of the LCTF filter and operation of the CCD camera. The software enabled automated image acquisition using the

specifications for camera exposure time and gain for each filter wavelength. Since the LCTF filter transmits less at lower wavelengths and more at higher wavelengths the exposure time for the camera had to be controlled such that the full dynamic range of the camera was utilized. The minimum exposure time used was 400ms whereas the maximum exposure time used was 1400ms, resulting in a typical acquisition time of approximately 16ms for image acquisition, filter tuning, image transfer, and saving images on external hard drive. One hemoglobin saturation image set comprised of 16 images acquired in the wavelength range of 500-575nm with an interval of 5nm.

Image Processing

Image processing was performed using Matlab software (The Mathworks, Inc., Natick, MA). The hyperspectral images acquired using the CCD camera and LCTF filter were converted into double-precision arrays for mathematical analysis. The mathematical analysis was based on Ross Shonat's method to solve for hemoglobin saturation (HbSat) using linear least squares regression[89]. The model equation used is the following:

$$OD(i) = eHbO2(i) * [HbO2] * L + eHbR(i) * (1 - [HbO2]) * L + LS \quad \dots\dots\dots Eqn(1)$$

Where,

OD = optical density (absorbance) at wavelength i (no units),

eHbO2 = extinction coefficient of oxyhemoglobin at wavelength i (1/(M.cm)),

[HbO2] = concentration of oxyhemoglobin (M) which is also the hemoglobin

saturation in this form of the equation,

eHbR = extinction coefficient of deoxyhemoglobin at wavelength i (1/(M.cm)),

L = pathlength (cm),

LS = scattering term (dimensionless here since it is the product of the pathlength and the scattering). In this equation, the scattering is handled in the LS term.

A rearrangement of the OD function results in the following:

$$\mathbf{OD(i)} = [(\mathbf{eHbO2(i)} - \mathbf{eHb(i)}) * \mathbf{HbSat} + \mathbf{eHb(i)}] * \mathbf{L} * \mathbf{HbTotal} + \mathbf{LS} \quad \text{.....Eqn(2)}$$

Where,

HbSat = hemoglobin saturation (= [HbO2]/ ([HbO2] + [HbR])), and

HbTotal = [HbO2] + [HbR].

If the following substitutions are made,

a = HbSat*L*HbTotal,

b = L*HbTotal,

c = LS,

eDelta(i) = eHbO2(i)-eHbR(i),

then the following equation results:

$$\% \mathbf{OD(i)} = \mathbf{eDelta(i)} * \mathbf{a} + \mathbf{eHbR(i)} * \mathbf{b} + \mathbf{c} \quad \text{.....Eqn(3)}$$

The function solves this equation for a, b, and c by linear least squares regression, and then solves for HbSat by performing a/b.

The image processing flow diagram is presented in Figure 2-4.

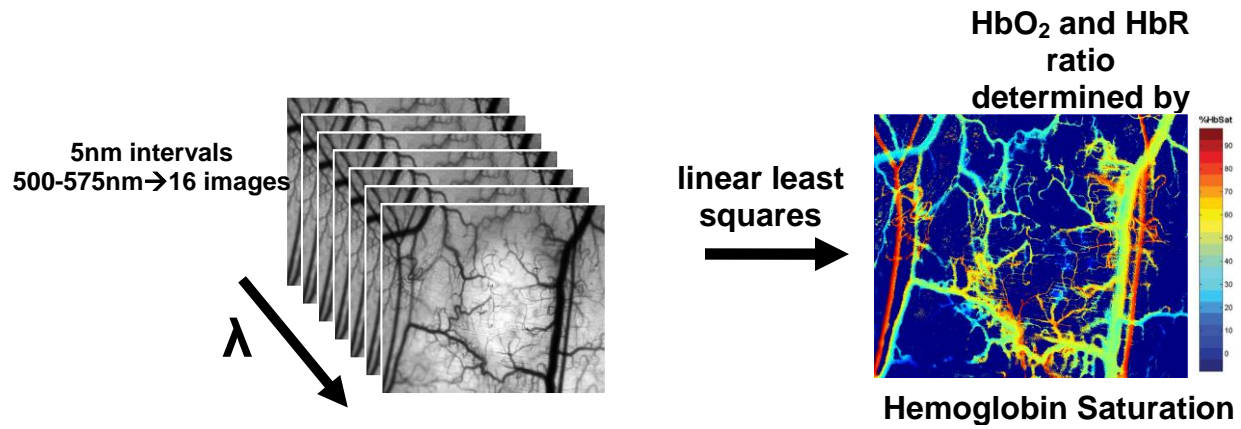


Figure 2-4. Flow diagram depicting the image processing method to obtain hemoglobin saturation map from the stack of 16 images obtained via spectral imaging.

Further details regarding the imaging system and image processing can be obtained from Sorg et al[90].

CHAPTER 3

SPECTRAL IMAGING OF WINDOW CHAMBERS: A VERSATILE TOOL FOR VASCULAR PATHOLOGY STUDIES

In the previous chapter an introduction to our mouse window chamber model and spectral imaging system was provided. This chapter will now furnish some of our data illustrating the versatility and utility of spectral imaging for study of microvasculature.

Abnormal vasculature, aberrant angiogenesis and oxygenation, or abnormal vascular remodeling are characteristic features of numerous pathologies. Qualitative and quantitative imaging and measurement of microvessel function may promote increased understanding of these diseases. Spectral imaging techniques can be effectively used for direct imaging of microvascular function.

We used spectral imaging to study microvasculature physiology and function in live mouse models of various pathological conditions such as cancer tumors, thrombosis, and arterio-venous malformations.

Introduction

Imaging and measurement of microvessel function can be important to increase understanding of various diseases. Numerous pathologies include hypervascularity, aberrant angiogenesis, or abnormal vascular remodeling among the characteristic features of the disease [91-93]. For example, the microvasculature of solid tumors is structurally and functionally abnormal [94, 95] foot ulcerations can occur in diabetes mellitus patients due to impaired angiogenesis and poor vascularization [96, 97] angiogenesis that forms abnormal microvasculature can sustain chronic inflammation in rheumatoid arthritis [98, 99] and epidermal hyperplasia is a characteristic of psoriatic skin lesions [100]. Many ophthalmic diseases, such as diabetic retinopathy and senile vascular degeneration, also have an underlying microvascular component [101, 102].

Several optical techniques are useful for direct imaging of microvascular morphology and function either clinically or in preclinical animal models. Intravascular fluorescence contrast agents can be used for imaging of microvessel morphology in some tissues with wide-field fluorescence imaging (e.g., retinal angiography with sodium fluorescein [103]) or multiphoton microscopy using dyes or quantum dots [104]. Multiphoton microscopy can also be used to measure microvessel blood velocity [105], permeability [106], and relative oxygenation [107] in animal models. Relative microvessel perfusion can be measured with laser Doppler and speckle contrast techniques [108, 109]. Photoacoustic tomography and microscopy can be used to measure microvascular morphology and relative vessel oxygenation [110, 111].[112]. Optical coherence tomography (OCT) can be a particularly versatile optical modality for microvasculature imaging and measurements. Blood velocity can be measured [113-115] with Doppler OCT, relative microvessel oxygenation can be measured with spectroscopic OCT methods [116-119], microvessel hematocrit can be measured from scattering attenuation by red blood cells [120], and speckle variance processing can provide contrast for microvessel morphology imaging [121].

Spectral imaging can be used to assess microvascular oxygen transport function in microvessel networks through measurements of hemoglobin saturation. Spectral imaging of microvessels with high resolution is limited to superficial tissue microvessels and the best results are often obtained invasively with animal models; thus, the utility of spectral imaging measurements of microvascular function may potentially be applied best in the preclinical setting. Depending on instrument capabilities and the animal model used, correlations in hemoglobin saturation can be obtained throughout a

microvessel network with high spatial and temporal resolution. Several researchers have used spectral imaging in preclinical models to measure microvascular hemoglobin saturation in mesentery tissue [122], cremaster muscle [123], rodent dorsal skin-fold window chambers [122-126], and cerebrum [109, 127]. In this chapter, we highlight novel observations made with our intravital microscopy spectral imaging system used with mouse dorsal skin-fold window chambers for imaging hemoglobin saturation in microvessel networks. Specifically, we image acute oxygenation fluctuations in a tumor microvessel network, the formation of spontaneous and induced microvascular thrombosis and occlusions.

Materials and Methods

Details about the mouse model and spectral imaging system can be found in previous chapter.

Methods for Tumor Vessel Acute Oxygenation Fluctuations

Preparation of fluorescent red blood cells

RBCs were fluorescently labeled by using a modification of the procedure by Unthank et al. [128]. RBCs obtained from donor mice were labeled with a 1 mg/ml stock solution of Carbocyanine dye 1,1'-dioctadecyl-3,3,3',3'-tetramethylindodicarbocyanine, 4-chlorobenzenesulfonate salt (DiD solid, Invitrogen, D-7757) dissolved in ethanol. DiD (excitation 644nm=emission 665nm) was chosen as the lipid membrane labeling solution because it is an analog of the commonly used Dil dye (ex 549nm, em 565nm), but with a markedly redshifted fluorescence excitation and emission spectrum to minimize interference of RBC flux measurements with hemoglobin saturation measurements (500–575nm). RBCs obtained by cardiac puncture from a donor mouse were washed twice via centrifugation and resuspension in phosphate buffered saline

(PBS). The cells were labeled by adding 100 μ l of cells and 100 μ l of DiD stock solution to 10 ml of sterile PBS. The solution was incubated at room temperature for 30 min and agitated every 10 min to ensure suspension of the RBCs. After labeling, the RBCs were washed to remove unbound dye and re-suspended in PBS. Immediately prior to an imaging session, a 50 μ l bolus of packed labeled cells in saline solution (30% V/V) was administered to the mouse to be imaged by tail vein injection. An aliquot of DiD labeled cells was saved for flow cytometric confirmation of the efficacy of the labeling procedure.

Preparation of 4TO7 tumor cells

We used 4TO7 mouse mammary adenocarcinoma cells that are non-metastatic subclones of the 4T1 cell line with athymic female nude (nu/nu) mice. The tumor cells were a gift from Mark W. Dewhirst, Duke University, Durham, North Carolina. The tumor cells were cultured as a monolayer in Dulbecco modified Eagle medium (DMEM; Mediatech, Manassas, Virginia) with 10% fetal bovine serum (Mediatech, Manassas, Virginia) prior to implantation. Cultures were used after one or two passages from frozen stocks to ensure recovery from the thermal shock and a normal growth rate. The cells were enzymatically dissociated from the flasks (BD Bioscience, San Jose, California) using 0.05% trypsin/EDTA (Mediatech, Manassas, Virginia) and counted on a hemacytometer to determine the cell concentration to prepare single cell suspensions for implantation. The 4TO7 tumors were established at the time of window chamber surgery from a 10 μ L single cell suspension of 5×10^3 to 10×10^3 cells injected into the subcutaneous tissue immediately prior to placing a 12-mm round glass coverslip over the exposed area of the skin.

Window surgery, in vivo tumor initiation and tumor imaging

A titanium window chamber was surgically implanted under anesthesia (ketamine 100 mg/kg IP (intraperitoneal) and xylazine 10 mg/kg IP) on the back of mice. In this window chamber model, one piece of skin was removed completely and replaced with a 12-mm-diam #2 round glass coverslip (Erie Scientific, Portsmouth, New Hampshire). For experiments with tumors, a window chamber tumor was established during chamber implantation by injecting 10 μ L of a single cell suspension of tumor cells. In survival experiments, animals were housed in an environmental chamber with free access to food and water and standard 12-h light/dark cycles.

For imaging, animals were placed on a heating pad attached to the microscope stage during the imaging session. A custom-built window chamber holder stably secured the window chamber under the microscope objective. The holder was fastened to the microscope stage in a manner that enabled the window chamber to be positioned under the microscope objective using the standard manual controls on the microscope stage. Anesthesia for immobilization during imaging was provided by isoflurane (1 to 1.5%) in air. In two experiments, an increase in convective oxygen transport was induced during imaging by a change in breathing gases from room air to 100% oxygen.

Image and data processing

Image processing was performed using software developed with MATLAB (The Mathworks, Inc., Natick, Massachusetts). Images were converted into double-precision arrays for mathematical processing. Raw pixel values were converted to absorbance values after manually selecting a vascular reference region in the images as estimates of unattenuated light.

Calibration spectra of oxy- and deoxyhemoglobin obtained with the imaging system were used to calculate pixel HbSat values by linear least-squares regression of the data in a linear mixing model according to the method of Shonat et al.[129] as described previously [90].

Red blood cell flux imaging

Fluorescently labeled red blood cells (RBCs) were imaged via streaming video using an Andor iXon electron multiplying CCD camera (Andor Technology, South Windsor, Connecticut). A Cy5 filter set was used (Chroma Technology Corp., Rockingham, Vermont, excitation 640nm with 20nm bandwidth, emission 680nm with 30nm bandwidth) in line with the illumination source of a Zeiss FluoArc mercury lamp. To optimize the resolution of the fast-moving cells, data were acquired in kinetic acquisition mode with 2×2 binning, using an exposure time of 16:2ms, a shift speed of 0:564 μ s, and a frequency of ~ 30 Hz to ensure that images would be captured with sufficient temporal resolution. Internal triggering was used to spool data directly to the computer hard drive, and 20 s of streaming video was saved every minute for 1 h in coordination with the acquisition of spectral imaging data sets. Each frame was saved as a tagged image format file (TIFF), resulting in a stack of 600 TIFFs per data point. RBC flux was determined by first identifying a region on a vessel of interest where flowing RBCs appeared to be in good focus and then manually counting the number of labeled cells flowing past the designated location on the vessel over the 20 s time interval of data acquisition for the time point. These measurements were converted to flux by correcting for the fraction of labeled RBCs versus unlabeled RBCs in the mouse blood. The fraction of labeled RBCs was determined by flow cytometry of a blood

sample obtained postimaging via retro-orbital puncture performed on the imaged mouse. The RBC flux was then calculated by using Eq. (4):

$$F_{RBC} = \frac{N_{RBC}}{t \left(\frac{N_{RBC, fluor}}{N_{RBC, Total}} \right)} \dots\dots\dots(4)$$

where,

N_{RBC} is the number of fluorescent RBCs counted flowing in the vessel,

t is the time interval in which N_{RBC} was counted (20 s in this case), and

$N_{RBC, fluor}$ and $N_{RBC, Total}$ are the number of fluorescent and total RBCs respectively, counted by flow cytometry in the post-experiment blood sample.

RBC velocity was determined from the time required for an individual RBC to travel a specific distance in the blood vessel that passed through the region of interest. The time interval was determined from the frame rate of fluorescence video imaging. The mean velocity of 5–10 randomly selected RBCs from each time point was taken as v_{avg} .

Methods for Induced Thrombus Experiments

Experiment design summary

The FeCl₃ was applied to the tissue with a piece of paper soaked with the solution (dotted outline in Figure 4-1). Venous thrombi gradually formed over approximately 20 min, resulting in a decreased oxygenation in the venules due to restricted and occluded blood flow. Figure 4-2 shows time series images of the region outlined by the small box in Figure 4-1, showing the gradual decrease in oxygenation of the venule as thrombi form over time. The HbSat values of the indicated region in Figure 4-2 at several time points are shown in Figure 4-3. Thrombus formation was independently confirmed by

the accumulation of fluorescently labeled platelets throughout the venules. Spectral imaging revealed the microvessel network oxygenation changes due to thrombi formation in the venules.

Imaging of thrombus formation was performed as part of experiments to test the antithrombotic activity of an angiotensin converting enzyme 2 (ACE2) activator compounds to stimulate purported antithrombotic activity of the ACE2/angiotensin- (1-7)/Mas axis [130, 131]. Vascular injury and thrombus formation were artificially induced to demonstrate the effect of the compounds by visualizing platelet adhesion and thrombus formation in real time.

Surgery

Dorsal skin-fold window chambers were surgically implanted on male athymic nude mice (nu/nu) of 9 to 10 weeks of age (Harlan Sprague Dawley, Indianapolis, Indiana) as previously described except that a coverslip was not installed for these terminal experiments. The exposed subdermal skin of the window chamber was maintained under warm saline at 37 °C throughout the experiment.

Platelet labeling and visualization

The jugular vein was cannulated for intravenous access. A bolus of 300 µL of carboxyfluorescein diacetate succinimidyl ester (Invitrogen, Carlsbad, California) was injected via the cannulated jugular vein to visualize platelets. The nonfluorescent precursor is taken up by platelets and somewhat by leukocytes where it forms the stable and highly fluorescent fluorophore carboxyfluorescein succinimidyl ester (CFSE) in the cells by intracellular cleavage of the acetate groups. The approximate excitation and emission peaks of CFSE are 492 and 517 nm, respectively.

Thrombus induction

Thrombus formation was induced using a protocol similar to Katayama et al. [132] via topical application for 2 min of 5% FeCl₃-soaked paper (3×3 mm) placed on the exposed sub-dermal skin region containing the vessel of interest. The piece of paper was removed after 2 min and the window was washed twice with warm saline.

Thrombus imaging

A vessel of interest with a 70- to 200- μm diameter was selected on the basis of un-restricted blood flow and location in the vessel network. Thrombus formation was monitored in real time by fluorescence and spectral imaging. Fluorescence video images were acquired every minute for 20 s at a 30-frames/s rate with an electronmultiplying CCD camera (Andor Technology, South Windsor, Connecticut) and a spectral imaging data set for hemoglobin saturation measurements was acquired once every minute, as described previously. Imaging sessions lasted for 20 to 25 min.

Methods for Arterio-venous Malformation Experiments

Experiment design summary

Imaging of pathological anastomoses formation in the form of arteriovenous malformations was performed using a mouse model of hereditary hemorrhagic telangiectasia (HHT). In this mouse model, the activin-receptor-like kinase 1 (Alk1) gene is designed to be deleted by administration of tamoxifen. Details about the generation of the Alk1 conditional knockout mice were described previously [133]. Conditional Alk1 knockout (Alk1^{2f/-}) mice were intercrossed with ROSA26^{CreER/+} mice that ubiquitously produce CreER that is a fusion protein of Cre recombinase and a mutated form of the estrogen receptor that can be activated by tamoxifen. The experimental group included

mice with ROSA26^{CreER/+} ; /Alk1^{2f/2f} and ROSA26^{CreER/+} ;Alk1^{2f/-} genotypes while the control groups were ROSA26^{+/+} ;Alk1^{2f/2f} and ROSA26^{+/+} ;Alk1^{2f/-} mice.

Window chamber wound model

Window chambers were surgically installed as already described, and a wound was created in an avascular area between vessel branches in the center of the window chamber using a 16-gauge needle during surgery. Oil-based tamoxifen (Sigma-Aldrich, St. Louis, Missouri) was administered intraperitoneally at 2.5 mg/25 g bodyweight to control and knockout mice immediately prior to window chamber installation.

Spectral imaging

Mice were imaged as already described almost every day for up to 11 days after surgery.

Blood flow imaging

Blood flow through suspected arteriovenous malformations (AVMs) from arterioles to venules was confirmed by tracking fluorescently labeled red blood cells (RBCs). Blood from a donor mouse was labeled with the carbocyanine dye 1,1-dioctadecyl-3,3,3,3-tetramethylindodicarbocyanine, 4-chlorobenzenesulfonate salt (DiD solid, Invitrogen, D-7757) similar to the procedure used by Unthank et al [128]. A 50µL bolus of packed labeled RBCs in saline solution (30% v/v) was administered by tail vein injection 1 to 2 days prior to imaging. It was determined from previous experiments that for the fraction of labeled cells achieved in vivo with this protocol (1 to 3%), there was negligible absorption interference of the dye with the spectral data obtained for hemoglobin saturation in the wavelength range employed 40 (500 to 575 nm).

Results

Tumor Microvascular Acute Oxygenation Fluctuations

Abnormal tumor microvasculature with compromised oxygen transport is known to be a major cause of hypoxia in tumors [31, 95, 134]. The biology of tumor cells may be different depending on whether they are exposed to chronic hypoxia or acute hypoxia with subsequent reoxygenation [135]. Acute fluctuations in blood flow and oxygen supply that are significant enough to cause hypoxia are becoming more appreciated for their effects on tumor biology and therapy as even relatively short hypoxic episodes can have a potentially profound effect [136, 137]. For example, it has been recently reported that tumor metastases have a higher fraction of acutely hypoxic cells than chronically hypoxic cells, implying that acutely hypoxic cells have a higher metastatic potential and greater probability of impact on therapeutic response [138].

Research to characterize acute fluctuations in tumor microvessel oxygenation and perfusion requires advanced imaging techniques with microvessel resolution [139]. Spectral imaging of tumor microvessel oxygenation may be a useful tool in this effort. We previously showed that spectral imaging could be used to measure acute fluctuations in tumor microvessel oxygenation [140]. We further demonstrate here how spectral imaging can document acute fluctuations in tumor microvessel oxygenation and reveal an apparent sensitivity in a tumor microvessel network to supply vessel oxygenation fluctuations.

Figure 3-1 shows a 4TO7 tumor with a diameter of 1.5 to 2.0 mm 9 days after implantation of cells. Temporal spectral data was collected every minute for 1 hour. Figure 3-2 shows the HbSat image created from one set of spectral data from the data in Figure 3-1. Also, red cell flux data was obtained simultaneously every minute for 1

hour. An example figure is shown in Figure 3-3. The regions of interest (ROIs) chosen for HbSat measurement are indicated in the figures by numbered white squares in Figure 3-1. RBC flux was calculated after counting the number of labeled RBCs flowing in the vessels close to the ROIs of interest. The plot of HbSat values and RBC flux versus time is shown in Figure 3-4 and Figure 3-5. Correlation between the RBC flux and HbSat can be observed.

These results demonstrate that fluctuations in microvessel oxygenation with the potential to cause hypoxia can occur in tumors of a relatively small size. The results also suggest that a potential source of instability in tumor microvessel oxygenation may be due to an exaggerated response in the tumor vessels to oxygenation fluctuations in the tumor supply vessels. Gaustad et al. showed that tumor feeding vessels can have a significant influence on local perfusion of tumor microvessel network regions [141], thus, some correlation between tumor supply vessels and regions of tumor microvessel networks could be expected. In previous publications, we showed that in tumors there could be direct connections between well and poorly oxygenated microvessels [140, 142]. If these connections were present in the tumors used in this study, then it is possible that dynamic changes in blood flow through these connections contributed to the large swings in microvessel oxygenation.

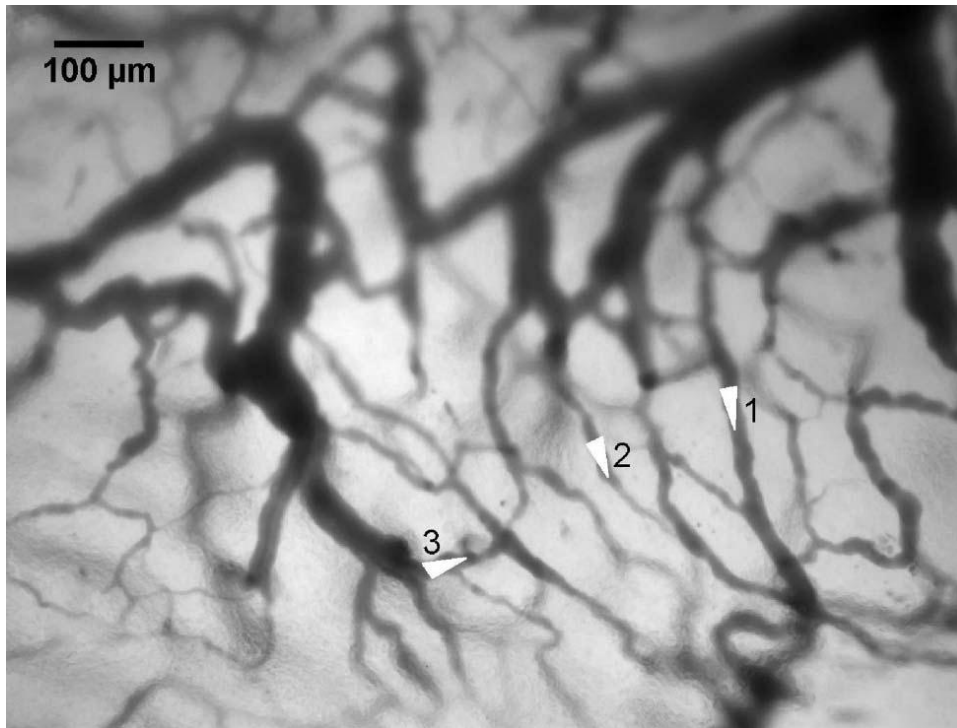


Figure 3-1. Transmitted light image of the tumor microvessel network. It is a 4T07 mouse mammary carcinoma with a diameter of 1.5 to 2.0 mm 9 days after implantation of cells. White triangles represent regions of interest chosen for analysis. A 10x objective was used for imaging (NA of 0.3, working distance of 5.5 mm).

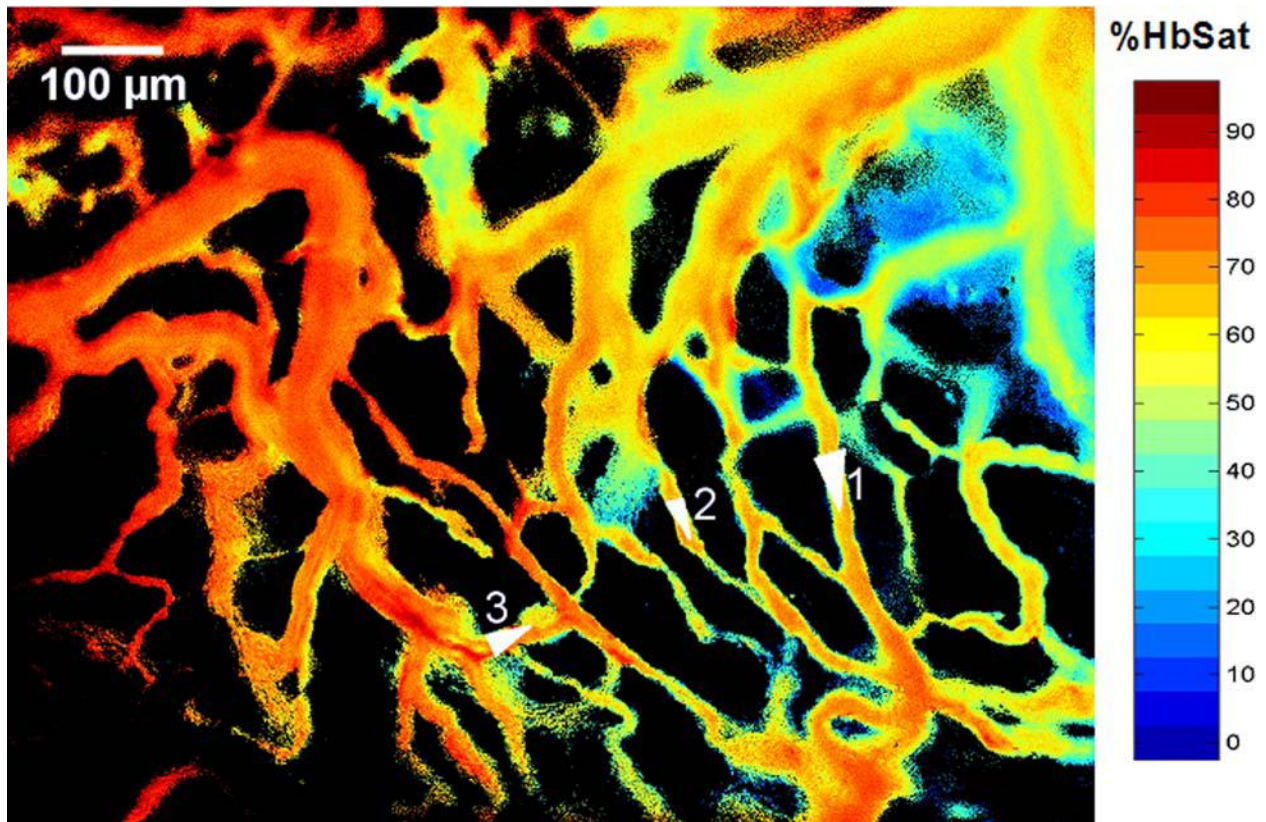


Figure 3-2. Hemoglobin saturation image of the tumor microvessel network in Figure 3-1. The pixels are colored according to the hemoglobin saturation scale to the right of the figure. The background is black. Regions of interest for analysis are indicated in the figure.

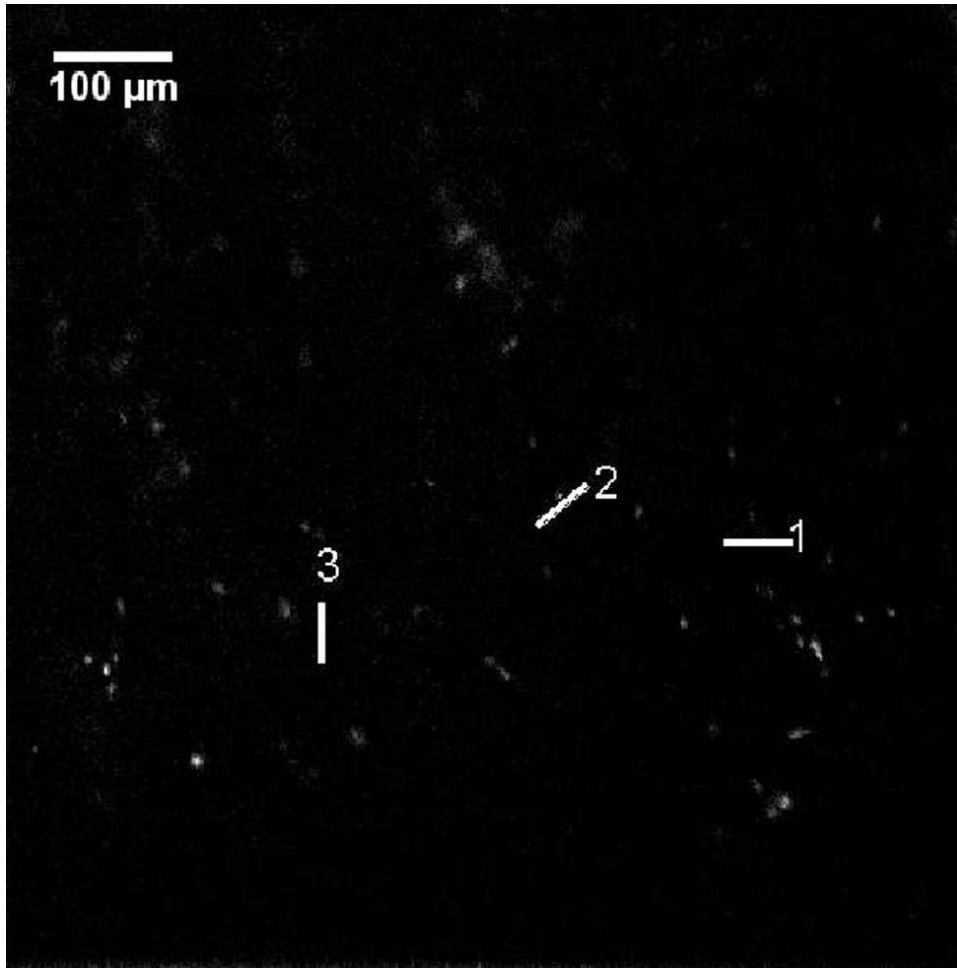


Figure 3-3. Fluorescence image of RBCs labeled with DiD flowing in the tumor microvessel network. Images were captured with an electron multiplying CCD camera at video rates (30 Hz). 20 s of data were taken every minute of the hour-long imaging session, and cells were counted over this time increment and then converted to RBC flux measurements. The locations of the regions of interest for analysis are indicated in the figure.

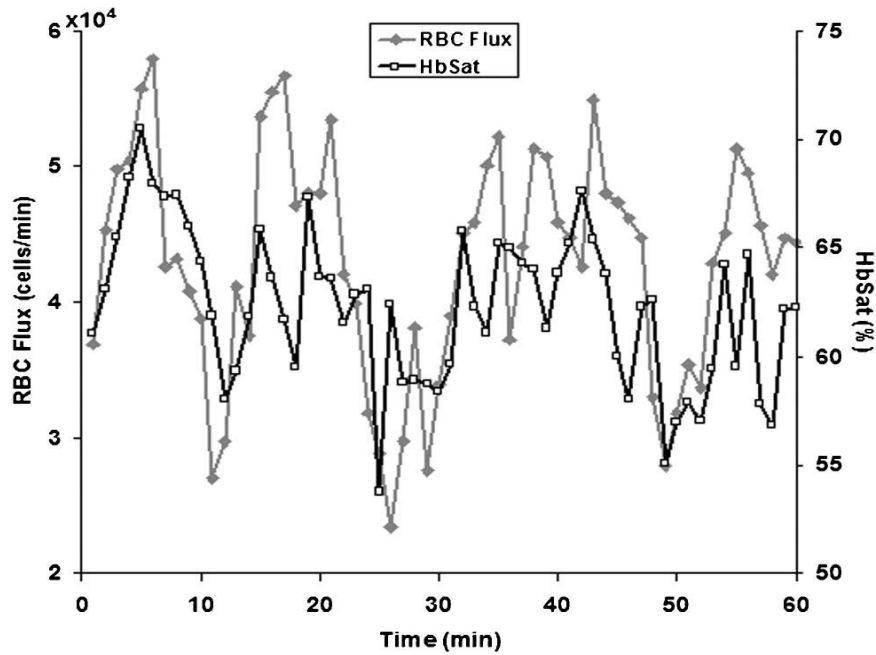


Figure 3-4. Plot of RBC flux versus hemoglobin saturation (HbSat) for region of interest 1 in Figure 3-1. The data points were acquired at 1 min intervals for 1 h.

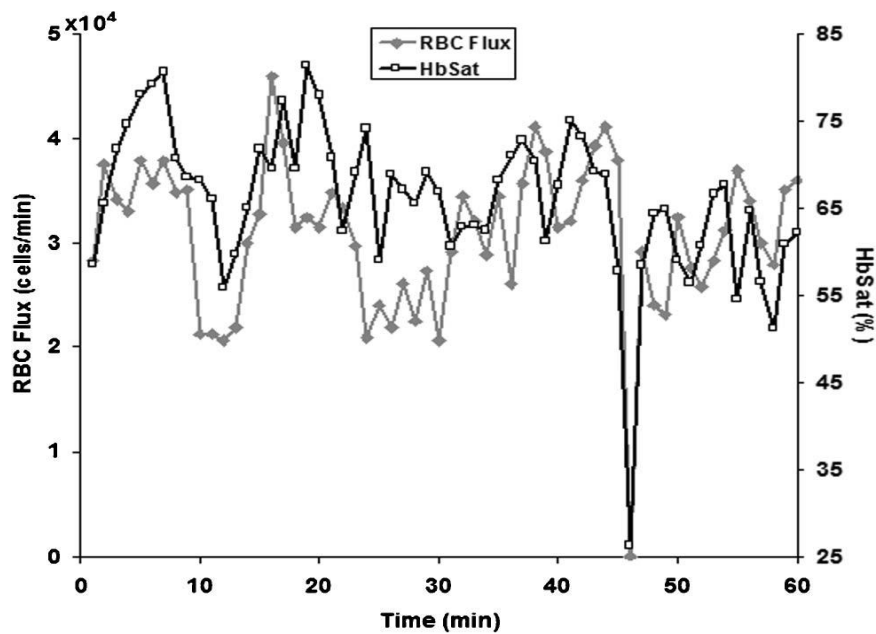


Figure 3-5. Plot of RBC flux versus hemoglobin saturation (HbSat) for region of interest 3 in Figure 3-1. The data points were acquired at 1 min intervals for 1 h.

Spectral Imaging for Study of Microvascular Occlusions

Blood vessel occlusions due to thrombus formation can occur in disease and pathophysiological processes. In cardiovascular disease, the eruption of an atherosclerotic plaque can initiate arterial thrombus formation leading to myocardial infarction [143]. There can be a risk of deep vein thrombosis formation after some types of surgery or trauma, or in patients with various disorders of the coagulation system [144]. Imaging of microvasculature in preclinical models can potentially be useful for testing and evaluation of new thrombolytic drugs to dissolve thrombi or thromboprophylaxis agents aimed at preventing thrombus formation. Dorsal skin-fold window chambers were used with spectral imaging as part of an investigation into the antithrombotic activity of a novel ACE2 activating agent [145, 146].

Dorsal skin-fold window chambers were used with spectral imaging as part of an investigation into the antithrombotic activity of a novel ACE2 activating agent. Figure 3-6 shows brightfield and HbSat images of a region of tissue in a mouse immediately prior to and 21 min after thrombus formation initiated by topical application of FeCl₃. The FeCl₃ was applied to the tissue with a piece of paper soaked with the solution (dotted outline in Figure 3-6). Venous thrombi gradually formed over approximately 20 min, resulting in a decreased oxygenation in the venules due to restricted and occluded blood flow. Figure 3-7 shows time series images of the region outlined by the small box in Figure 3-6, showing the gradual decrease in oxygenation of the venule as thrombi form over time. The HbSat values of the indicated region in Figure 3-7 at several time points are shown in Figure 3-8. Thrombus formation was independently confirmed by the accumulation of fluorescently labeled platelets throughout the venules. Spectral

imaging revealed the microvessel network oxygenation changes due to thrombi formation in the venules.

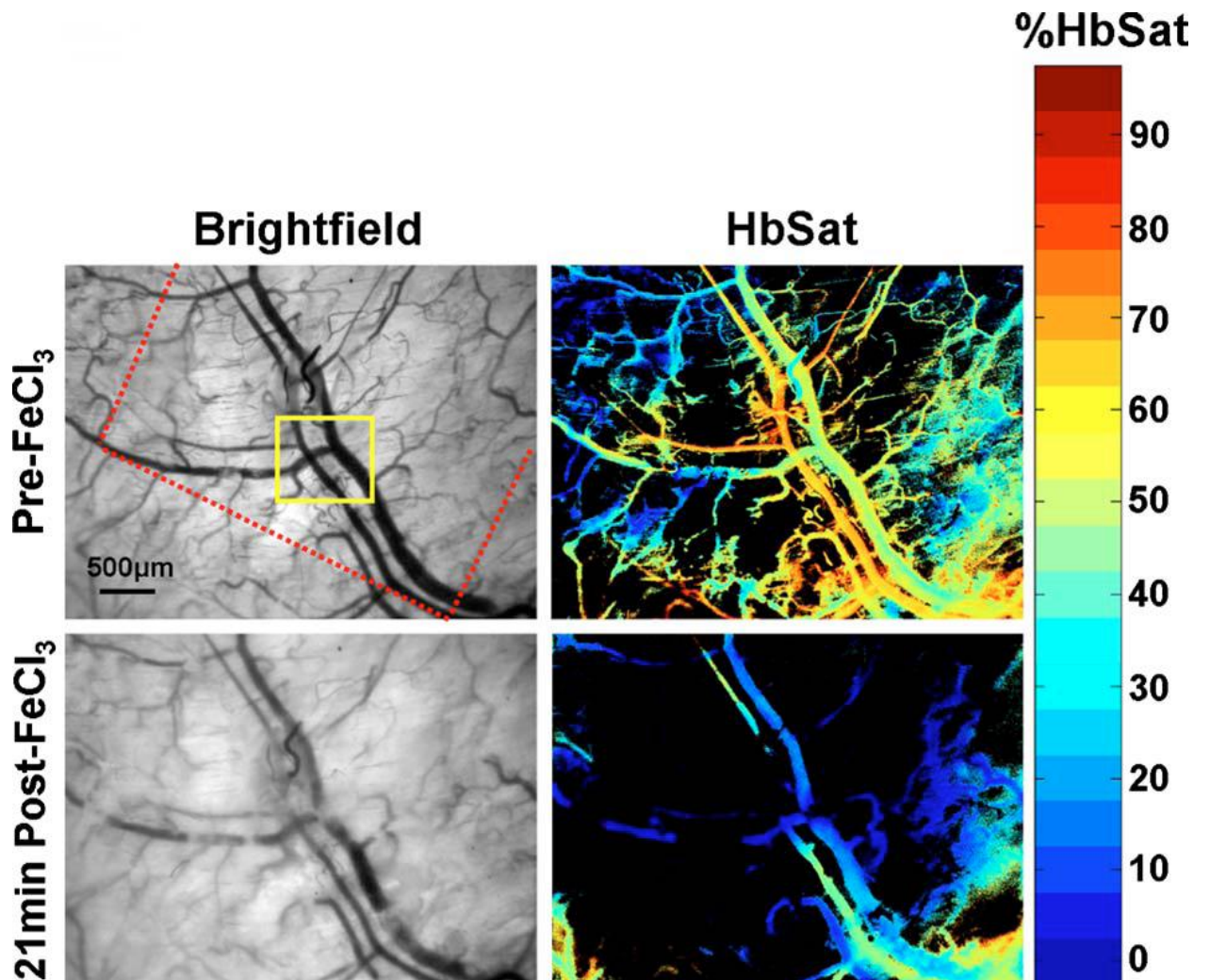


Figure 3-6. Brightfield and HbSat images are shown before and 21 minutes after topical application of FeCl₃ to induce thrombus formation. The red dotted line in the top left image indicates where the border of the paper soaked with FeCl₃ was relative to the image area. The yellow box indicates the region shown in the images in Figure 3-7 at higher magnification.

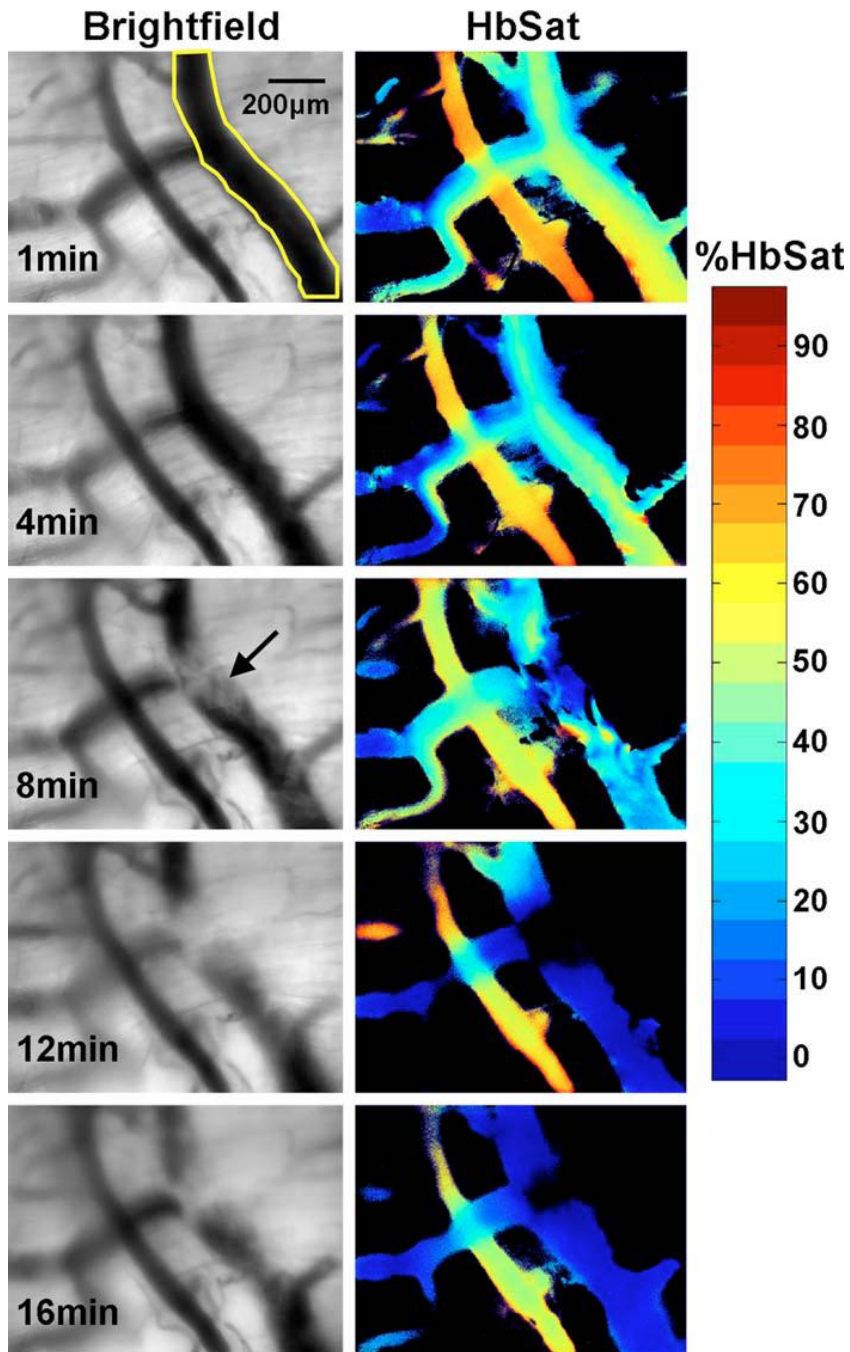


Figure 3-7. Brightfield and HbSat time sequence images of thrombus development for the region indicated by the yellow box in Figure 3-6. The yellow outlined area on the venule in the top left image indicates the ROI used for the HbSat measurements shown in Figure 3-8. The arrow in the brightfield image at the 8-min time point indicates a forming thrombus.

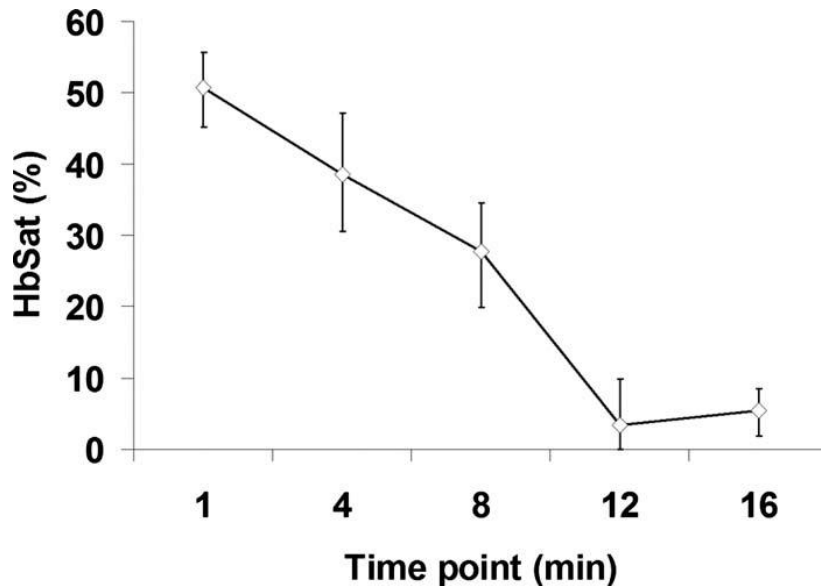


Figure 3-8. Plot of the HbSat in the ROI indicated in Figure 4-2 at various time points during thrombus development. The data points in the figure are given as the median \pm interquartile range for the ROI.

Spectral Imaging for Real-Time Imaging of Arterio-Venous Malformations

Arteriovenous (AV) anastomoses are direct connections between the arterial and venous circulation without an intervening capillary bed. These connections can be created surgically in larger vessels for a therapeutic purpose such as assistance in the treatment of hemodialysis patients [147]. AV anastomoses are naturally present in the microcirculation of some normal tissues with highly variable blood flow, such as skin [148] and nasal mucosa [149], but they can also arise pathologically as part of a disease process. Tumor microvasculature can develop a substantial number of pathological AV anastomoses [150]. A high percentage of HHT patients can develop AVMs in the brain, lungs, liver, and gastrointestinal tract that can potentially rupture with devastating consequences [175,176]. In addition to these visceral AVMs, a majority of

HHT patients develop telangiectases in mucocutaneous areas, such as the nasal cavity, that result in spontaneous nose bleeding [177].

To study the development of skin AVMs, we developed a mouse model using the Alk1 gene by intercrossing ROSA26^{CreER/+} mice with Alk1-conditional knockout (Alk1^{2f/-}) mice [133]. We have shown that a wound can induce de novo AVMs in its surroundings in adult ROSA26^{CreER/+};Alk1^{2f/-} mice (Alk1 mutants hereafter) administered with tamoxifen.

To study the development of skin AVMs, we developed a mouse model using the Alk1 gene by intercrossing ROSA26^{CreER/+} mice with Alk1-conditional knockout (Alk1^{2f/-}) mice [133]. We have shown that a wound can induce de novo AVMs in its surroundings in adult ROSA26^{CreER/+};Alk1^{2f/-} mice (Alk1 mutants hereafter) administered with tamoxifen. Figure 3-9 shows AVM development at selected time points stimulated by wound healing in the Alk1 mutants. The regions where two AVMs form are indicated in the figure. Venules near the wound had increased oxygenation and diameters after surgery due to AVM formation. Veins and venules, the most distensible of the blood vessels, are sensitive to pressure changes and can markedly dilate with small increases in pressure [151]. The increase in venule oxygenation was observed prior to the appearance of a clearly identifiable AVM with brightfield or spectral imaging.

Confirmation of a direct connection between arterioles and venules through AVMs was obtained by tracking the flow of fluorescently labeled RBCs administered via tail vein injection after spectral imaging. Tracking fluorescently labeled RBCs also enabled visualization of the earliest connections between arterioles and venules through sprouting vessels that eventually formed AVMs, suggesting that the vascular changes

seen in the brightfield and spectral images were induced by these connections. In the Alk1 mutants, relatively few nascent sprouts developed at the perimeter of the wound.

There was extensive formation of stable AVMs that resulted in significant changes in the microvasculature adjacent to the wound, including major arterioles and venules, that persisted after the wound had healed. Wound healing occurred within the same time frame as control animals. Figure 3-10 shows wound healing at selected time points in control animals with functional Alk-1. Extensive formation of nascent sprouts occurred around the periphery of wounds in control animals during wound healing, but they subsided after the wound was healed. There were minor changes in the oxygenation and morphology of major vessels and after wound healing the microvasculature returned to a more normal state. In contrast to the Alk-1 deletion mice, no AVMs formed in control mice and venule oxygenation in control mice was less than in Alk-1 deletion animals. This point is illustrated in Table 3-1. Arteriole and venule ROIs were evaluated on different days (n=9 for Alk-1 deletion, n=7 for control). The ROIs were located in areas near the arrow heads identifying the different vessels in Figs. 3-9 and 3-10. For the mice in the figures, the arterioles had similar average saturations throughout the observation period but the Alk-1 deletion mice had statistically higher venule saturation (see Table 3-1).

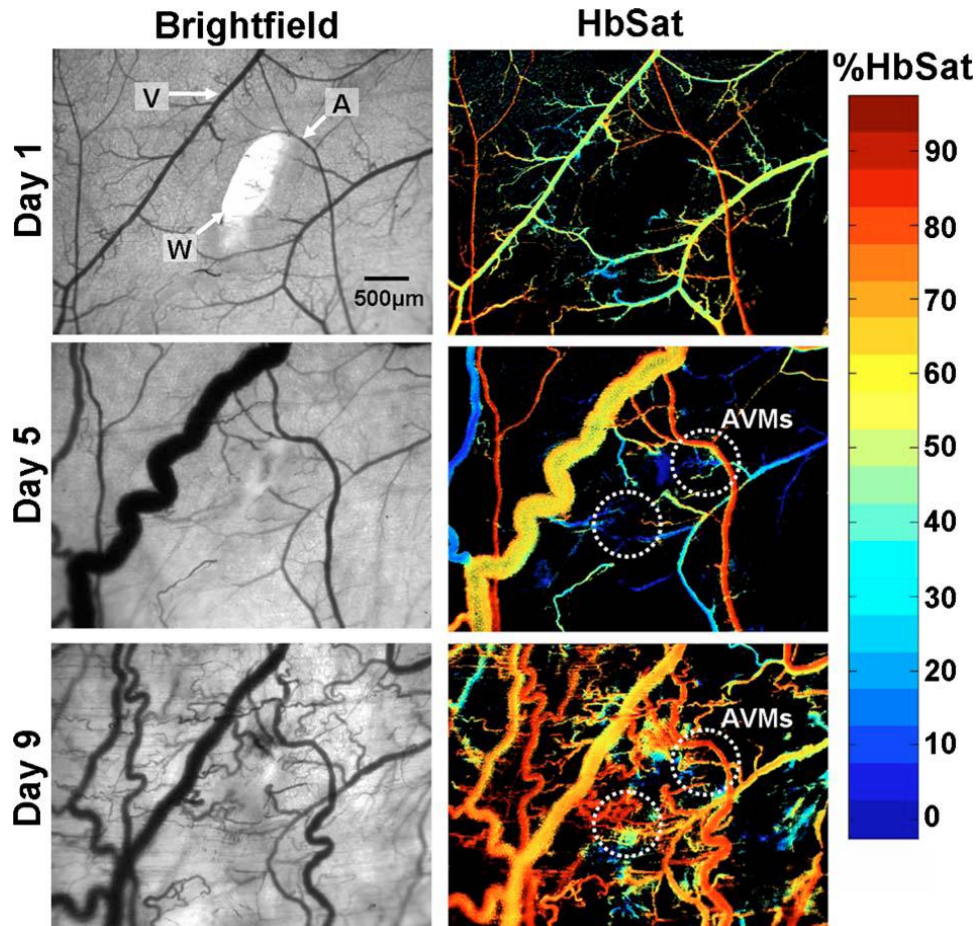


Figure 3-9. AVM development in a conditional Alk1 deletion mouse ($\text{ROSA26}^{\text{CreER}}/\text{Alk1}^{2f/-}$) stimulated by a wound, where A, arteriole; V, venule; and W, wound. The left column shows transmitted light images and the right column shows HbSat images. Region where AVMs formed is indicated in the day 5 and day 9 images. At day 5, the AVM connections were not obvious but clear changes in venule oxygenation could be seen due to the AVMs. The arrowheads indicating the arteriole and venule also indicate regions of interest where HbSat measurements were obtained.

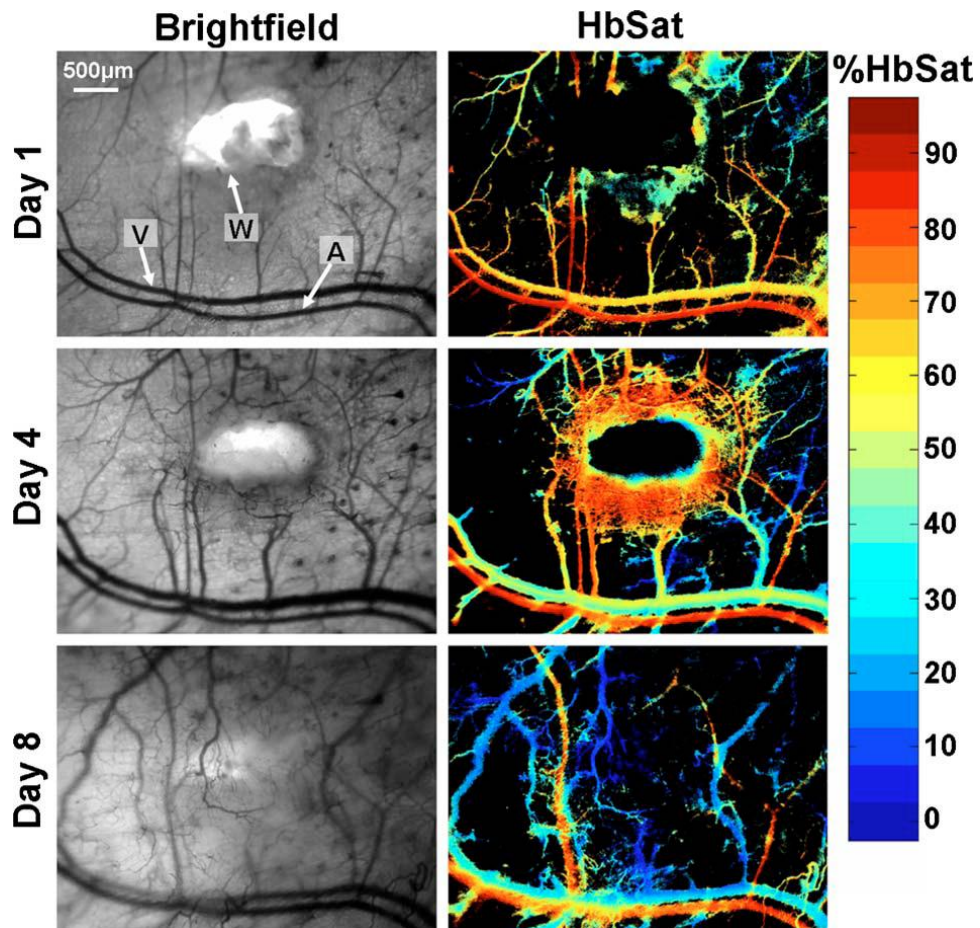


Figure 3-10. Wound healing in a control mouse: A, arteriole; V, venule; and W, wound. The left column shows transmitted light brightfield images and the right column shows HbSat images. The arrowheads indicating the arteriole and venule also indicate regions of interest where HbSat measurements were obtained. Unlike the conditional *Alk1* deletion mouse in Figure 3-9, no AVMs formed during wound healing.

| | HbSat (%) ^a | |
|-----------------------------|------------------------|----------------------|
| | Arteriole | Venule |
| Control (n=9) | 81 ± 5 ^b | 47 ± 12 ^c |
| <i>Alk-1</i> deletion (n=7) | 82 ± 3 ^b | 64 ± 6 ^c |

^aMean ± st dev
^bNot statistically significant
^cStatistically significant (t test, p < 0.005)

Table 3-1. Comparison of arteriole and venule saturation in a mouse model of HHT during wound healing.

Discussion

Several optical techniques are useful for direct imaging of microvascular morphology and function either clinically or in preclinical animal models. Spectral imaging can be used to assess microvascular oxygen transport function in microvessel networks through measurements of hemoglobin saturation. Spectral imaging along with fluorescence imaging techniques was used to study the tumor vessel oxygenation and RBC flux simultaneously as shown in Figures 3-1-5. These results indicate that oxygenation fluctuations are prevalent in even millimeter size tumors which may potentially lead to acute hypoxic conditions in tumors. The study of RBC flux together with HbSat of the vessels gives insights regarding the relationship between the blood supply and transportation.

Dangerous and debilitating thrombus formation can be caused by pathological conditions such as diabetes, hypertension, and atherosclerosis [178]. Thrombi induced from these and similar pathological conditions can result in strokes, pulmonary emboli,

and deep venous thrombi among other conditions [178]. Spectral imaging of hemoglobin saturation showed the gradual formation of chemically induced thrombi and the effects of the thrombi on microcirculation oxygenation in Figures 3-6–9. The time for thrombus formation and complete microvessel occlusion could be measured from these experiments, and these data may provide additional information besides systemic physiological measurements with which to assess local microvessel physiology during a thrombotic event. Real-time imaging of thrombus formation and changes in microvascular oxygenation can aid in the development and comparison of new therapeutic agents designed to treat pathological thrombi by revealing subtle differences in the timing and magnitude of drug action on the microvessel physiological response and thrombus formation.

Spectral imaging in a mouse model of HHT in Figures 3-9-10 and Table 3-1 document the consequences of AVM development in real time. Microvessel oxygenation changes during AVM development indicated that AVM formation occurred at early time points following angiogenesis stimulation by wound creation, and suggested that the formation of the AVM induced changes in microvascular morphology and function, particularly in the venules. Venules connected to arterioles through AVMs rapidly became dilated and hyperoxygenated compared to normal venules. The changes in venule oxygenation were frequently apparent prior to the appearance of a clearly identifiable AVM. This is important because previous histologic examination of tissue specimens suggested [179,180] that the opposite was the case—that dilation of microvessels initiated or at least preceded development of AVMs. A clearer understanding of the causes and consequences of AVM formation and tracking the

timing of AVM formation may aid in the development of therapies to better treat diseases that exhibit this pathology. Our imaging technique may aid in understanding the causes of AVM formation and other vascular pathologies at the molecular and genetic level using genetically altered mouse models such as the one employed in this study. A more detailed description of the animal model and characterization experiments with this model can be found in a paper by Park et al [152].

CHAPTER 4 OXI4503 TREATMENT OF 4T1 AND CAKI-1 TUMORS

Introduction

Tumor vasculature is essential for tumor growth, proliferation and metastasis, hence numerous methods have been developed to impair tumor vessels with the intent of cutting off the tumor blood supply and access to oxygen and nutrients. An array of specific tumor vessel targeting strategies emerged after Denekamp et al distinguished tumor endothelial cells from normal tissue endothelial cells based on their significantly higher proliferation rate [153, 154]. Currently, a number of vascular targeting approaches are in development for selective and specific targeting of the tumor vessels while sparing the normal tissue vasculature [12-16, 54].

Vascular disrupting agents (VDAs) are designed to damage existing tumor blood vessels while antiangiogenic therapies such as bevacizumab aim to inhibit new blood vessel formation [17]. Combretastatins, initially derived from the South African tree *Combretum caffrum*, represent a class of potent tubulin binding agents with significant vascular disrupting activity [15, 155]. Lead agents Combretastatin A4-P (CA4-P) and OXi4503 (CA1-P) have been shown to result in time-dependent decreases in tumor perfusion, increased tumor vascular permeability, and significant tumor vascular damage in a wide variety of preclinical tumor models [15, 27-29]. In the clinic, these agents have now entered Phase II/III evaluation [156, 157].

Despite extensive tumor destruction following VDA therapy, a hallmark of VDA treatment is the survival of neoplastic cells at the tumor periphery [156]. This surviving 'viable rim' can lead to subsequent tumor reperfusion and regrowth following drug treatment [28, 158]. In preclinical models and some clinical studies, functional and

morphological parameters such as tumor perfusion, blood flow, vascular structure, permeability and vascular damage are used to evaluate the effect of OXi4503 and CA4-P on tumor and normal tissue [28, 69, 70, 71, 158]. Some of the methods used cannot furnish continuous real-time in vivo information as they require animal euthanasia at the respective time-points and do not permit serial follow-up of the same tumor after VDA treatment. Hence, several different techniques are used for the in vivo assessment of VDA-induced functional and morphological changes in murine and human tumor vasculature. For example, Sheng et al used microsphere fluorescence to assess in vivo tumor blood flow in murine flank tumors after OXi4503 treatment [27]. Other techniques such as magnetic resonance imaging and positron emission tomography can provide functional information regarding blood flow, tumor perfusion, and vascular permeability [72, 158], however, with poor microvascular resolution. In vivo microscopy techniques such as multi-photon fluorescence microscopy in a window chamber model have been employed by Tozer et al which provides vascular function data with improved microvessel resolution [73], and can be used to simultaneously observe serial morphological changes after VDA treatment.

Spectral imaging is an effective tool for measurement of microvessel vessel oxygenation in tumor microvasculature [74, 90, 140]. The oxygenation of a vessel depends on several factors such as hemoglobin saturation (HbSat), perfusion and red cell flux [74, 159]. In the present study, spectral imaging is used with mouse dorsal skin-fold window chambers to measure microvascular functional changes in terms of HbSat in two different tumors, a mouse mammary carcinoma (4T1) and human renal cell carcinoma (Caki-1), during serial treatments with the VDA OXi4503.

Materials and Methods

Tumor Cells

4T1 mouse mammary adenocarcinoma cells (a gift from Mark W. Dewhirst, Duke University Medical Center, Durham, NC) were cultured in DMEM (Cellgro, Inc., 1X, 4.5 g/l glucose, L-glutamine and sodium pyruvate) containing 10% fetal bovine serum (Biowhittaker, Inc.), 1% L-glutamine (Clonogen, Inc.) and 1% penicillin streptomycin (Clonogen, Inc.). A single cell suspension of approximately 5×10^3 to 10×10^3 cells prepared in serum-free DMEM was used to initiate tumors in window chambers of the experimental mice.

Caki-1 tumor xenografts [29] were initiated in a single hind limb of donor mice by inoculating with 2×10^5 to 5×10^5 tumor cells. Tumors were excised when they reached about 200 mm^3 in size, and a single cell suspension was prepared in DMEM. About 1×10^6 cells were used to initiate a window chamber tumor in the experimental mice.

Animal Model

All in vivo procedures were conducted in accordance with a protocol approved by University of Florida Institutional Animal Care and Use Committee. Athymic (nu/nu) female mice weighing at least 21 g (Charles River Laboratories, Raleigh, NC) were surgically implanted with a titanium window chamber on the dorsal skin flap. During surgery mice were anesthetized by an IP injection of ketamine (100 mg/kg) and xylazine (10 mg/kg). A tumor was initiated in the window chamber during surgery by injecting the tumor cells subcutaneously in the dorsal skin flap prior to placing a 12-mm diameter no. 2 round glass coverslip (Erie Scientific, Portsmouth, NH) over the exposed skin. After surgery animals were housed in an environmental chamber maintained at 33°C and 50% humidity with free access to food and water and standard 12-h light/dark cycles.

Drug Preparation and Experimental Design

OXi4503, a gift from OXiGENE, Inc. (Waltham, MA) was administered at a dose of 10 mg/kg IP (0.01 ml/g of mouse body weight). The light-sensitive drug was protected from light during handling. OXi4503 was suspended in a solution of sterile saline and 50 μ l per ml of 5% sodium carbonate solution before injection. The drug was prepared fresh daily. Control groups received an equivalent volume of sterile saline and 5% sodium carbonate solution. The tumors were allowed to grow for 7-8 days and the treatment was started when tumors reached a size of about 3-4 mm. Spectral imaging was performed immediately prior to and post-treatment, and also at 2, 4, 6, 8, 24 and 48 h post-treatment. After the 48-h imaging time point the mouse was re-treated and the same imaging schedule was maintained. The treatment was repeated 3-5 times on each of the experimental mice. In all, 5 mice bearing 4T1 tumors were treated with OXi4503 and 3 mice were carrier only controls. For Caki-1 tumors the OXi4503 treatment was performed on 5 mice, while 2 mice received carrier only minus drug.

Imaging System, Image Acquisition and Image Processing

The spectral imaging system, image acquisition, and image processing methods for hemoglobin saturation measurements were discussed in detail previously [160]. Briefly, a Zeiss Axiolmager microscope (Carl Zeiss, Inc., Thornwood, NY) was used as a basic platform for the imaging system. For transillumination images, a 100-W tungsten halogen lamp was used. The long working distance objectives used were 2.5 \times and 5 \times Fluars, 10 \times EC Plan-NeoFluar and 20 \times LD-Plan-NeoFluar (Carl Zeiss, Inc.). For spectral information, brightfield transmitted light images were obtained using a CCD camera thermoelectrically cooled to -20 $^{\circ}$ C (DVC Co., Austin, TX; Model no.1412AM-T2-FW). Band-limited optical filtering was accomplished using a C-mounted liquid crystal

tunable filter (CRI, Inc., Woburn, MA) with a 400- to 720-nm transmission range and a 10-nm nominal bandwidth, placed in front of the CCD camera. LabVIEW8 (National Instruments Corp., Austin, TX) was used to automatically control the tuning of the LCTF and acquire images with the CCD camera. Microvessel hemoglobin saturation measurements and images were created from the spectral image data [89, 90].

Results

During each treatment the tumor vasculature experienced two distinct phases: a destruction phase closely followed by a recovery phase. The treatment resulted in a combination of three major effects on the tumor vasculature: i) transient vessel collapse, ii) permanent vessel disintegration or iii) no structural damage with only temporary functional loss. Transient vessel collapse refers to the temporary disappearance of the tumor core vessels during the destruction phase of each treatment. These original tumor vessels re-emerged during the recovery phase and regained their functionality.

Tumor core vasculature that underwent vessel disintegration never reappeared and in some cases there was evidence of hemorrhaging. Some tumor vessels as well as the normal vasculature did not suffer from structural damage but still manifested temporary oxygenation changes.

Treatment of 4T1 Mouse Mammary Carcinomas

Each 4T1 tumor-bearing mouse (n=5) received 3 serial treatments of OXi4503 administered every 48 h. Figure 4-1 shows a typical 4T1 tumor treatment progression. Prior to OXi4503 administration, the tumor vessels as well as the normal vasculature were intact and functional with ample oxygenated blood supply (Figure 4-1A, B). At 2-h post OXi4503 treatment, structural collapse of the tumor vasculature was observed (Figure 4-1E) accompanied with significant reduction in oxygenation (Figure 4-1F) with

initiation of minor vessel breakdown in some areas of the tumor. Progressive vessel disintegration advanced from the tumor core towards the periphery between 2-8 h post-treatment resulting in functional loss in the tumor core (disintegrated vascular network highlighted in Figure 4-1G, H). Some tumor vessels did not exhibit permanent structural alterations and instead temporarily lost functionality (example vessel highlighted in Figure 4-1I, J). As a result of the structural breakdown, the oxygenation in the tumor vasculature plummeted rapidly up to 6 h after treatment. From 8-48 h post-treatment, a rapid structural and functional recovery ensued, progressing from the tumor periphery towards the tumor core. The vessels which had temporarily lost functionality without losing their structure were gradually reoxygenated (Figure 4-1I, J-O, P). The collapsed tumor vessels re-emerged and reperfused (Figure 4-1M, N-O, P) whereas the vessels in which the structure was completely disintegrated did not recover (Figure 4-1M, O). Rapid neovascularization and vascular remodeling was observed between 24-48 h after OXi4503 administration in the form of new vessel sprouts and new network interconnections. Figure 4-2 gives a magnified view of the vessel remodeling and neovascularization in the tumor periphery during the recovery phase from 8-48 h after a treatment.

Regional quantification of the vessel hemoglobin saturation was performed by dividing the 2-D image vasculature into tumor core, tumor periphery, or normal tissue regions. For example, the tumor nodule is indicated enclosed by the dotted line in Figure 4-1A. Vessels outside the dotted line were considered as normal tissue vasculature. The tumor periphery vessels consisted of the vessels in the 250-500 μm

thin border on the circumference of the tumor nodule. The remaining tumor vessels constituted the tumor core vasculature.

Figure 4-3A shows the tumor before and after each of the serial treatments. An increasing fraction of vasculature-deprived and apparently necrotic tumor area was observed with every serial treatment. In Figure 4-3B is a cumulative plot for three serial treatments in five mice showing the HbSat changes over time. Two individual treatments from two different mice have been omitted from the data in Figure 4-3B owing to lack of considerable oxygenation changes. As seen in Figure 4-3B, the core vessels experienced the greatest impact of the treatment followed by the periphery and the normal vessels. Interestingly, the adjacent normal vasculature also experienced oxygenation changes even though it remained structurally intact throughout the treatment. From 2-6 h there was a steep decrease in all three region vessels with an onset of steady recovery from 8 h onward. The normal and tumor periphery vessels seemed to have an earlier and almost complete recovery back to the original oxygenation values, as opposed to the tumor core vessel oxygenation. At 24 and 48 h post-treatment normal and tumor periphery regions were highly oxygenated but the tumor core did not recover as much and remained relatively less oxygenated. Interestingly, in one mouse the first of the three serial treatments was unable to elicit noticeable structural alterations with only subtle oxygenation changes, while in another mouse the second of the three serial treatments failed to produce any observable morphological or functional changes. Moreover, the later treatments in both these mice were able to produce profuse vascular damage with vivid changes in oxygenation.

No microvessel structural or functional changes were observed in the control mice administered carrier-only treatment. In controls the tumor mass and vasculature continued to develop unrestrained. Over the entire experimental period, the tumor core region gradually becomes less oxygenated compared to the tumor periphery and normal tissue regions as the tumor expands. Figure 4-3C shows the hemoglobin saturation quantification results for carrier-only treatments in 3 mice.

Treatment of Caki-1 Human Renal Carcinomas

An example OXi4503-treated Caki-1 tumor is shown in Figure 4-4. A pattern of structural and functional changes including vascular collapse, vessel disintegration, and oxygenation changes after OXi4503 treatment were observed. Notably, compared to 4T1 tumors the Caki-1 tumors manifested more vessel collapse and lesser vascular disintegration. Among the total number of treatments (n=18), only one single treatment in one mouse showed a comparable amount of tumor vessel disintegration to 4T1 tumors. For the rest of the treatments, as shown in Figure 4-4E, F-I, J, the tumor vasculature underwent a temporary vessel collapse from 2-4 h with minimal structural breakdown. The Caki-1 tumor vasculature recovered earlier with the tumor periphery gradually rejuvenated by 6 h post-treatment (Figure 4-4I, J). During the recovery period from 6-48 h post-treatment, the collapsed vessels reappeared. Similar to 4T1 tumors, some Caki-1 tumor vessels remained intact but experienced dramatic oxygenation changes. Even though there was minimal permanent vessel damage in Caki-1 tumors as compared to 4T1 tumors, there were explicit changes in vessel hemoglobin saturations in tumor and normal vasculature as seen in Figures 4-4 and 4-5. The brightfield images before and after each of the serial treatments is shown in Figure 4-5A and the cumulative quantified vessel oxygenation during each of the serial treatments in

five mice is shown in Figure 4-5B. From Figure 4-5B it can be seen that the tumor core in this tumor type did not have a decrease in microvessel oxygenation during the disruption phase as large in magnitude compared to 4T1 tumors. The core vessel oxygenation was tightly coordinated with the tumor periphery and normal vessel oxygenation, and recovered as much and as fast as the latter two. From the brightfield images in Figure 4-5A it can be seen that compared to 4T1 tumors (Figure 4-3A) there was minimal vessel disintegration and no obvious avascular regions. The control mice which received the carrier-only treatment did not show any dramatic structural and functional changes as shown in Figure 4-5C. With the increasing tumor mass, there was a gradient in the tumor vessel oxygenation from normal surroundings towards tumor core, with core vessels being the least oxygenated.

Even though there was no apparent necrosis evident in Caki-1 tumors, the tumor size seemed to be controlled by OXi4503 treatment. Tumor size in terms of apparent tumor area was measured from the 2-D brightfield images using ImageJ software (ImageJ 1.37a, Wayne Rasband, NIH, USA) and statistical size comparison between control and OXi4503-treated tumors was performed. On average the untreated tumors were significantly larger at 48 h (4.91 mm², $p < 0.03$, two-tailed t-test: paired two sample for means) than the starting tumor size for the first sham treatment (3.44 mm²), and twice the starting size after a fourth sham treatment (7.23 mm²). In contrast, the OXi4503 treated tumors did not show any statistically significant increase from their original size at the start of treatment ($p > 0.36$, two-tailed t-test: paired two sample for means).

Rapid Oxygenation Changes after OXi4503 Treatment

A mouse with a 4T1 tumor was imaged at 30-sec intervals for 20 min prior to drug administration and 60 min after drug administration for real-time recording of the immediate microvascular effects of the drug. In this particular example (Figure 4-6) significant effects began at about 21 min after administration. There was a clear reduction in oxygenation of the tumor periphery, core and normal draining venule. Only the feeding artery oxygenation remained relatively unchanged.

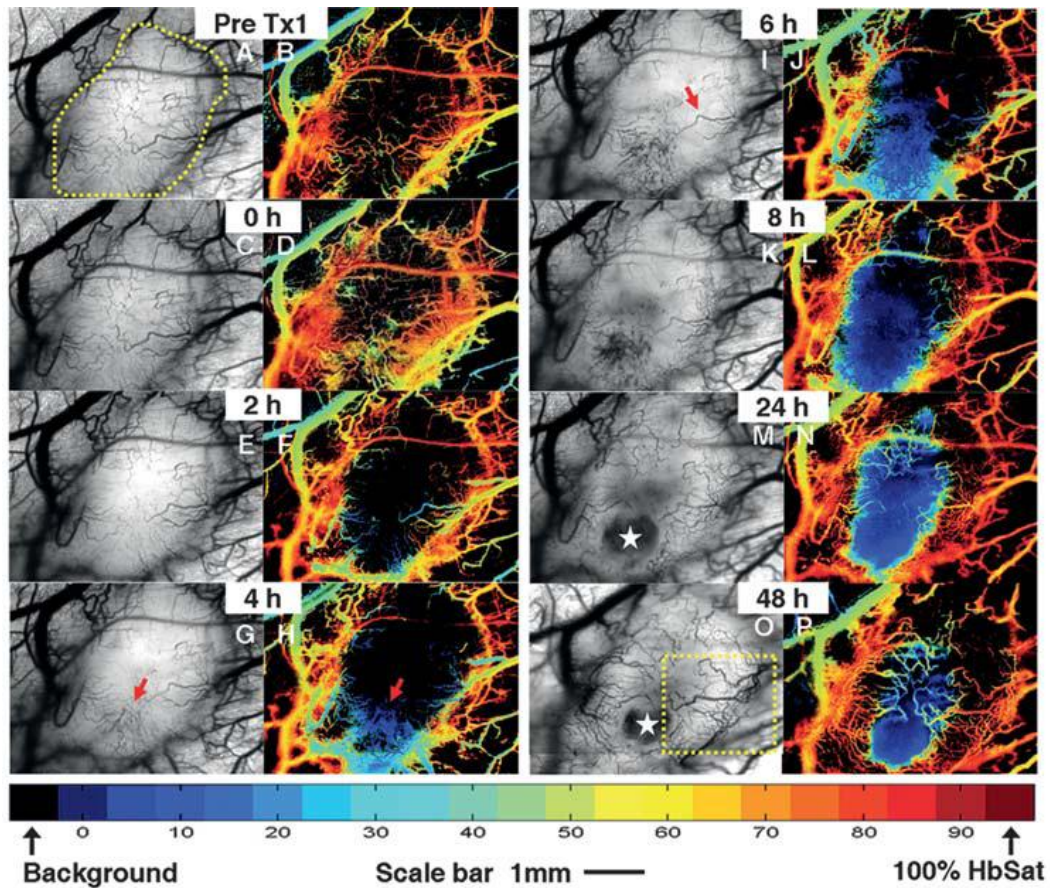


Figure 4-1. Typical OXi4503 treatment progression in a 4T1 tumor-bearing mouse. The brightfield images (left hand figures in each panel) show structural alterations in the vasculature through the course of the single treatment. The approximate tumor border is indicated by the dotted line in (A). Vessels outside the dotted line are considered normal tissue vasculature. The tumor periphery consisted of a 250- to 500- μ m thin border on the circumference of the tumor. Remaining tumor vasculature except for the periphery constituted the tumor core. Images were obtained at x2.5 magnification with image dimensions of 4.15x3.125 mm. The HbSat maps are shown in the right hand figures in each panel. The oxygenation levels in the HbSat maps are color coded as indicated by the colorbar. Arrows in frames (G) and (H) highlight the disintegrating vasculature, while arrows in (I) and (J) indicate an example vessel that persists through all time-points with only oxygenation changes. The star in frames (M) and (O) indicate the avascular regions created by the OXi4503 treatment.

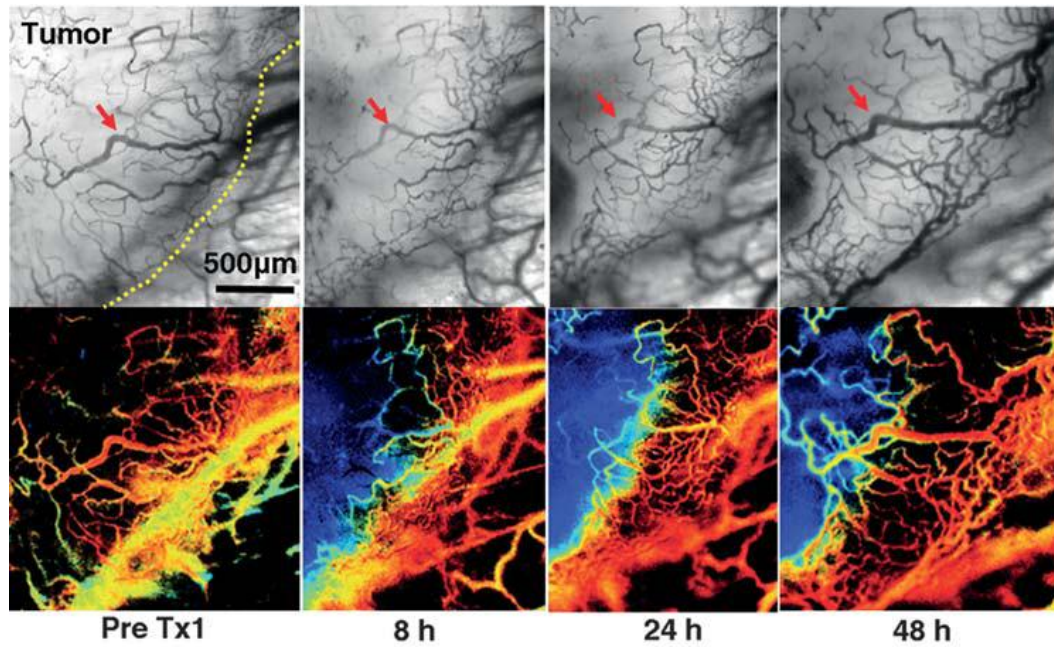


Figure 4-2. Recovery, re-oxygenation, vascular remodeling, and neovascularization in the 4T1 tumor during the recovery phase after OXi4503 treatment for the area indicated in Figure 1O by the dotted rectangle. The approximate tumor border is demarcated by the dotted line in the first bright field image. The arrows highlight an example vessel that maintains its structure throughout the treatment but undergoes dramatic oxygenation changes. The color-scale for hemoglobin saturation is the same as in Figure 4-1.

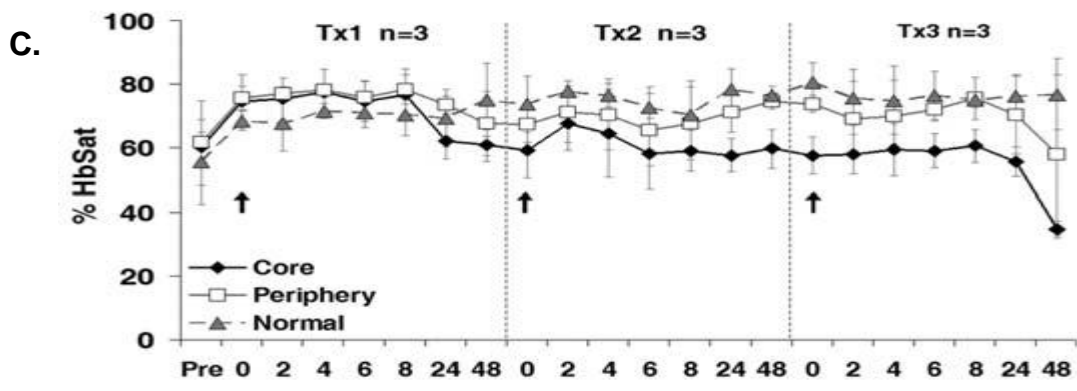
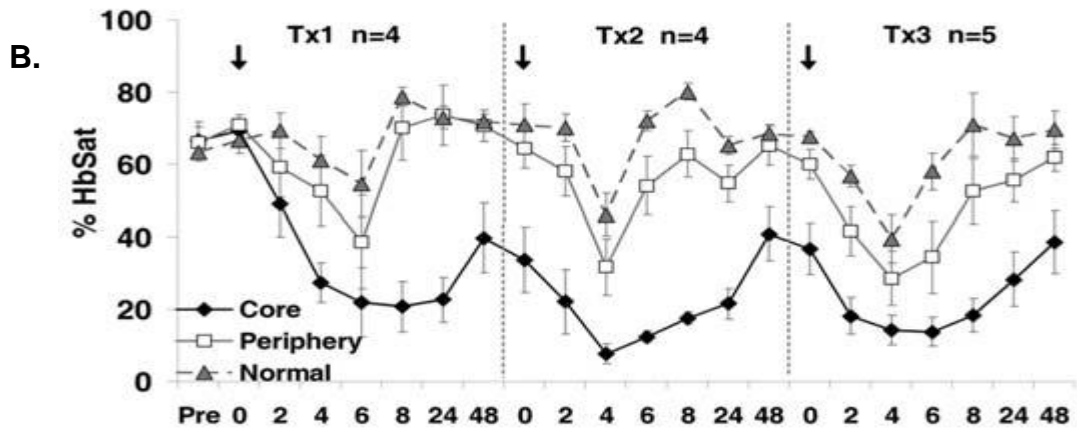
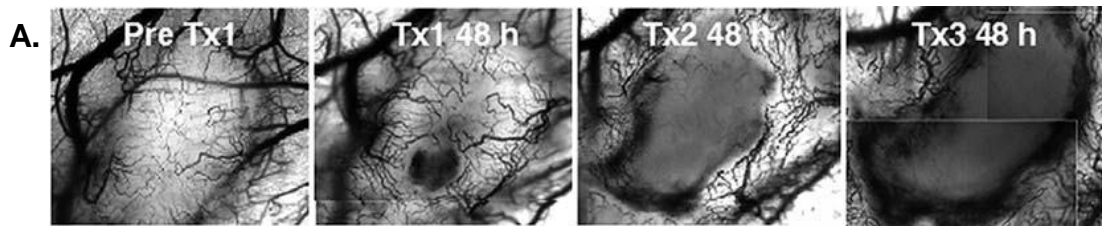


Figure 4-3. Quantitative tumor regional analysis for 4T1 tumor treatment. The tumor was divided into core, periphery, and normal tissue for purposes of analysis. (A) Brightfield images before and after every successive treatment of the tumor in Figure 4-1. (B) Cumulative HbSat values (mean \pm standard error) for 3 serial treatments in all 5 4T1 tumor mice. Arrows indicate drug administration. (C) Cumulative HbSat values (mean \pm standard error) for 3 serial sham treatments (saline) in all 3 control mice.

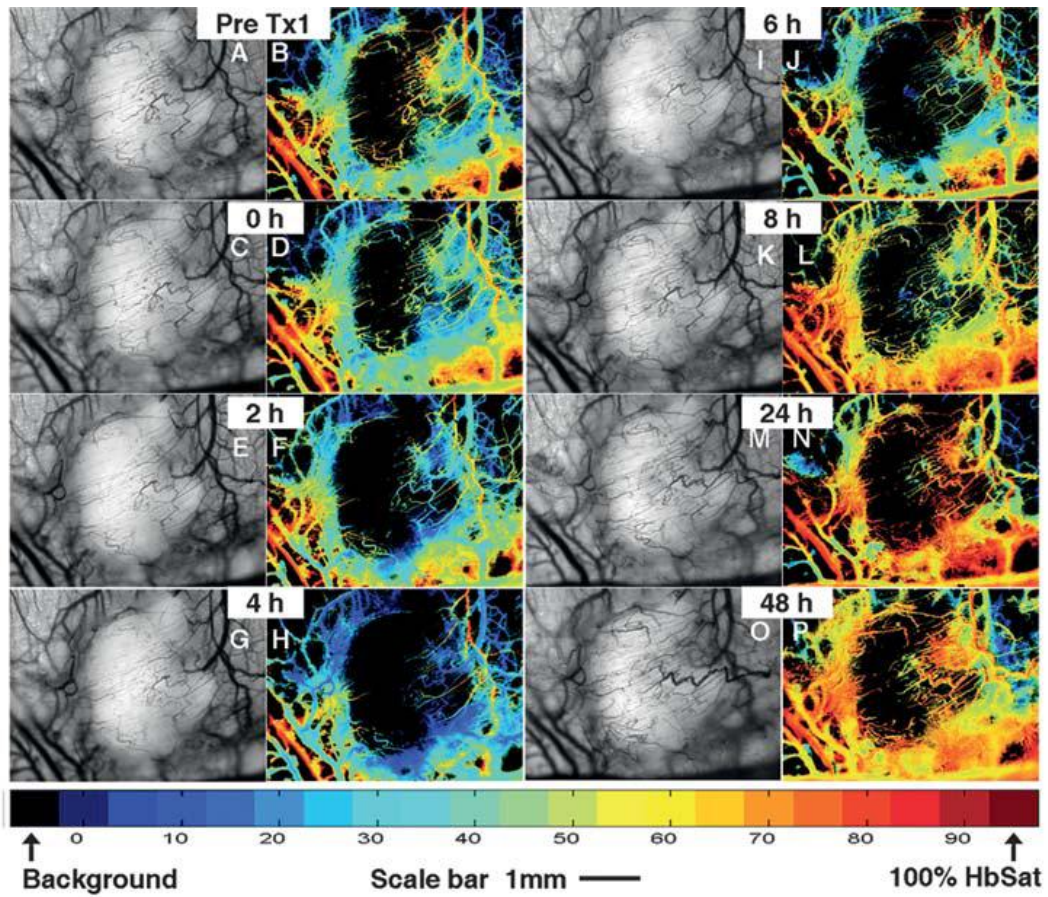


Figure 4-4. OXi4503 treatment 2 of a Caki-1 tumor bearing mouse. Images were obtained at x2.5 magnification with image dimensions of 4.15x3.125 mm. The HbSat maps are shown in the right hand figures in each panel. The oxygenation levels in the HbSat maps are color coded as indicated by the colorbar.

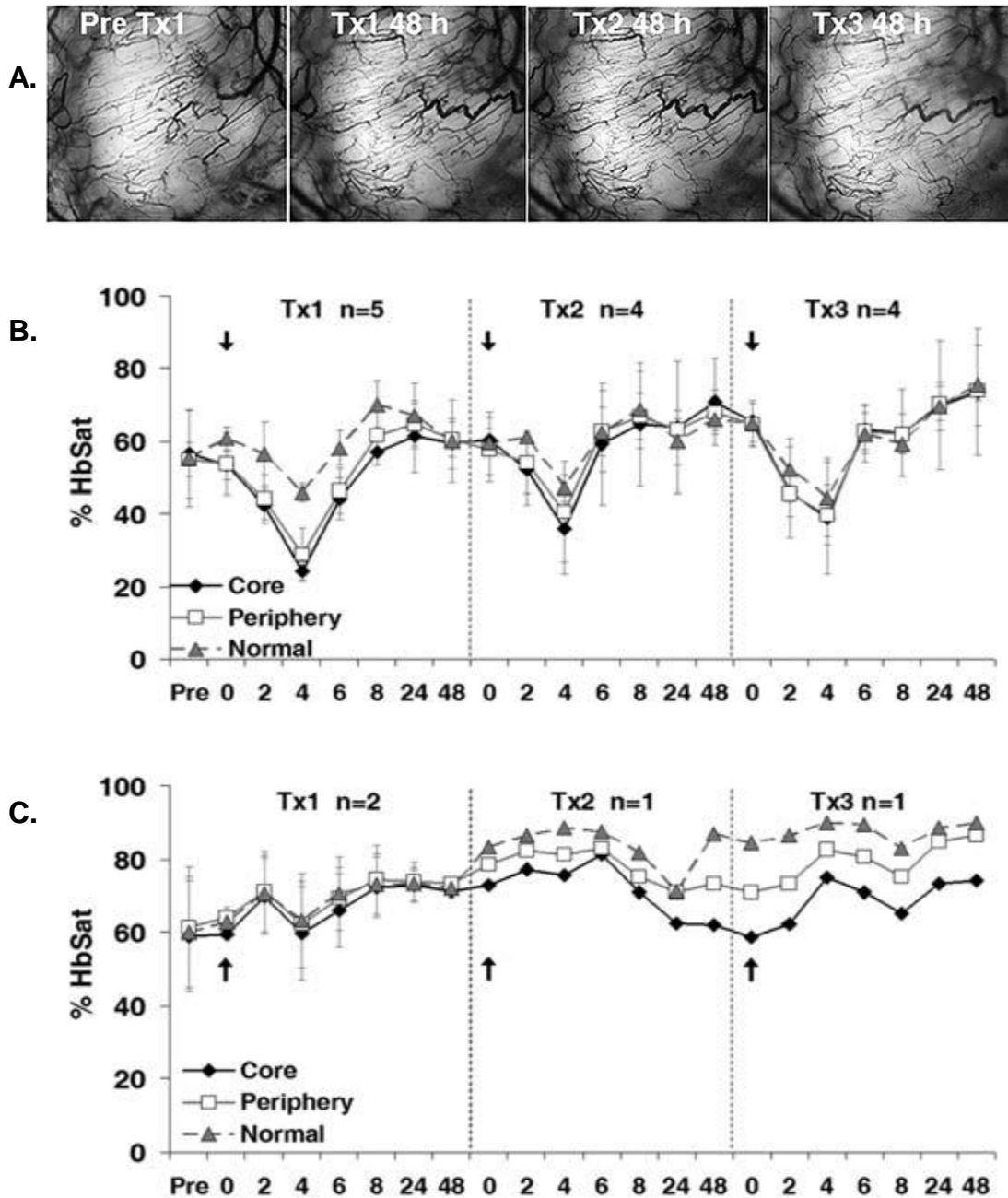


Figure 4-5. Quantitative tumor regional analysis for Caki-1 tumor treatment. The tumor was divided into core, periphery, and normal tissue for purposes of analysis. (A) Brightfield images before and after every successive treatment of the tumor in Figure 6-4. (B) Cumulative HbSat values (mean \pm standard error) for 3 serial treatments in all 5 4T1 tumor mice. Arrows indicate drug administration. (C) Cumulative HbSat values (mean \pm standard error) for 3 serial sham treatments (saline) in a control mouse.

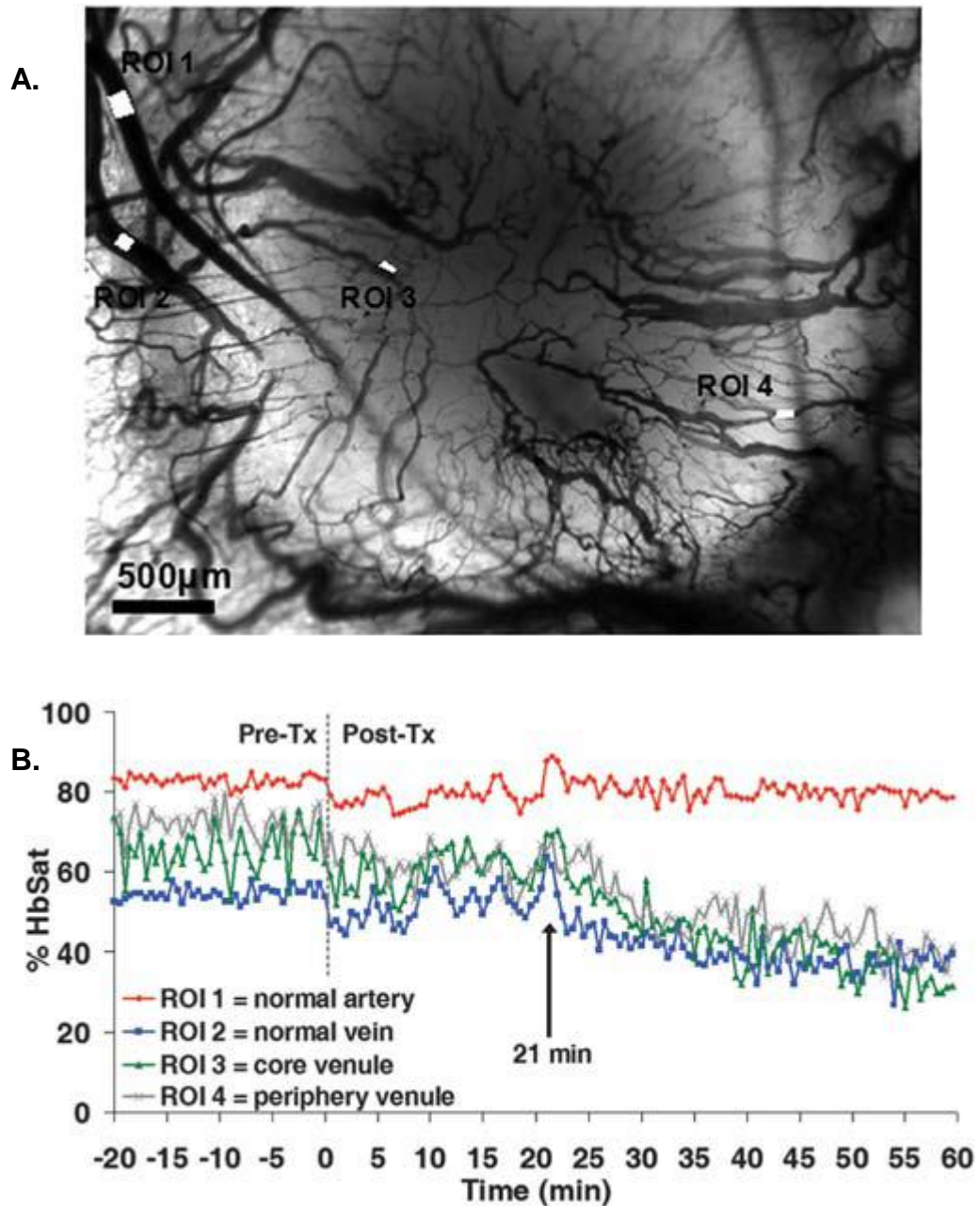


Figure 4-6. Rapid oxygenation changes in 4T1 tumor microvasculature after treatment with VDA OXi4503. The mouse was imaged for 20 min before treatment and for 60 min after treatment. Spectral images were obtained every 30 sec. (A) Brightfield image of the tumor microvasculature. (B) Hemoglobin saturation before and after OXi4503 treatment.

Discussion

OXi4503, a Combretastatin family member, is a tubulin binding drug [161, 162] and currently considered among the most potent VDAs [27, 163]. In this study, we employed spectral imaging of window chamber tumors to investigate the realtime VDA-induced modulation in microvessel structure and function of two different tumor types during multiple serial treatments with OXi4503. Many of the observations with our imaging system were consistent with those reported by others using different techniques. For example, both 4T1 and Caki-1 tumors experienced a rapid drop in vascular oxygenation followed by recovery over 48 h post-treatment. The timings of our observations for vascular disruption and recovery are similar to those reported by Salmon and Siemann using Hoechst-33342 vessel staining for studying vascular shutdown and dynamic contrast-enhanced magnetic resonance imaging for quantifying tumor perfusion inhibition [29]. Both these methods suggested 80-90% tumor perfusion reduction at 4 h, with onset of recovery from 24-48 h (~63% recovery at 48 h). In our study the Caki-1 tumor recovery started earlier than 4T1 tumor recovery beginning at about 6 h post-treatment while 4T1 recovery started around 8 h post-treatment. In previous studies using tumor histology to assess VDA effects, there were indirect indications of vessel hemorrhaging due to the presence of red blood cells in the tissue [164]. With our system, direct real-time visualization of vessel hemorrhaging was possible and confirmed by hemoglobin saturation measurements that showed the presence of deoxygenated extravasated red blood cells. We observed rapid onset of microvessel functional changes in the form of decreasing hemoglobin saturation occurring mostly in tumor capillaries and draining venules starting about 21 min after administration of OXi4503, consistent with reported times for other VDAs [165].

Real-time functional imaging of serial OXi4503 treatments highlighted unexpected differences in the responses of the 4T1 and Caki-1 tumors. The Caki-1 tumors were less responsive to vascular damage induced by OXi4503 than 4T1 tumors. The major Caki-1 tumor response was temporary vessel collapse with minimal vascular disruption followed by reperfusion and reoxygenation at later time-points during recovery. Only a small fraction of the tumor core vessels did not recover. This response was very reproducible with multiple serial treatments. In 4T1 tumors there was extensive permanent microvessel damage and more vessel damage occurred with each subsequent treatment. Consistent with the greater vascular breakdown in 4T1 tumors, there was greater deoxygenation in 4T1 core vessels than in Caki-1 tumors. Despite the fact that in the Caki-1 tumors there was more temporary vessel collapse than permanent vessel disruption, treatment with OXi4503 seemed to control tumor growth similar to 4T1 tumors. It should be noted that while there was little permanent microvessel disruption and a lack of apparent necrosis in the Caki-1 tumors after OXi4503 administration, the treatments were highly dynamic and perturbative in terms of the acute effects on microvessel oxygenation.

Another difference in the tumor treatment response was the lack of apparent necrotic areas in the Caki-1 tumors even after repeat doses, while similarly sized 4T1 tumors developed what appeared to be extensive necrotic areas in the tumor core. The observed induction of necrosis in the 4T1 tumors was unexpected given previous research that showed size dependence in tumor response to VDA treatment. Siemann and Rojani, using several different rodent and human tumor xenografts including Caki-1 tumors in mice, showed that larger tumors (>1 g) had significantly larger areas of

necrosis on the order of 90% after treatment with ZD6126 than smaller tumors (<0.3 g, ~25% necrosis) treated with the same dose [166]. The window chamber tumors fall into the smaller tumor size category, so the lack of apparent necrotic areas in the Caki-1 tumors in this study is consistent with the previous results with ZD6126, but the response of the 4T1 tumors was unexpected at this tumor size. It has been reported that different tumors can have diverse responses to the same VDA treatment owing to inherent variations in their tumor microenvironments or vasculature. For example, upon administration of a single dose of CA4-P to breast adenocarcinoma CaNT tumors and the round cell sarcoma SaS, Parkins *et al* observed greater vascular damage in the tumors having higher nitric oxide synthase activity [167]. While the functional vascular volume, assessed using a fluorescent carbocyanine dye, was significantly reduced at 18 h after CA4-P treatment in both tumor types, the degree of reduction was very different in the two tumors. Similarly, Skliarenko *et al* have reported that the KHT-C murine fibrosarcoma cell line and the CaSki human cervical carcinoma cell line responded differently to the same one time treatment with ZD6126 depending on their initial interstitial fluid pressures (IFP) [168]. Notably, the two tumor types manifested IFP changes distinct from each other, and the tumors with higher IFPs had less tumor cell death. A single tumor can also have different responses to different VDAs. Dalal and Burchill treated TC-32 and A673 Ewing's sarcoma family of tumors with CA4-P, OXi4503, and OXi8007, and demonstrated that different VDAs can have varying efficacy and treatment results in a particular tumor type [169]. In light of the previous results, it is not unreasonable that 4T1 and Caki-1 tumors could vary in their response to OXi4503, and that the differential response with tumor size reported with ZD6126

could be somewhat dissimilar with OXi4503. Further research is required to identify the conditions and mechanisms responsible for the differences in 4T1 and Caki-1 small tumor responses to OXi4503.

In summary, we used spectral imaging of tumor microvessel hemoglobin saturation with mouse window chamber tumors to measure the real-time response of 4T1 and Caki-1 tumors to repeat treatments with OXi4503. Some of the observations made with our imaging system were consistent with others in the literature obtained with different techniques, such as the timing of the onset of vascular changes induced after administration of the VDA. We also observed differences in the responses of the 4T1 and Caki-1 tumors. Specifically, the 4T1 tumors were more responsive to treatment with OXi4503 than Caki-1 tumors in terms of permanent vascular damage and induction of tumor necrosis, a finding that contrasted with previous work using a different VDA. A better understanding of the mechanisms of action of VDAs and how they can vary across tumors or at different stages of tumor development may help optimize the application of these agents and improve their efficacy.

CHAPTER 5 OXI4503 AND AVASTIN COMBINATION TREATMENT OF CAKI-1 TUMORS

Introduction

All tumors need to develop their own vasculature to grow beyond a size of approximately 1 mm³ [170]. Vasculature development by tumors require numerous triggering mechanisms such hypoxia and autocrine growth factor loops among others. Hypoxia or oxygen deprivation is known to accelerate angiogenesis in tumors which in turn up-regulates the vascular endothelial growth factor (VEGF). Increase in VEGF secretion results in angiogenesis which is an inherent characteristic of solid tumors. Although, other factors such as angiopoietins, platelet-derived growth factor B (PDGF-B) etc [34] contribute to angiogenesis, VEGF is the rate-limiting step in normal and pathological blood vessel growth [35]. Hence, inhibiting VEGF function is an attractive strategy in retarding tumor growth.

Based on evidence of its angiogenesis-inhibition potential via VEGF-blocking, recently a drug called Avastin or Bevacizumab has been approved for clinical use. Avastin is the humanized form of the mouse anti-VEGF monoclonal antibody A.4.6.1 that has been utilized widely in research for studying different tumor models. It functions by binding and neutralizing all human VEGF-A isoforms [35, 45].

Although angiogenesis inhibiting agents including Avastin by itself more often than not are found lacking to be a curative as a single therapeutic agent [3, 15]. The complex mechanism of angiogenesis has many triggers, and tumor growth and metastasis being dependent on angiogenesis, the merit of AIs mostly lies in disease control as opposed to tumor cell kill [23, 55]. Furthermore, evidence suggests that cytotoxic therapies

including radiation therapy can initiate tumor angiogenesis [56]. Hence the need for combination of AIs with conventional treatments such as radiation is justified.

In addition, despite their efficacy in terms of vascular damage and tumor cell kill, VDAs alone cannot completely block the nutrient and oxygen supply to the tumor, since, the vasculature along the periphery of the tumor is left intact. Hence, combination of VDAs with other therapies is a logical step in order to achieve complete tumor therapy.

It is well known and has been well characterized that the VDAs such as Oxi4503 utilize their tubulin-binding capability to impart a strong antivasular and antitumor effect. In fact, the effect of Oxi4503 when tested with the models of murine breast adenocarcinoma CaNT , the murine colon tumor MAC29, the human adenocarcinoma MDA-MB-231 and the murine myocardial endothelioma MHEC5-T, Oxi4503 exhibits a stronger antivasular and antitumor effect than CA4P[27]. Notably, Oxi4503 has been shown to retard tumor growth in a dose-dependent manner and improved survival in murine model of colorectal liver metastases[28]. Furthermore, Oxi4503 works by binding the α -tubulin subunits thus preventing the formation of microtubules, which in turn leads to rounding up of endothelial cells. This rounding up of cells ultimately leads to the collapse of vascular wall and formation of thrombus which blocks the blood supply to the tumor [3, 29].

However, Oxi4503 treatment in itself does not lead to complete destruction of the tumor tissue. Hence, a combination of growth retardation of vasculature around the tumor via AIs such as Avastin and disruption of existing vasculature via VDAs such as Oxi4503 forms an attractive complimentary and combinatorial strategy for amelioration of solid tumors and warrants further investigation.

Furthermore, it is imperative to understand the microvessel oxygenation to evaluate the tumor response to different regimes of Oxi4503 and Avastin drug treatment not only because they induce oxygenation fluctuations, but also due to the relevance of tumor oxygen status for other therapeutic modalities. Spectral imaging provides direct information regarding microvessel oxygenation in terms of HbSat. Previously tumor oxygenation has been measured for characterization of AI drug treatment response using various techniques including Eppendorf polarographic oxygen electrodes [60-62], various hypoxia markers [63-65], or radiation response assays [66-68]. Moreover, VDA treatment evaluation also involves tumor microvessel assessment for structure as well as functional changes such as vessel perfusion, permeability, blood flow etc [28, 29, 63-71]. Spectral imaging used with the window chamber model allows visualization of the tumor in a live animal over a period of time. The tumor microvessel oxygenation information in terms of blood hemoglobin saturation along with vessel network structure changes can be studied serially with great temporal and spatial resolution. Such information is an asset when studying the effect of VTAs on tumors. Hence, this method was utilized for studying the combinatorial approach on the tumor pathology.

Specifically, we studied the effect of individual as well as combinatorial treatment of human renal carcinomas (Caki-1 tumors) with two different VTAs (OXi4503, a tubular binding vascular disrupting agent; and Avastin, an anti-VEGF angiogenesis inhibitor) using our mouse window chamber model and spectral imaging system. The eventual goal of this research is the in-depth characterization and optimal combinatorial scheduling of VTAs with conventional therapies.

Materials and Methods

Tumor Cells

Caki-1 human-derived renal carcinoma xenografts were used for the experiments described in this chapter. Caki-1 tumor xenografts [29] were initiated in a single hind limb of donor mice by inoculating with 2×10^5 to 5×10^5 tumor cells. Tumors were excised when they reached about 200 mm^3 in size, and a single cell suspension was prepared in saline. About 1×10^6 cells were used to initiate a window chamber tumor in the experimental mice.

Animal Model

Details about the mouse model have been discussed in previous chapters. All in vivo procedures were conducted in accordance with a protocol approved by University of Florida Institutional Animal Care and Use Committee. Athymic (nu/nu) female mice weighing at least 21 g (Charles River Laboratories, Raleigh, NC) were surgically implanted with a titanium window chamber on the dorsal skin flap. During surgery mice were anesthetized by an IP injection of ketamine (100 mg/kg) and xylazine (10 mg/kg). A tumor was initiated in the window chamber during surgery by injecting the tumor cells (10^6 cells in 10-20 μl saline) subcutaneously in the dorsal skin flap prior to placing a 12-mm diameter no. 2 round glass coverslip (Erie Scientific, Portsmouth, NH) over the exposed skin. After surgery animals were housed in an environmental chamber maintained at 33°C and 50% humidity with free access to food and water and standard 12-h light/dark cycles.

Drug Preparation and Experimental Design

Vascular disrupting agent OXi4503

OXi4503, a gift from OXiGENE, Inc. (Waltham, MA) was administered at a dose of 10 mg/kg IP (0.01 ml/g of mouse body weight). The light-sensitive drug was protected from light during handling. OXi4503 was suspended in a solution of sterile saline and 50 µl per ml of 5% sodium carbonate solution before injection. The drug was prepared fresh daily. Control groups received an equivalent volume of sterile saline and 5% sodium carbonate solution.

Angiogenesis inhibitor Avastin

Avastin was received from Siemann lab. The stock solution was stored in 4°C and diluted to a dose concentration of 2 mg/Kg (0.01 ml/g of mouse body weight). Controls received equivalent amount of saline.

Individual and combinatorial treatment design and imaging schedule

The Caki-1 tumors were allowed to grow for 8-12 days before starting the treatment. For individual treatment with OXi4503, the treatment was repeated every 48 hours for up to 3 times per mouse (Given on e.g. MWF of the week). Spectral imaging was performed immediately prior to the treatment, and also at 4, 8, 24 and 48 h post-treatment. After the 48-h imaging time point the mouse was re-treated and the same imaging schedule was maintained. In all, 12 mice bearing Caki-1 tumors were treated with OXi4503 and 3 mice were carrier only controls.

For individual treatment with Avastin, the treatment was given twice each week (Given on e.g. M and F of the week). Mice that received combination treatment, Avastin was always injected 1 hour post OXi4503 administration. Imaging time points were

maintained same as the OXi4503 schedule for all individual, combination, and control treatments.

In all, 12 mice received OXi4503 only. Combination treatment was given to 5 mice. Three mice received Avastin only, whereas 3 mice were controls receiving carrier only (saline or saline and 5% sodium carbonate solution).

Tumor Size Measurement

Tumors were measured with calipers everyday of imaging and tumor volume was calculated assuming that the tumor volume as a half of an ellipsoid. The following equation was used to calculate tumor volume in mm³:

$$Tumor\ volume = \frac{1}{2} \left[\frac{\pi}{6} \times major \times minor \times vertical \right]$$

Where, major, minor and vertical represent the three mutually perpendicular axes of the ellipsoid.

Imaging System, Image Acquisition and Image Processing

The spectral imaging system, image acquisition, and image processing methods for hemoglobin saturation measurements were discussed in detail previously [125]. Briefly, a Zeiss Axiolmager microscope (Carl Zeiss, Inc., Thornwood, NY) was used as a basic platform for the imaging system. For transillumination images, a 100-W tungsten halogen lamp was used. The long working distance objectives used were 2.5× and 5× Fluars, 10× EC Plan-NeoFluar and 20× LD-Plan-NeoFluar (Carl Zeiss, Inc.). For spectral information, brightfield transmitted light images were obtained using a CCD camera thermoelectrically cooled to -20°C (DVC Co., Austin, TX; Model no.1412AM-T2-FW). Band-limited optical filtering was accomplished using a C-mounted liquid crystal tunable filter (CRI, Inc., Woburn, MA) with a 400- to 720-nm transmission range and a

10-nm nominal bandwidth, placed in front of the CCD camera. LabVIEW8 (National Instruments Corp., Austin, TX) was used to automatically control the tuning of the LCTF and acquire images with the CCD camera. Microvessel hemoglobin saturation measurements and images were created from the spectral image data [90, 129].

Statistical Analysis

The least mean squares values and standard error were obtained using two-way ANOVA via General Linear Model program, SYSTAT 12 (Version 12, Systat Software, San Jose, CA), with independent variables being the time points and treatment number. The significant pairs between different time points were obtained using Tukey's honestly significant difference test. The data obtained from at least 3 different mice was pooled together to perform the statistics.

Results

Tumor Model Identification

Caki-1 tumor growth after individual treatment with OXi4503

From our previous work with OXi4503, we observed that compared to 4T1 mouse mammary carcinomas, Caki-1 human-derived tumors consistently appeared less susceptible to permanent vascular damage in response to the VDA (Figure 4-4 and 5 from Chapter 4). We found out that several studies so far have suggested a link between tumor size and VDA response [25, 166, 171](from proposal). A recent study by Masunaga et al also stressed the importance of tumor size along with time of dosage for optimal response in individual ZD6126 treatment as well as when using it in combination with the cytotoxins tirapazamine (TPZ) and gamma-rays [172]. Siemann et al have specifically shown to tumor size dependence of Caki-1 tumors to another VDA named ZD6126 [166]. This fact, in addition to our observations of profuse vascular damage with

our small-sized 4T1 tumors (~3mm diameter), suggested that larger Caki-1 tumors may be able to induce better response for OXi4503 treatments.

Thus, Caki-1 tumors were grown in different sizes and treated with 1-3 serial treatments every 48 hours with the VDA OXi4503. As a measure of treatment response, tumor volume measurement, HbSat changes, and vascular changes were monitored. Figure 5-1 shows the data from tumor volume comparison after OXi4503 treatments. It was observed that OXi4503-treated tumors up to 50 mm³ volume showed greater tumor size control as compared to controls in our mouse model.

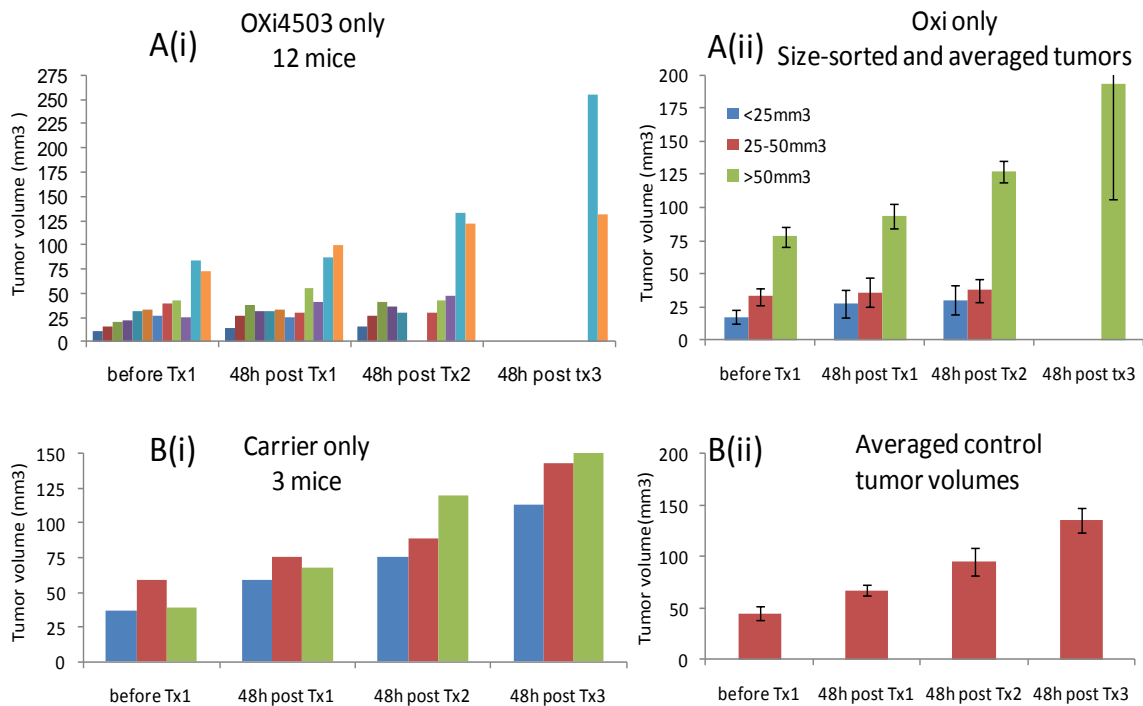


Figure 5-1. Effect of OXi4503 treatment on different sized Caki-1 tumors. As shown in Figure 5-1A (i) and (ii), tumors with pre-OXi4503 volumes up to 50 mm³ demonstrated control of tumor growth compared to controls in the window chamber model.

Effect of OXi4503 treatment on Caki-1 tumors: Hemoglobin saturation (HbSat) assessment

The tumors were serially treated with OXi4503 every 48 hours and HbSat maps of tumors and normal vasculature were obtained. Figure 5-2 demonstrates an example treatment with OXi4503. At the time of treatment the tumor was approximately 55 mm³ in volume and 12 days old. At each imaging time point multiple images of the tumor and adjacent vasculature were obtained and complete tumor image was obtained by collage of several regions.

As evident from the data, there was extensive and gradual structural damage and function loss in the tumor vasculature up to 8 h upon OXi4503 treatment. The vessels appeared to have constricted in diameter at 4 h (Figure 5-3 Brightfield image 4h post-Tx) along with complete cessation of oxygenated blood supply (Figure 5-3 HbSat image 4h post-Tx). The tumor periphery vessels start regaining oxygenated supply from 8 h onward, whereas the regrowth of tumor peripheral vessels appears to have started in the wake of oxygenation recovery. The tumor core lost bulk vascular network which did not recover and led to massive avascular regions in the tumor body likely causing tumor cell death. The evidence of effective treatment was also seen in the form of tumor size reduction at 48 h time point from 55 to approximately 42 mm³ for this particular tumor.

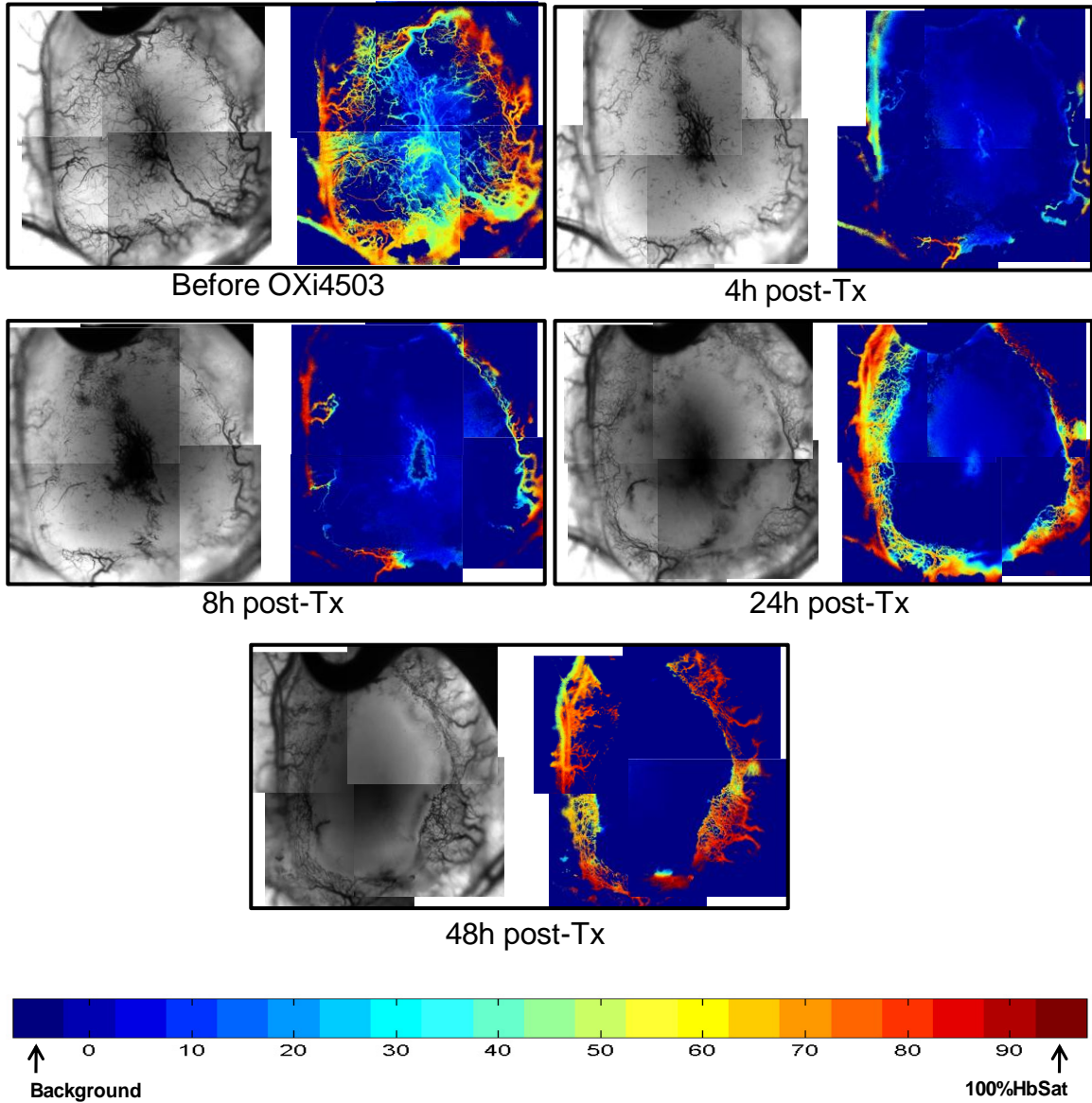


Figure 5-2. Example of one of the serial OXi4503 treatments in one mouse. The brightfield images are shown along with the corresponding hemoglobin saturation maps. At the beginning of treatment the tumor was approximately 55 mm^3 in volume and 12 days old. Structural deterioration of tumor vessel network is evident in the brightfield images up to 8 h post Tx, with recovery of peripheral vessels from 24 h. Oxygenation plummeted corresponding to the structural damage nearly to 8 h and recovered on the tumor rim from 8 h. At 48 h post Tx tumor had shrunk to nearly 42 mm^3 in volume.

Combination Treatment with OXi4503 and Avastin

Tumor growth study

The data in figure 5-3 shows the comparison of tumor volumes after they were subjected to serial treatments with either OXi4503 or Avastin alone, or with a combination of the two. It was observed that even though OXi4503 treatment alone was able to effectively control tumor size (Figure 5-3C), the combination treatment was even more effective in obliterating the tumors (Figure 5-3D) as compared to the individual treatments with either of the VTAs. Although Avastin treatment did slightly slow down the tumor growth as compared to controls in the one week of Avastin treatment (Figure 5-3A and B), its effect was very limited as compared to OXi4503 or combination treatments. Statistically significant pairs are indicated in Figure 5-3E.

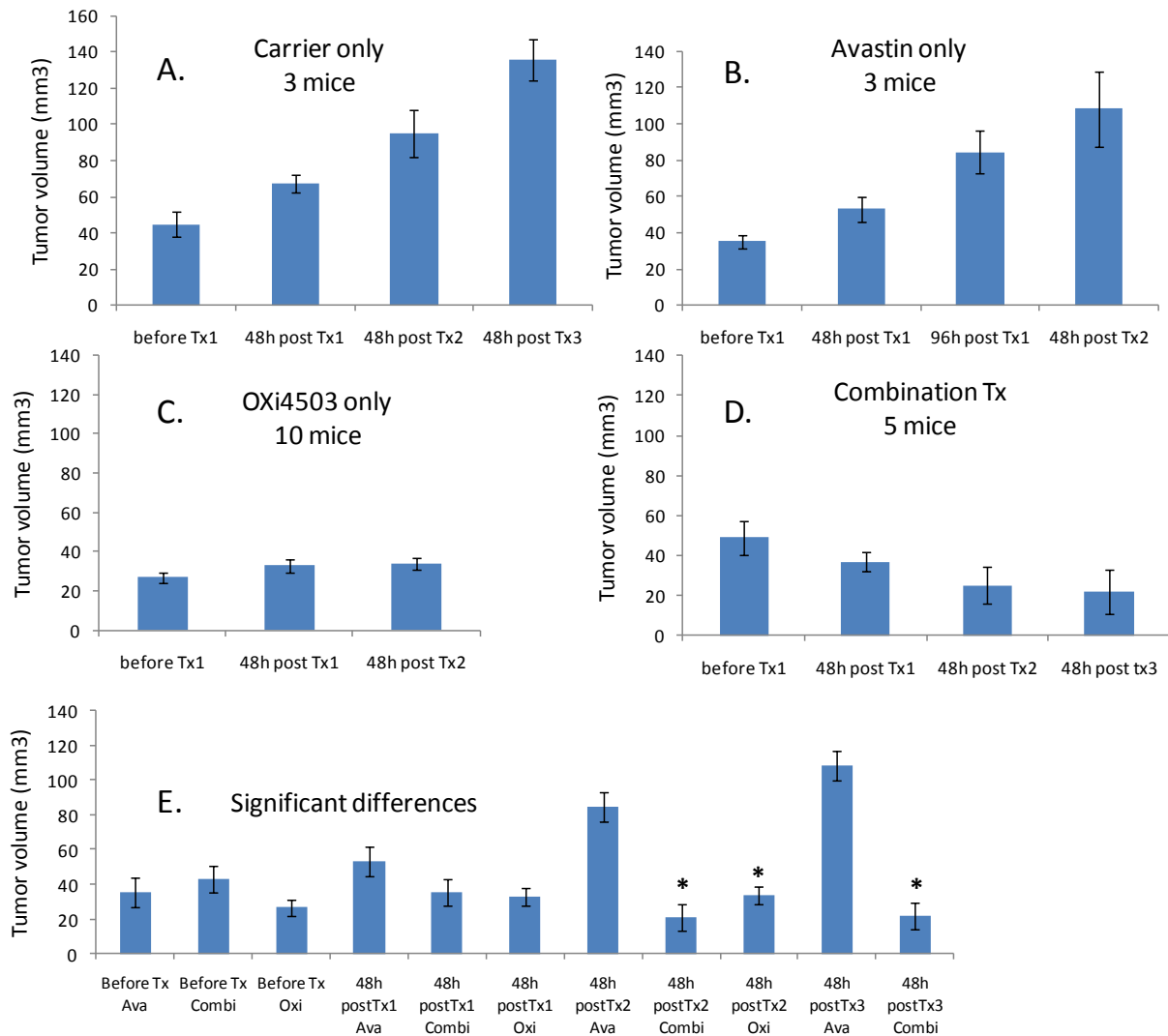


Figure 5-3. Tumor volume comparison after individual and combination treatment with OXi4503 and Avastin. It was observed that combination of therapeutics have additive/supra-additive effects on tumor size reduction of Caki1 tumors. A) The carrier treatment had no effect on tumor growth retardation. B) Avastin alone did not reduce the tumor size appreciably. C) The treatment of OXi4503 alone retarded the tumor growth D) Trend suggests that the combinatorial treatment of Avastin and OXi4503 reduces the tumor size with each consecutive treatment. E) Interesting significantly different pairs ($p < 0.05$) are as follows: treatments marked with * as compared to 48h post Tx2 and Tx3 of Avastin.

Quantitative HbSat analysis and comparison

Oxygenation change is a major characteristic of VDA treatment. All treatments are also reported to have oxygenation changes. Hence we quantified and compared HbSat values for all the VTA treatments. Four different treatment regimens were undertaken to compare the oxygenation of the tumor microvasculature: 1) OXi4503 only treatment, 2) Avastin only treatment, 3) Combination of Avastin and Oxi4503 and 4) Carrier only control treatment.

Quantitative microvessel oxygenation was obtained in terms of blood HbSat using methods previously described. Briefly, oxy- and deoxy-hemoglobin have distinct photo-absorbance spectrum between 500-575 nm. Spectral brightfield information was obtained in the absorbance range of blood hemoglobin and HbSat values were derived using linear least square regression model [89].

For assessment of oxygenation changes in various parts of the tumor, tumor vasculature was classified as belonging to the tumor core, periphery, or the normal

vasculature outside the tumor (Figure 5-4).

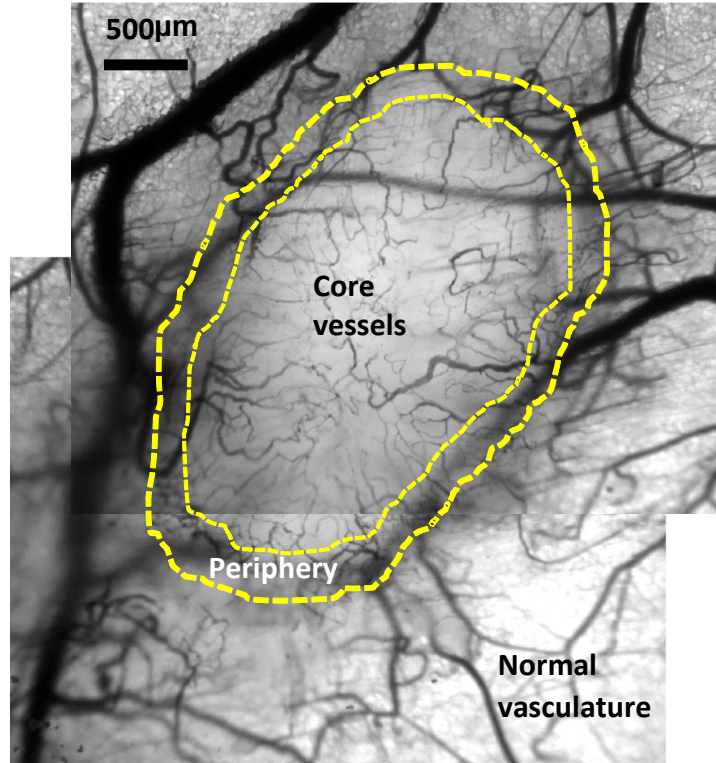


Figure 5-4. Example of classification of tumor core, periphery and normal vasculature. The periphery was chosen between 250-500 µm on the tumor rim.

For analysis, the HbSat values obtained were first normalized with respect to the values obtained for the time point just before (0 h) treating the mice with different conditions. In all, 12 mice were treated with Oxi4503 only treatment, 5 mice were treated with Avastin only treatment, whereas 5 mice were treated with combination treatment of Avastin and Oxi4503 and 3 mice were utilized for control by delivery of carrier only. Hyperspectral images were obtained and HbSat values were quantitatively determined at different time points of 0h, 4h, 8h, 24h, and 48h after each treatment. As many as 3 treatment regimens were provided for each individual treatment type. Data

was pooled and statistics was performed using Systat 12 software to obtain Tukey's-honestly-significant differences between oxygenation levels at different time points. The average values for different time points with standard error are plotted for all the treatment types (Figure 5-5).

Upon treatment of Oxi4503, it was observed that after 4 h, the oxygenation in the periphery, core and normal vessels dipped by 20-50%, which was found to be significantly different from the initial oxygenation levels at 0 h (Figure 5-5 Ai, Aii, Aiii). It is evident from the plots that even though the peripheral and normal vessels underwent significant differences in oxygenation after each treatment, their recovery was faster than the core vessels that were affected more and regained oxygenation slower after each OXi4503 treatment. Notably, in the periphery vasculature for the first and second treatment, 4 h oxygenation level was significantly different with all the other time points for the respective treatments. Furthermore, it was observed that there were significant differences between 4 h and 8 h for both first and second treatment in the normal vasculature. Additionally, there was significant difference between 4 h and 48 h oxygenation levels for the second treatment in the normal vasculature. However, in case of core vessels, 4 h oxygenation levels were statistically different from 0 h and 48 h oxygenation only. (Figure 5-5 Ai, Aii, Aiii).

For Avastin only treatment, in the periphery vasculature the oxygenation level was found to be significantly improved at 72 h post Tx1 as compared to 8 h and 24 h. There were no significant differences found for the core and normal vasculature for this treatment type (Figure 5-5 Bi, Bii, Biii), although an overall incremental trend in the oxygenation was observed after Avastin treatments.

Interestingly, for the combination treatment, significant differences were observed in the second treatment group between oxygenation levels at 4 h and 0 h; and 4 h and 48 h for the periphery vasculature. Contrarily, although, for the core vasculature, significant differences were not observed in the second treatment there were significant differences observed in the first treatment between oxygenation levels of 0 h and 4 h; 0 h and 8h; 4 h and 48 h. Additionally, for the normal vasculature, although, there was significant difference between oxygenation levels at 8 h and 48 h, the change in oxygenation values was > 20% (Figure 5-5 Ci, Cii, Ciii).

As expected, the control of carrier only vasculature did not have any significant differences between oxygenation levels at different time points for periphery, core and normal vasculature (Figure 5-5 D).

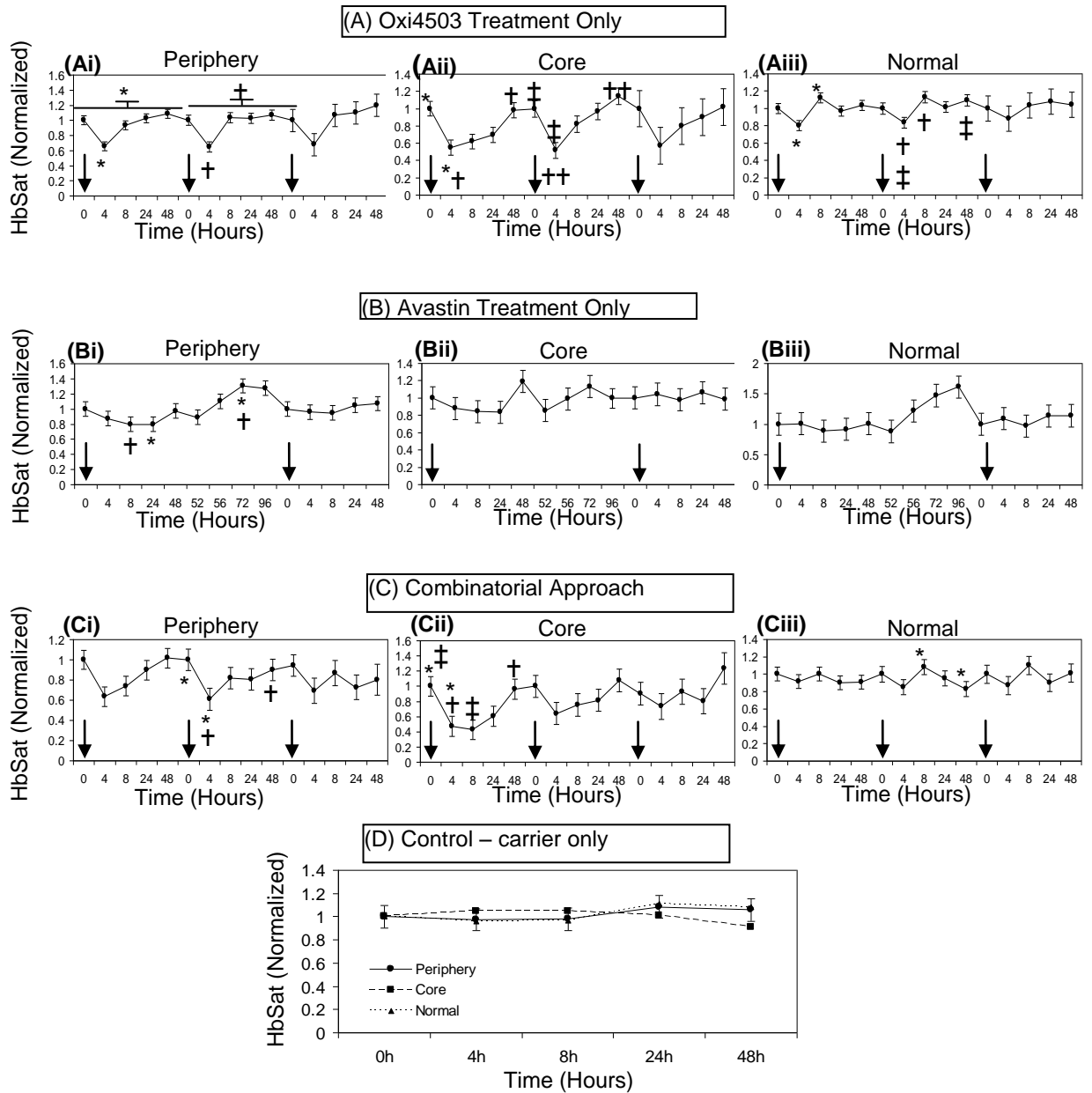


Figure 5-5. The HbSat or oxygenation of the periphery, core and normal microvessels modulates with individual treatments with (A) Oxi4503 or (B) Avastin, or their (C) combination at different time points and (D) control. Two-way ANOVA was performed on HbSat values normalized to 0 h time points of each treatment obtained from more than 3 mice per group and the average values of HbSat and standard error are plotted against corresponding time points. Significant differences between individual time points are indicated. The black arrows represent the time point where treatment was given to mice.

Discussion

Neoplasms need neovasculature to develop beyond a few millimeters in size [170]. Tumors employ several different mechanisms for inducing angiogenesis thereby causing endothelial cell proliferation and sprouting of new microvessels from the existing vasculature [10, 18, 19]. Tumor vasculature makes a lucrative target for drug development owing to the crucial role of endothelial cells in cancer cell survival, growth, and metastasis, and because they are more genetically stable, and potentially less likely to develop resistance to therapeutic agents as compared to tumor cells themselves [19]. Moreover, targeting endothelial cells offers new avenues for therapeutic targeting than traditional chemotherapeutics, thereby implying potential dual benefit from combination approach.

A number of strategies are in development for targeting tumor vasculature. Some approaches focus on inhibiting neo-vasculature sprouting by blocking the angiogenic pathways (Angiogenesis inhibitors, AIs), while others seek to destroy the existing tumor vasculature (Vascular disrupting agents, VDAs) [17]. Combination of these two mechanisms to target tumor vasculature is a new approach being currently investigated. It has been observed that angiogenesis inhibiting agents more often than not are found lacking to be a curative as a single therapeutic agent [3, 15]. The complex mechanism of angiogenesis has many triggers, and tumor growth and metastasis being dependent on angiogenesis, the merit of AIs mostly lies in disease control as opposed to tumor cell kill [23, 55]. In addition, despite their efficacy in terms of vascular damage and tumor cell kill, VDAs alone cannot completely block the nutrient and oxygen supply to the tumor, since, the vasculature along the periphery of the tumor is left intact.

Combination of AIs with VDAs is under investigation and shows promise for comprehensive tumor therapy[24-26]. Due to their complimentary mechanisms of action and non-overlapping treatment schedules, AIs and VDAs may be used together for enhanced tumor treatment as compared to individual treatment with these agents.

Based on this synergistic mechanism hypothesis, using spectral imaging techniques we endeavored to evaluate the efficacy of combination treatment with two of the popular VTAs, OXi4503 and Avastin, in the Caki-1 renal cell carcinomas. Human-derived Caki-1 cells were chosen for the combination study since Avastin is a recombinant humanized monoclonal antibody against vascular endothelial growth factor (VEGF) [45]. Also, renal cell carcinomas have been reported to have particularly high VEGF expressions potentially making them particularly susceptible to Avastin.

OXi4503, the diphosphate prodrug of CA1P [173], is a tubulin binding agent currently regarded as one of the most potent VDAs [27, 163]. It is a fast acting drug, shown to induce time-dependent decrease in tumor perfusion, increase in tumor vessel permeability, and profuse tumor vascular damage in several tumor models [3, 27, 28]. The anti-angiogenic Avastin (Bevacizumab) is a recombinant humanized monoclonal antibody against vascular endothelial growth factor (VEGF) [45]. Owing to its significance for the process of angiogenesis, VEGF-inhibition leads to arrest of tumor growth and metastasis [57]. The non-overlapping effects of these two VTAs, have been shown to improve tumor treatment measured in terms of increased growth delay, when used as a combination as opposed to individual treatment [24].

Before using them for VTA combination treatments, preliminary characterization of Caki-1 tumors was performed. From our previous work with OXi4503 [174], we

observed that compared to 4T1 mouse mammary carcinomas (approximately 3-4mm in diameter), the Caki-1 human-derived renal tumors (approximately 2-3mm in diameter) consistently appeared less susceptible to permanent vascular damage in response to the VDA. We found out that several studies so far have suggested a link between tumor size and VDA response [25, 166, 171]. This fact, in addition to our observations of profuse vascular damage with our small-sized 4T1 tumors, indicated that larger Caki-1 tumors may induce better response for OXi4503 treatments. Thus, Caki-1 tumors were grown at larger sizes (approximately 3.5-7.5mm in diameter) in the window chamber mouse model (approximately 1cm in diameter) compared to previous experiments (approximately 2-3mm in diameter), treated serially with OXi4503 up to 3 times, and their response evaluated. Our tumor growth data indicated that tumors less than or around 5mm in diameter (approximately 50 mm³ in volume) demonstrated effective tumor growth retardation in the window chamber model (Figure 5-1). Also, as seen in Figure (5-2), profuse vascular disintegration and oxygenation changes similar to previous observations in 4T1 tumors (Figure 4-1 and 3) further signified the suitability of Caki-1 tumors for studies with the combination treatments.

Once the tumor model to be used for combination studies with OXi4503 and Avastin was identified, Caki-1 tumors were subjected to four different treatment regimens to compare the tumor growth retardation, and changes in structure and oxygenation of the tumor microvasculature: 1) OXi4503 only treatment, 2) Avastin only treatment, 3) Combination of Avastin and Oxi4503 and 4) Carrier only control treatment.

Tumor growth monitoring post-VTA treatments clearly revealed differences between the efficacies of the individual and combination treatments (Figure 5-3).

Compared to the controls, Avastin only treatment marginally retarded the tumor growth rate with one week of treatment (Figure 5-3A and B). This was somewhat expected since anti-angiogenics such as Avastin are considered long-term treatments, believed to cause tumor growth retardation over much longer periods. Although Avastin treatment did retard the tumor growth, its effect was very limited as compared to OXi4503 or combination treatments. Interestingly, even though OXi4503 treatment alone was able to effectively control tumor size (Figure 5-3C), the combination treatment was even more effective in obliterating the tumors (Figure 5-3D) as compared to the individual treatments with either of the VTAs, thus confirming the findings of Siemann et al [24].

Spectral imaging enabled us to obtain microvessel oxygenation values in terms of hemoglobin saturation. As depicted in Figure 5-5, this vessel oxygenation data evaluation and comparison between the various treatment regimens offered further insights into the mechanism of these drugs. The OXi4503 treatment induced consistent vascular structure and corresponding function loss at approximately 4 h after each of the serial treatments. With each serial treatment, the tumor core vessels suffered the most with loss of oxygenation up to nearly 50% of the pre-treatment value, followed by tumor peripheral vessels (approximately 30% oxygenation loss) and adjacent normal vasculature (approximately 20% oxygenation loss) (Figure 5-5Ai, ii, iii). The periphery and normal vessels recovered faster at the 8, 24 and 48 h post-treatment time points, whereas the core recovered much slower owing to the OXi4503-induced vascular network disruption. These results were similar to the results obtained with 4T1 tumors (Figure 4-3).

Changes in tumor vessel oxygenation post-Avastin were subtle compared to OXi4503 treatment. Though not statistically significant, overall incremental trend was observed in the normal, peripheral, and tumor core vasculature after 72 h post first Avastin treatment. Interestingly, for combination treatment the initial treatments appear to induce oxygenation changes similar to individual OXi4503 treatment, with later serial treatments showing lesser fluctuations (Figure 5-5 Ci, Cii, Ciii). This makes us speculate the impact of Avastin on the treatment response. The mechanisms responsible for such influence are still unknown and require further investigation.

In summary, we identified an appropriate tumor model for VTA combination treatment evaluation and used spectral imaging of tumor microvessel hemoglobin saturation with mouse window chamber tumors to measure the real-time response of Caki-1 tumors. Some of the observations made with our imaging system support the literature as well as our previous work. We were able to identify differences in the responses of Caki-1 tumors to individual and combination treatments with OXi4503 and Avastin. A better understanding of the mechanisms of action of VTAs and how they can be used in synergy with each other may help optimize the application of these agents and improve their efficacy.

CHAPTER 6 CONCLUSION AND FUTURE DIRECTION

In conclusion, we were able to utilize spectral imaging methods in live mouse window chambers to study the efficacy of novel tumor therapeutic drugs. We identified an appropriate tumor model for the evaluations of two leading vascular targeting agents namely OXi4503 and Avastin. Our findings clearly suggest that the combination of these two vascular targeting agents induce better therapeutic outcomes in terms of tumor growth retardation as compared to individual treatments with either agent. Additionally, OXi4503 modulates the tumor microvascular response in the presence of Avastin. Interestingly, in the later treatments, there is minimal permanent vessel damage along with frequent vascular collapse of the tumor core vessels. We observe that these vessels recover from their collapsed state with rejuvenated blood supply and ample oxygenation. In the combination therapy, despite minimal vessel disintegration, the tumors experience size reduction indicating necrosis or apoptosis of tumor cells. The mechanisms involved causing these effects are not yet known and warrant further investigations.

The modulation of vascular response upon combination treatment might be explained by the varying VEGF production and VEGF-blocking process that occurs during the combination treatment. Upon use of Avastin as a single agent, reduction in neo-angiogenesis of tumor vessels was observed, however its effect appeared more dramatic when used in combination with the vascular disrupting agent, Oxi4503. In the presence of Avastin, VEGF may have been blocked effectively to mellow down the recovery phase of OXi4503. Additional VEGF expression, along with the pathological tumor cell expression of VEGF, with OXi4503 treatment may have increased the

potency of Avastin. In order to dispel these numerous uncertainties, further studies to assess the functional VEGF activity prior to and after these VTA treatments are required. Again, despite the apparent reduction in the vascular damage, the data suggests that tumor cell death may have been increased leading to the tumor size reduction. Mechanisms responsible for this phenomenon need to be investigated.

A better understanding of the mechanisms of action of VTAs and how they can be used in synergy with each other may help optimize the application of these agents and improve their efficacy.

LIST OF REFERENCES

1. Siemann DW, Chaplin DJ: **An update on the clinical development of drugs to disable tumor vasculature.** *Expert Opin Drug Discov* 2007, **2**(10):1–11.
2. Hirst DG, Flitney FW: **The physiologic importance and therapeutic potential of nitric oxide in the tumour-associated vasculature.** In: *Tumour Angiogenesis*. Edited by Bicknell R, Lewis CE, Ferrara N. Oxford: Oxford University Press; 1997: 153–167.
3. Salmon HW, Siemann DW: **Effect of the second-generation vascular disrupting agent OXi4503 on tumor vascularity.** *Am Assoc Cancer Res* 2006, **12**(13):4090–4094.
4. Bikfalvi A: **Angiogenesis: health and disease.** *Ann Oncol* 2006, **17**(Suppl 10):65–70.
5. Siemann DW: **Vascular targeting agents.** *Horizons in cancer therapeutics* 2002, **3**:4–14.
6. Horsman MR, Siemann DW: **Pathophysiologic effects of vascular-targeting agents and the implications for combination with conventional therapies.** *Cancer Res* 2006, **66**(24):11520–11539.
7. Folkman J, Shing Y: **Angiogenesis.** *J Biol Chem* 1992, **267**(16):10931–10934.
8. Arap W, Pasqualini R, Ruoslahti E: **Cancer treatment by targeted drug delivery to tumor vasculature in a mouse model.** *Science* 1998, **279**:377–380.
9. Ruoslahti E: **Specialization of tumor vasculature.** *Nat Rev Cancer* 2002, **2**:83–90.
10. Ellis LM, Liu W, Ahmad SA, F F, Jung YD, Shaheen RM, Reinmuth N: **Overview of angiogenesis: Biologic implications for antiangiogenic therapy.** *Semin Oncol* 2001, **28**:94–104.
11. Kerbel RS: **Tumor angiogenesis: past, present and the near future.** *Carcinogenesis* 2000, **21**:505–515.
12. Chaplin DJ, Dougherty GJ: **Tumor vasculature as a target for cancer therapy.** *Br J Cancer* 1999, **80**(Suppl 1):57–64.
13. Denekamp J: **The tumor microcirculation as a target in cancer therapy: a clearer perspective.** *Eur J Clin Invest* 1999, **29**:733–736.
14. Baguley BC: **Antivascular therapy of cancer: DMXAA.** *Lancet Oncol* 2003, **4**:141–148.

15. Siemann DW, Chaplin DJ, Horsman MR: **Vascular-targeting therapies for treatment of malignant disease.** *Cancer* 2004, **100**:2491–2499.
16. Thorpe PE: **Vascular targeting agents as cancer therapeutics.** *Clin Cancer Res* 2004, **10**:415–427.
17. Siemann DW, Bibby MC, Dark GG, Dicker AP, Eskens FALM, Horsman MR, Marme D, LoRusso PM: **Differentiation and definition of vascular-targeted therapies.** *Am Assoc Cancer Res* 2005, **11**:416–420.
18. Marme D: **The impact of anti-angiogenic agents on cancer therapy.** *J Cancer Res Clin Oncol* 2003, **129**:607–620.
19. Kerbel R, Folkman J: **Clinical translation of angiogenesis inhibitors.** *Nat Rev Cancer* 2002, **2**:727–739.
20. Sridhar SS, Shepherd FA: **Targeting angiogenesis: a review of angiogenesis inhibitors in the treatment of lung cancer.** *Lung Cancer* 2003, **42**(Suppl 1):S81–91.
21. Eskens FA: **Angiogenesis inhibitors in clinical development; where are we now and where are we going?** *Br J Cancer* 2004, **90**:1–7.
22. Wachsberger P, Burd R, Dicker AP: **Tumor Response to Ionizing Radiation Combined with Antiangiogenesis or Vascular Targeting Agents: Exploring Mechanisms of Interaction.** *Clinical Cancer Research* 2003, **9**:1957–1971.
23. Siemann DW, Shi W: **Targeting the Tumor Blood Vessel Network to Enhance the Efficacy of Radiation Therapy.** *Seminars in Radiation Oncology* 2003, **13**(1):53–61.
24. Siemann DW, Shi W: **Dual targeting of tumor vasculature: Combining Avastin and vascular disrupting agents (CA4P or OXi4503).** *Anti-Cancer Research* 2008, **28**:2027–2032.
25. Landuyt W, Ahmad B, Nuyts S, Theys J, Op dBM, Rijnders A, Anne J, van Oosterom A, van den Bogaert W, Lambin P: ***In vivo* antitumor effect of vascular targeting combined with either ionizing radiation or anti-angiogenesis treatment.** *Int J Radiat Oncol Biol Phys* 2001, **49**:443–450.
26. Siemann DW, Shi W: **Efficacy of combined antiangiogenic and vascular disrupting agents in treatment of solid tumors.** *Int J Radiat Oncol Biol Phys* 2004, **60**(4):1233–1240.

27. Sheng Y, Hua J, Pinney KG, Garner CM, Kane RR, Prezioso JA, Chaplin DJ, Edvardsen K: **Combretastatin family member OXi4503 induces tumor vascular collapse through the induction of endothelial apoptosis.** *Int J Cancer* 2004, **111**:604–610.
28. Chan LS, Malcontenti-Wilson C, Muralidharan V, Christophi C: **Alterations in vascular architecture and permeability following OXi4503 treatment.** *Anti-Cancer Drugs* 2008, **19**:17–22.
29. Salmon HW, Mladinich C, Siemann DW: **Evaluations of vascular disrupting agents CA4P and OXi4503 in renal cell carcinoma (Caki-1) using a silicon based microvascular casting technique.** *Eur J Cancer* 2006, **42**:3073–3078.
30. Ehrmann RL, Knoth M: **Choriocarcinoma - Transfilter Stimulation of Vasoproliferation in Hamster Cheek Pouch Studied by Light and Electron Microscopy.** *Journal of the National Cancer Institute* 1968, **41**(6):1329–1333.
31. Folkman J, Bach M, Rowe JW, Davidoff F, Lambert P, Hirsch C, Goldberg A, Hiatt HH, Glass J, Henshaw E: **Tumor Angiogenesis - Therapeutic Implications.** *N Engl J Med* 1971, **285**(21):1182–1188.
32. Folkman J, Klagsbrun M: **Angiogenic Factors.** *Science* 1987, **235**(4787):442–447.
33. Ferrara N: **VEGF and the quest for tumour angiogenesis factors.** *Nat Rev Cancer* 2002, **2**(10):795–803.
34. Jain RK: **Molecular regulation of vessel maturation.** *Nature Medicine* 2003, **9**(6):685–693.
35. Ferrara N, Gerber HP, LeCouter J: **The biology of VEGF and its receptors.** *Nat Med* 2003, **9**:669–676.
36. Volm M, Koomagi R, Mattern J: **Prognostic value of vascular endothelial growth factor and its receptor Flt-1 in squamous cell lung cancer.** *International Journal of Cancer* 1997, **74**(1):64–68.
37. Yoshiji H, Gomez DE, Shibuya M, Thorgeirsson UP: **Expression of vascular endothelial growth factor, its receptor, and other angiogenic factors in human breast cancer.** *Cancer Research* 1996, **56**(9):2013–2016.
38. Ellis LM, Takahashi Y, Fenoglio CJ, Cleary KR, Bucana CD, Evans DB: **Vessel counts and vascular endothelial growth factor expression in pancreatic adenocarcinoma.** *European Journal of Cancer* 1998, **34**(3):337–340.

39. Tomisawa M, Tokunaga T, Oshika Y, Tsuchida T, Fukushima Y, Sato H, Kijima H, Yamazaki H, Ueyama Y, Tamaoki N *et al*: **Expression pattern of vascular endothelial growth factor isoform is closely correlated with tumour stage and vascularisation in renal cell carcinoma.** *European Journal of Cancer* 1999, **35**(1):133–137.
40. Sowter HM, Corps AN, Evans AL, Clark DE, Charnock-Jones DS, Smith SK: **Expression and localization of the vascular endothelial growth factor family in ovarian epithelial tumors.** *Laboratory Investigation* 1997, **77**(6):607–614.
41. Kim KJ, Li B, Winer J, Armanini M, Gillett N, Phillips HS, Ferrara N: **Inhibition of Vascular Endothelial Growth Factor-Induced Angiogenesis Suppresses Tumor-Growth In Vivo.** *Nature* 1993, **362**(6423):841–844.
42. Gerber HP, Kowalski J, Sherman D, Eberhard DA, Ferrara N: **Complete inhibition of rhabdomyosarcoma xenograft growth and neovascularization requires blockade of both tumor and host vascular endothelial growth factor.** *Cancer Research* 2000, **60**(22):6253–6258.
43. Kuo CJ, Farnebo F, Yu EY, Christofferson R, Swearingen RA, Carter R, von Recum HA, Yuan J, Kamihara J, Flynn E *et al*: **Comparative evaluation of the antitumor activity of antiangiogenic proteins delivered by gene transfer.** *Proc Natl Acad Sci U S A* 2001, **98**(8):4605–4610.
44. Holash J, Davis S, Papadopoulos N, Croll SD, Ho L, Russell M, Boland P, Leidich R, Hylton D, Burova E *et al*: **VEGF-Trap: A VEGF blocker with potent antitumor effects.** *Proc Natl Acad Sci U S A* 2002, **99**(17):11393–11398.
45. Presta LG, Chen H, Oconnor SJ, Chisholm V, Meng YG, Krummen L, Winkler M, Ferrara N: **Humanization of an anti-vascular endothelial growth factor monoclonal antibody for the therapy of solid tumors and other disorders.** *Cancer Research* 1997, **57**(20):4593–4599.
46. Lin YS, Nguyen C, Mendoza JL, Escandon E, Fei D, Meng YG, Modi NB: **Preclinical pharmacokinetics, interspecies scaling, and tissue distribution of a humanized monoclonal antibody against vascular endothelial growth factor.** *Journal of Pharmacology and Experimental Therapeutics* 1999, **288**(1):371–378.
47. Shima DT, Gougos A, Miller JW, Tolentino M, Robinson G, Adamis AP, Damore PA: **Cloning and mRNA expression of vascular endothelial growth factor in ischemic retinas of *Macaca fascicularis*.** *Investigative Ophthalmology & Visual Science* 1996, **37**(7):1334–1340.

48. Ryan AM, Eppler DB, Hagler KE, Bruner RH, Thomford PJ, Hall RL, Shopp GM, O'Neill CA: **Preclinical safety evaluation of rhuMAbVEGF, an antiangiogenic humanized monoclonal antibody.** *Toxicologic Pathology* 1999, **27**(1):78–86.
49. Margolin K, Gordon MS, Holmgren E, Gaudreault J, Novotny W, Fyfe G, Adelman D, Stalter S, Breed J: **Phase Ib trial of intravenous recombinant humanized monoclonal antibody to vascular endothelial growth factor in combination with chemotherapy in patients with advanced cancer: Pharmacologic and long-term safety data.** *Journal of Clinical Oncology* 2001, **19**(3):851–856.
50. Gordon MS, Margolin K, Talpaz M, Sledge GW, Holmgren E, Benjamin R, Stalter S, Shak S, Adelman DC: **Phase I safety and pharmacokinetic study of recombinant human anti-vascular endothelial growth factor in patients with advanced cancer.** *Journal of Clinical Oncology* 2001, **19**(3):843–850.
51. Cobleigh MA, Langmuir VK, Sledge GW, Miller KD, Haney L, Novotny WF, Reimann JD, Vassel A: **A phase I/II dose-escalation trial of bevacizumab in previously treated metastatic breast cancer.** *Seminars in Oncology* 2003, **30**(5):117–124.
52. Yang JC, Haworth L, Sherry RM, Hwu P, Schwartzentruber DJ, Topalian SL, Steinberg SM, Chen HX, Rosenberg SA: **A randomized trial of bevacizumab, an anti-vascular endothelial growth factor antibody, for metastatic renal cancer.** *N Engl J Med* 2003, **349**(5):427–434.
53. Kabbinavar F, Hurwitz HI, Fehrenbacher L, Meropol NJ, Novotny WF, Lieberman G, Griffing S, Bergsland E: **Phase II, randomized trial comparing bevacizumab plus fluorouracil (FU) leucovorin (LV) with FU/LV alone in patients with metastatic colorectal cancer.** *Journal of Clinical Oncology* 2003, **21**(1):60–65.
54. Li L, Rojiani AM, Siemann DW: **Preclinical evaluations of therapies combining the vascular targeting agent Combretastatin A-4 Disodium Phosphate and conventional anticancer therapies in the treatment of kaposi's sarcoma.** *Acta Oncologica* 2002, **41**(1):91–97.
55. Liang WC, Wu X, Peale FV, Lee CV, Meng YG, Gutierrez J, Fu L, Malik A, Gerber HP, Ferrara N *et al*: **Cross-species Vascular Endothelial Growth Factor (VEGF)-blocking Antibodies Completely Inhibit the Growth of Human Tumor Xenografts and Measure the Contribution of Stromal VEGF.** *THE JOURNAL OF BIOLOGICAL CHEMISTRY* 2006, **281**(2):951–961.
56. Koukourakis M, Giatromanolaki A, Sivridis E, Simopoulos K, Pissakas G, Gatter K, Harris AL: **Squamous cell head and neck cancer: evidence of angiogenic regeneration during radiotherapy.** *Anticancer Res* 2001, **21**:4301–4309.

57. Gerber HP, Ferrara N: **Pharmacology and Pharmacodynamics of Bevacizumab as Monotherapy or in Combination with Cytotoxic Therapy in Preclinical Studies.** *Cancer Res* 2005, **65**(3).
58. Siemann DW, Mercer E, Lepler S, Rojiani AM: **Vascular targeting agents enhance chemotherapeutic agent activities in solid tumor therapy.** *Int J Cancer* 2002, **99**:1–6.
59. Li L, Rojiani AM, Siemann DW: **Preclinical Evaluations of Therapies Combining the Vascular Targeting Agent Combretastatin A-4 Disodium Phosphate and Conventional Anticancer Therapies in the Treatment of Kaposi's Sarcoma.** *Acta Oncologica* 2002, **41**(1):91–97.
60. Lee CG, Heijn M, di Tomaso E, Griffon-Etienne G, Ancukiewicz M, Koike C, Park K, Ferrara N, Jain RK, Suit HD *et al*: **Anti-Vascular Endothelial Growth Factor Treatment Augments Tumor Radiation Response under Normoxic or Hypoxic Conditions.** *CANCER RESEARCH* 2000, **60**:5565–5570.
61. Gong H, Pottgen C, Stuben G, Havers W, Stuschke M, Schweigerer L: **ARGININE DEIMINASE AND OTHER ANTIANGIOGENIC AGENTS INHIBIT UNFAVORABLE NEUROBLASTOMA GROWTH: POTENTIATION BY IRRADIATION.** *Int J Cancer* 2003, **106**:723–728.
62. Teicher BA, Holden SA, Ara G, Dupuis NP, Liu F, Yuan J, Ikebe M, Kakeji Y: **Influence of an anti-angiogenic treatment on 9L gliosarcoma: Oxygenation and response to cytotoxic therapy.** *Int J Cancer* 1995, **61**(5):732–737.
63. Fenton B, Paoni S, Grimwood B, Ding I: **DISPARATE EFFECTS OF ENDOSTATIN ON TUMOR VASCULAR PERFUSION AND HYPOXIA IN TWO MURINE MAMMARY CARCINOMAS.** *Int J Radiation Oncology Biol Phys* 2003, **57**(4):1038–1046.
64. Fenton B, Paoni S, Ding I: **Pathophysiological Effects of Vascular Endothelial Growth Factor Receptor-2-Blocking Antibody plus Fractionated Radiotherapy on Murine Mammary Tumors.** *CANCER RESEARCH* 2004, **64**:5712–5719.
65. Bernsen HJJA, Rijken PFJW, Peters JPW, Bakker JH, Boerman RH, Wesseling P, van der Kogel AJ: **Suramin treatment of human glioma xenografts; effects on tumor vasculature and oxygenation status.** *Journal of Neuro-Oncology* 1999, **44**:129–136.
66. Leith JT, Papa G, Quaranto L, Michelson S: **Modification of the volumetric growth responses and steady-state hypoxic fractions of xenografted DLD-2**

- human colon carcinomas by administration of basic fibroblast growth factor or suramin.** *Br J Cancer* 1992, **66**:345–348.
67. Murata R, Nishimura Y, Hiraoka M: **AN ANTIANGIOGENIC AGENT (TNP-470) INHIBITED REOXYGENATION DURING FRACTIONATED RADIOTHERAPY OF MURINE MAMMARY CARCINOMA.** *Int J Radiation Oncology Biol Phys* 1997, **37**(5):1107– 1113.
 68. Rofstad E, Henriksen K, Galappathi K, Mathiesen B: **Antiangiogenic Treatment with Thrombospondin-1 Enhances Primary Tumor Radiation Response and Prevents Growth of Dormant Pulmonary Micrometastases after Curative Radiation Therapy in Human Melanoma Xenografts.** *CANCER RESEARCH* 2003, **63**:4055–4061.
 69. El-Emir E, Boxer GM, Petrie IA, Boden RW, Dearling JLJ, Begent RHJ, Pedley RB: **Tumour parameters affected by combretastatin A-4 phosphate therapy in a human colorectal xenograft model in nude mice.** *European Journal of Cancer* **41**:799–806.
 70. Galbraith SM, Maxwell RJ, Lodge MA, Tozer GM, Wilson J, Taylor NJ, Stirling JJ, Sena L, Padhani AR, Rustin GJS: **Combretastatin A4 Phosphate Has Tumor Antivascular Activity in Rat and Man as Demonstrated by Dynamic Magnetic Resonance Imaging.** *J Clin Oncol* 2003, **21**:2831–2842.
 71. Seshadri M, Sperryak JA, Maiery PG, Richard T. Cheney, Mazurchuk R, Bellnier DA: **Visualizing the Acute Effects of Vascular-Targeted Therapy In Vivo Using Intravital Microscopy and Magnetic Resonance Imaging: Correlation with Endothelial Apoptosis, Cytokine Induction, and Treatment Outcome.** *Neoplasia* 2007, **9**(2):128–135.
 72. Kotz B, West C, Saleem A, Jones T, Price P: **Blood flow and Vd (water): both biomarkers required for interpreting the effects of vascular targeting agents on tumor and normal tissue.** *Mol Cancer Ther* 2009, **8**(2):303–309.
 73. Tozer GM, Akerman S, Cross NA, Barber PR, Björndahl MA, Greco O, Harris S, Hill SA, Honess DJ, Ireson CR *et al*: **Blood Vessel Maturation and Response to Vascular-Disrupting Therapy in Single Vascular Endothelial Growth Factor-A Isoform–Producing Tumors.** *Cancer Res* 2008, **68**(7):2301–2311.
 74. deDeugd C, Wankhede M, Sorg BS: **Multimodal optical imaging of microvessel network convective oxygen transport dynamics.** *Applied Optics* 2009, **48**(10):D187–D197.
 75. Kimura H, Braun RD, Ong ET, Hsu R, Secomb TW, PapaHadjopoulos D, Hong K, Dewhirst M: **Fluctuations in red cell flux in tumor microvessels can lead**

- to transient hypoxia and reoxygenation in tumor parenchyma.** *Cancer Res* 1996, **56**:5522–5528.
76. Kerger H, Torres IP, Rivas M, Winslow RM, Intaglietta M: **Systemic and Subcutaneous Microvascular Oxygen-Tension in Conscious Syrian Golden-Hamsters.** *American Journal of Physiology-Heart and Circulatory Physiology* 1995, **268**(2):H802–H810.
77. Menger MD, Laschke MW, Vollmar B: **Viewing the microcirculation through the window: Some twenty years experience with the hamster dorsal skinfold chamber.** *European Surgical Research* 2002, **34**(1–2):83–91.
78. Laschke MW, Menger MD: **In vitro and in vivo approaches to study angiogenesis in the pathophysiology and therapy of endometriosis.** *Human Reproduction Update* 2007, **13**(4):331–342.
79. Dewhirst M: **Concepts of oxygen transport at the microcirculatory level.** *Semin Radiat Oncol* 1998, **8**:143–150.
80. Jain RK, Munn LL, Fukumura D: **Dissecting tumour pathophysiology using intravital microscopy.** *Nat Rev Cancer* 2002, **2**(4):266–276.
81. Leunig M, Yuan F, Menger MD, Boucher Y, Goetz AE, Messmer K, Jain RK: **Angiogenesis, Microvascular Architecture, Microhemodynamics, and Interstitial Fluid Pressure During Early Growth of Human Adenocarcinoma Ls174t in Scid Mice.** *Cancer Research* 1992, **52**(23):6553–6560.
82. Li CY, Shan SQ, Cao YT, Dewhirst MW: **Role of incipient angiogenesis in cancer metastasis.** *Cancer and Metastasis Reviews* 2000, **19**(1–2):7–11.
83. Abdul-Karim MA, Al-Kofahi K, Brown EB, Jain RK, Roysam B: **Automated tracing and change analysis of angiogenic vasculature from in vivo multiphoton confocal image time series.** *Microvasc Res* 2003, **66**(2):113–125.
84. Friedl P, Wolf K: **Proteolytic and non-proteolytic migration of tumour cells and leucocytes.** In: *Proteases and the Regulation of Biological Processes.* Edited by Saklatvala J, Nagase H, Salvesen G, vol. 70. London: Portland Press Ltd; 2003: 277–285.
85. Kashiwagi S, Izumi Y, Gohongi T, Demou ZN, Xu L, Huang PL, Buerk DG, Munn LL, Jain RK, Fukumura D: **NO mediates mural cell recruitment and vessel morphogenesis in murine melanomas and tissue-engineered blood vessels.** *Journal of Clinical Investigation* 2005, **115**(7):1816–1827.
86. Garini Y, Young IT, McNamara G: **Spectral imaging: Principles and applications.** *Cytom Part A* 2006, **69A**(8):735–747.

87. Wyatt CL: **Infrared Spectrometer - Liquid-Helium Cooled Rocketborne Circular-Variable Filter**. *Applied Optics* 1975, **14**(12):3086–3092.
88. Miller PJ: **Use of Tunable Liquid-Crystal Filters to Link Radiometric and Photometric Standards**. *Metrologia* 1991, **28**(3):145–149.
89. Shonat RD, Wachman ES, Niu W, Koretsky AP, Farkas DL: **Near-simultaneous hemoglobin saturation and oxygenation tension maps in mouse brain using an AOTF microscope**. *Biophysical Journal* 1997, **73**:1223–1231.
90. Sorg BS, Moeller BJ, Donovan O, Cao Y, Dewhirst MW: **Hyperspectral imaging of hemoglobin saturation in tumor microvasculature and tumor hypoxia development**. *J Biomed Opt* 2005, **10**(4): Research Papers.
91. Perry BN, Arbiser JL: **The duality of angiogenesis: implications for therapy of human disease**. *Journal of Investigative Dermatology* 2006, **126**:2160–2166.
92. Otrrock ZK, Mahfouz RAR, Makarem JA, Shamseddine AI: **Understanding the biology of angiogenesis: Review of the most important molecular mechanisms**. *Blood Cells, Molecules, and Diseases* 2007, **39**:212–220.
93. Carmeliet P, Jain RK: **Angiogenesis in cancer and other diseases**. In: *Nature*. vol. 407; 2000: 249–257.
94. Dewhirst MW: **Angiogenesis and blood flow in solid tumors**. In: *Drug Resistance in Oncology*. Edited by Teicher BA. New York: Marcel Dekker; 1993: 3–23.
95. Warren BA: **The vascular morphology of tumors**. In: *Tumor blood circulation: Angiogenesis, vascular morphology and blood flow of experimental and human tumors*. Edited by Peterson HI. Boca Raton: CRC Press, Inc.; 1979: 1–47.
96. Simons M: **Angiogenesis, arteriogenesis, and diabetes - paradigm reassessed?** *Journal of the American College of Cardiology* 2005, **46**(5):835–837.
97. Martin A, Komada MR, Sane DC: **Abnormal angiogenesis in diabetes mellitus**. *Medicinal Research Reviews* 2003, **23**(2):117–145.
98. Carvalho JF, Blank M, Shoenfeld Y: **Vascular endothelial growth factor (VEGF) in autoimmune diseases**. *Journal of Clinical Immunology* 2007, **27**(3):246–256.

99. Bainbridge J, Sivakumar B, Paleolog E: **Angiogenesis as a therapeutic target in arthritis: lessons from oncology.** *Current Pharmaceutical Design* 2006, **12**:2631–2644.
100. Azfar RS, Gelfand JM: **Psoriasis and metabolic disease: epidemiology and pathophysiology.** *Current Opinion in Rheumatology* 2008, **20**:416–422.
101. Gargiulo P, Giusti C, Pietrobono D, La Torre D, Diacono D, Tamburrano G: **Diabetes mellitus and retinopathy.** *Digestive and Liver Disease* 2004, **36 (Suppl 1)**:S101–S105.
102. Wegewitz U, Göhring I, Spranger J: **Novel approaches in the treatment of angiogenic eye disease.** *Current Pharmaceutical Design* 2005, **11**:2311–2330.
103. O’goshi KI, Serup J: **Safety of sodium fluorescein for in vivo study of skin.** *Skin Research and Technology* 2006, **12**:155–161.
104. Werkmeister E, Kerdjoudj H, Marchal L, Stoltz JF, Dumas D: **Multiphoton microscopy for blood vessel imaging: new non-invasive tools (Spectral, SHG, FLIM).** *Clinical Hemorheology and Microcirculation* 2007, **37**:77–88.
105. Schaffer CB, Friedman B, Nishimura N, Schroeder LF, Tsai PS, Ebner FF, Lyden PD, Kleinfeld D: **Two-photon imaging of cortical surface microvessels reveals a robust redistribution in blood flow after vascular occlusion.** *PLoS Biology* 2006, **4**:e22.
106. Reyes-Aldasoro CC, Wilson I, Prise VE, Barber PR, Ameer-Beg M, Vojnovic B, Cunningham VJ, Tozer GM: **Estimation of apparent tumor vascular permeability from multiphoton fluorescence microscopic images of P22 rat sarcomas in vivo.** *Microcirculation* 2008, **15(1)**:65–79.
107. Fu D, Matthews TE, Ye T, Piletic IR, Warren WS: **Label-free in vivo optical imaging of microvasculature and oxygenation level.** *Journal of Biomedical Optics* 2008, **13(4)**:article 040503.
108. Choi B, Kang NM, Nelson JS: **Laser speckle imaging for monitoring blood flow dynamics in the in vivo rodent dorsal skin fold model.** *Microvasc Res* 2004, **68**:143–146.
109. Dunn AK, Devor A, Bolay H, Andermann ML, Moskowitz MA, Dale AM, Boas DA: **Simultaneous imaging of total cerebral hemoglobin concentration, oxygenation, and blood flow during functional activation.** *Optics Letters* 2003, **28(1)**:28–30.
110. Kolkman RGM, Klaessens JHGM, Hondebrink E, Hopman JCW, de Mul FFM, Steenbergen W, Thijssen JM, van Leeuwen TG: **Photoacoustic determination**

- of blood vessel diameter.** *Physics in Medicine and Biology* 2004, **49**:4745–4756.
111. Wang X, Ku G, Wegiel MA, Bornhop DJ, Stoica G, Wang LV: **Noninvasive photoacoustic angiography of animal brains in vivo with near-infrared light and an optical contrast agent.** *Optics Letters* 2004, **29**(7):730–732.
 112. Wang X, Xie X, Ku G, Wang LV, Stoica G: **Noninvasive imaging of hemoglobin concentration and oxygenation in the rat brain using high-resolution photoacoustic tomography.** *Journal of Biomedical Optics* 2006, **11**(2):article 024015.
 113. Hitzenberger C, Trost P, Lo PW, Q. Zhou, " Opt. Express 11, 2753–2761 (2003): **Three-dimensional imaging of the human retina by high-speed optical coherence tomography.** *Optics Express* 2003, **11**:2753–2761.
 114. Izatt JA, Kulkarni MD, Yazdanfar S, Barton JK, Welch AJ: **In vivo bidirectional color Doppler flow imaging of picoliter blood volumes using optical coherence tomography.** *Optics Letters* 1997, **22**:1439–1441.
 115. Michaely R, Bachmann AH, Villiger ML, Blatter C, Lasser T, Leitgeb RA: **Vectorial reconstruction of retinal blood flow in three dimensions measured with high resolution resonant Doppler Fourier domain optical coherence tomography.** *Journal of Biomedical Optics* 2007, **12**(4):article 041213.
 116. Faber DJ, Mick EG, Aalders MCG, van Leeuwen TG: **Toward assessment of blood oxygen saturation by spectroscopic optical coherence tomography.** *Optics Letters* 2005, **30**:1015–1017.
 117. Faber DJ, Mik EG, Aalders MCG, van Leeuwen TG: **Light absorption of (oxy-)hemoglobin assessed by spectroscopic optical coherence tomography.** *Optics Letters* 2003, **28**(16):1436–1438.
 118. Lu CW, Lee CK, Tsai MT, Wang YM, Yang CC: **Measurement of the hemoglobin oxygen saturation level with spectroscopic spectral-domain optical coherence tomography.** *Optics Letters* 2008, **33**(5):416–418.
 119. Kagemann L, Wollstein G, Wojtkowski M, Ishikawa H, Townsend KA, Gabriele ML, Srinivasan VJ, Fujimoto JG, Schuman JS: **Spectral oximetry assessed with high-speed ultra-high resolution optical coherence tomography.** *Journal of Biomedical Optics* 2007, **12**(4):article 041212.
 120. Iftimia NV, Hammer DX, Bigelow CE, Rosen DI, Ustun T, Ferrante AA, Vu D, Ferguson RD: **Toward noninvasive measurement of blood hematocrit using**

- spectral domain low coherence interferometry and retinal tracking.** *Optics Express* 2006, **14**:3377–3388.
121. Mariampillai A, Standish BA, Moriyama EH, Khurana M, Munce NR, Leung MKK, Jiang J, Cable A, Wilson BC, Vitkin A *et al*: **Speckle variance detection of microvasculature using swept-source optical coherence tomography.** *Optics Letters* 2008, **33**(13):1530–1532.
 122. Styp-Rekowska B, Disassa NM, Reglin B, Ulm L, Kuppe H, Secomb TW, Pries AR: **An imaging spectroscopy approach for measurement of oxygen saturation and hematocrit during intravital microscopy.** *Microcirculation* 2007, **14**:207–221.
 123. Kobayashi H, Takizawa N: **Imaging of oxygen transfer among microvessels of rat cremaster muscle.** *Circulation* 2002, **105**:1713–1719.
 124. Sorg BS, Hardee ME, Agarwal N, Moeller BJ, Dewhirst MW: **Spectral imaging facilitates visualization and measurements of unstable and abnormal microvascular oxygen transport in tumors.** *Journal of Biomedical Optics* 2008, **13**(1):article 014026.
 125. Sorg BS, Moeller BJ, Donovan O, Cao Y, Dewhirst MW: **Hyperspectral imaging of hemoglobin saturation in tumor microvasculature and tumor hypoxia development.** *Journal of Biomedical Optics* 2005, **10**:044004.
 126. Skala MC, Fontanella A, Hendargo H, Dewhirst MW, Izatt JA: **Combined hyperspectral and spectral domain optical coherence tomography microscope for noninvasive hemodynamic imaging.** *Optics Letters* 2009, **34**(3):289–291.
 127. Shonat RD, Johnson PC: **Oxygen tension gradients and heterogeneity in venous microcirculation: a phosphorescence quenching study.** *American Journal of Physiology - Heart and Circulatory Physiology* 1997, **272**:H2233–H2240.
 128. Unthank JL, Lash JM, Nixon JC, Sidner RA, Bohlen HG: **Evaluation of carbocyanine-labeled erythrocytes for microvascular measurements.** *Microvasc Res* 1993, **45**:193–210.
 129. Shonat RD, Wachman ES, Niu WH, Koretsky AP, Farkas DL: **Near-simultaneous hemoglobin saturation and oxygen tension maps in mouse brain using an AOTF microscope.** *Biophysical Journal* 1997, **73**:1223–1231.
 130. Ferreira AJ, Raizada MK: **Genomic and proteomic approaches for targeting of angiotensin-converting enzyme2 for cardiovascular diseases.** *Current Opinion in Cardiology* 2008, **23**(4):364–369.

131. Santos RA, Ferreira AJ, Simões E, Silva AC: **Recent advances in the angiotensin-converting enzyme 2-angiotensin(1–7)-Mas axis.** *Experimental Physiology* 2008, **93**(5):519–527.
132. Katayama T, Ikeda Y, Handa M, Tamatani T, Sakamoto S, Ito M, Ishimura Y, Suematsu M: **Immunoneutralization of glycoprotein Iba attenuates endotoxin-induced interactions of platelets and leukocytes with rat venular endothelium in vivo.** *Circulation Research* 2000, **86**(10):1031–1037.
133. Park SO, Lee YJ, Seki T, Hong KH, Fliess N, Jiang Z, Park A, Wu X, Kaartinen V, Roman BL *et al*: **ALK5- and TGFBR2-independent role of ALK1 in the pathogenesis of hereditary hemorrhagic telangiectasia type 2.** *Blood* 2008, **11**(2):633–642.
134. Vaupel P, Kallinowski F, Okunieff P: **Blood flow, oxygen and nutrient supply, and metabolic microenvironment of human tumors: a review.** *Cancer Res* 1989, **49**:6449–6465.
135. Bristow RG, Hill RP: **Hypoxia, DNA repair and genetic instability.** *Nature Reviews - Cancer* 2008, **8**:180–192.
136. Durand RE, Aquino-Parsons C: **Clinical relevance of intermittent tumour blood flow.** *Acta Oncologica* 2001, **40**(8):929–936.
137. Durand RE, Aquino-Parsons C: **Non-constant tumour blood flow - implications for therapy.** *Acta Oncologica* 2001, **40**(7):862–869.
138. Rofstad EK, Galappathi K, Mathiesen B, Ruud E-BM: **Fluctuating and diffusion-limited hypoxia in hypoxia-induced metastasis.** *Clinical Cancer Research* 2007, **13**:1971–1978.
139. Brurberg KG, Gaustad JV, Mollatt CS, Rofstad EK: **Temporal heterogeneity in blood supply in human tumor xenografts.** *Neoplasia* 2008, **10**(7):727–735.
140. Sorg BS, Hardee ME, Agarwal N, Moeller BJ, Dewhirst MW: **Spectral imaging facilitates visualization and measurements of unstable and abnormal microvascular oxygen transport in tumors.** *Journal of Biomedical Optics* 2008, **13**(1).
141. Gaustad JV, Simonsen TG, Brurberg KG, Huuse EM, Rofstad EK: **Blood Supply in Melanoma Xenografts Is Governed by the Morphology of the Supplying Arteries.** *Neoplasia* 2009, **11**(3):277–285.

142. Hardee ME, Dewhirst MW, Agarwal N, Sorg BS: **Novel imaging provides new insights into mechanisms of oxygen transport in tumors.** *Current Molecular Medicine* 2008:accepted.
143. Fitzgerald DJ: **Vascular biology of thrombosis: The role of platelet–vessel wall adhesion.** *Neurology* 2001, **57(Suppl 2)**:S1–S4.
144. Kyrle PA, Eichinger S: **Deep vein thrombosis.** *Lancet* 2005, **365**:1163–1174.
145. Fraga-Silva RA, Ferreira AJ, Sorg BS, Wankhede M, deDeugd C, Jun JY, Baker MB, Castellano RJ, Katovich MJ, Raizada MK: **Pharmacological ACE2 activation exerts antithrombotic activity.** In: *American Heart Association International Stroke Conference*. San Diego, CA; 2009.
146. Fraga-Silva R, Sorg BS, Wankhede M, DeDeugd C, Jun J, Baker M, Li Y, Castello R, Katovich M, Raizada MK *et al*: **ACE2 Activation Promotes Anti-Thrombotic Activity.** *Molecular Medicine* 2010, **In press**.
147. Konner K: **The initial creation of native arteriovenous fistulas: surgical aspects and their impact on the practice of nephrology.** *Seminars in Dialysis* 2003, **16(4)**:291–298.
148. Jain RK: **Determinants of tumor blood flow: A review.** *Cancer Research* 1988, **48**:2641–2658.
149. Widdicombe J: **Microvascular anatomy of the nose.** *Allergy* 1997, **52(40)**:(Suppl) 7–11.
150. Zakrzewicz A, Secomb TW, Pries AR: **Angioadaptation: Keeping the vascular system in shape.** *News in Physiological Sciences* 2002, **17**:197–201.
151. Guyton AC: **Textbook of Medical Physiology**, 8th edn. Philadelphia, PA: W. B. Saunders Company; 1991.
152. Park SO, Wankhede M, Lee YJ, Choi EJ, Fliess N, Choe S, Oh SH, Walter G, Raizada MK, Sorg BS *et al*: **Real-time imaging of de novo arteriovenous malformation in a mouse model of hereditary hemorrhagic telangiectasia.** *J Clin Invest* 2009, **119**:3487–3496.
153. Denekamp J: **Endothelial cell proliferation as a novel approach to targeting tumour therapy.** *Br J Cancer* 1982, **45**:136–139.
154. Denekamp J, Hill SA, Hobson B: **Vascular occlusion and tumour cell death.** *Eur J Cancer Clin Oncol* 1983, **19**:271–275.

155. Chaplin DJ, Pettit GR, Hill SA: **Anti-vascular approaches to solid tumour therapy: evaluation of combretastatin A4 phosphate.** *Anticancer Res* 1999, **19**:189–195.
156. Siemann DW, Chaplin DJ, Walicke PA: **A review and update of the current status of the vasculature disabling agent combretastatin-A4 phosphate (CA4P).** *Expert Opinion on Investigational Drugs* 2009, **18**:189–197.
157. Siemann DW, Horsman MR: **Vascular targeted therapies in oncology.** *Cell and Tissue Research* 2009, **335**:241–248.
158. Salmon HW, Mladinich C, Siemann DW: **Evaluations of vascular disrupting agents CA4P and OXi4503 in renal cell carcinoma (Caki-1) using a silicon based microvascular casting technique.** *European Journal of Cancer* 2006, **42**:3073–3078.
159. Kimura H, Braun RD, Ong ET, Hsu R, Secomb TW, Papahadjopoulos D, Hong K, Dewhirst MW: **Fluctuations in red cell flux in tumor microvessels can lead to transient hypoxia and reoxygenation in tumor parenchyma.** *Cancer Research* 1996, **56**:5522–5528.
160. Sorg BS, Moeller BJ, Donovan O, Cao Y, Dewhirst MW: **Measurement of hemoglobin saturation in tumor microvasculature in preclinical models using hyperspectral imaging.** *Proceedings of SPIE* 2005, **5694**:74–81.
161. Jordan A, Hadfield JA, Lawrence NJ, McGown AT: **Tubulin as a Target for Anticancer Drugs: Agents Which Interact with the Mitotic Spindle.** *Med Res Rev* 1998, **18**(4):259–296.
162. Lin CM, Singh SB, Chu PS, Dempcy R, Schmidt JM, Pettit GR, Hamel E: **Interactions of Tubulin with Potent Natural and Synthetic Analogs of the Antimitotic Agent Combretastatin: a Structure-Activity Study.** *Molecular Pharmacology* 1988, **34**:200–208.
163. Folkes LK, Christlieb M, Madej E, Stratford MRL, Wardman P: **Oxidative Metabolism of Combretastatin A-1 Produces Quinone Intermediates with the Potential To Bind to Nucleophiles and To Enhance Oxidative Stress via Free Radicals.** *Chem Res Toxicol* 2007, **20**:1885–1894.
164. Salmon BA, Siemann DW: **Characterizing the tumor response to treatment with combretastatin A4 phosphate.** *Int J Radiation Oncology Biol Phys* 2007, **68**(1):211–217.
165. Tozer GM, Ameer-Beg SM, Baker J, Barber PR, Hill SA, Hodgkiss RJ, Locke R, Prise VE, Wilson I, Vojnovic B: **Intravital imaging of tumour vascular**

- networks using multi-photon fluorescence microscopy.** *Advanced Drug Delivery Reviews* 2005, **57**:135–152.
166. Siemann DW, Rojjani AM: **The Vascular disrupting Agent ZD6126 shows increased antitumor efficacy and enhanced radiation response in large advanced tumors.** *Int J Radiation Oncology Biol Phys* 2005, **62**(3):846–853.
167. Parkins CS, Holder AL, Hill SA, Chaplin DJ, Tozer GM: **Determinants of anti-vascular action by combretastatin A-4 phosphate: role of nitric oxide.** *British Journal of Cancer* 2000, **83**(6):811–816.
168. Skliarenko JV, Lunt SJ, Gordon ML, Vitkin A, Milosevic M, Hill RP: **Effects of the Vascular Disrupting Agent ZD6126 on Interstitial Fluid Pressure and Cell Survival in Tumors.** *Cancer Res* 2006, **66**(4):2074–2080.
169. Dalal S, Burchill SA: **Preclinical evaluation of vascular-disrupting agents in Ewing's sarcoma family of tumours.** *European Journal of Cancer* 2009, **45**:713–722.
170. Folkman J: **How is blood vessel growth regulated in normal and neoplastic tissue?** *Cancer Res* 1986, **46**:467–473.
171. Landuyt W, Verdoes O, Darius D, Drijkoningen M, Nuyts S, Theys J, Stockx L, Wynendaele W, Fowler J, Maleux G *et al*: **Vascular targeting of solid tumours: a major 'inverse' volume-response relationship following combretastatin A-4 phosphate treatment of rat rhabdomyosarcomas.** *European Journal of Cancer* 2000, **36**:1833–1843.
172. Masunaga SI, Nagasawa H, Nagata K, Suzuki M, Uto Y, Hori H, Kinashi Y, Ono K: **Dependency of the effect of a vascular disrupting agent on sensitivity to tirapazamine and gamma-ray irradiation upon the timing of its administration and tumor size, with reference to the effect on intratumor quiescent cells.** *J Cancer Res Clin Oncol* 2007, **133**:47–55.
173. Pettit GR, Singh SB, Hamel E, Lin C, Alberts D, Garcia-Kendall: **Isolation and structure of the strong cell growth and tubulin inhibitor combretastatin A-4.** *Experientia* 1989, **45**:209–211.
174. Wankhede M, DeDeugd C, Siemann DW, Sorg BS: **In vivo functional differences in microvascular response of 4T1 and Caki-1 tumors after treatment with OXi4503.** *Oncology Reports* 2010, **23**:685–692.
175. Sharathkumar, A.A. & Shapiro, A. **Hereditary haemorrhagic telangiectasia.** *Haemophilia* 2008, **14**:1269–1280.

176. Berg, J., *et al.* **Hereditary hemorrhagic telangiectasia: A questionnaire based study to delineate the different phenotypes caused by endoglin and ALK1 mutations.** *J Med Genet* 2003, **40**:585–590.
177. Sadick, H., *et al.* **Hereditary hemorrhagic telangiectasia: An update on clinical manifestations and diagnostic measures.** *Wien. Klin. Wochenschr.* 2006 **118**:72–80.
178. Willoughby, S., Holmes, A. & Loscalzo, J. **Platelets and cardiovascular disease.** *Eur J Cardiovasc Nurs* 2002 **1**:273–288.
179. Braverman, I.M., Keh, A. & Jacobson, B.S. **Ultrastructure and three-dimensional organization of the telangiectases of hereditary hemorrhagic telangiectasia.** *J Invest Dermatol* 1990 **95**:422–427.
180. Murphy, P.A., *et al.* **Endothelial Notch4 signalling induces hallmarks of brain arteriovenous malformations in mice.** *Proc Natl Acad Sci* 2008 **105**:10901–10906.

BIOGRAPHICAL SKETCH

Mamta Wankhede obtained her bachelor's degree in Electronics Engineering from Nagpur University, India (1999–2003) and joined the Biomedical Engineering program at University of Florida for a Master of Science degree (2005–2008). After completion of her PhD program in biomedical engineering in Dec 2010, she aspires to remain in the research field in future.